National Technical University of Athens
School of Chemical Engineering
Department II: Department of Process Analysis and Plant Design
/
Institut National Polytechnique de Toulouse
École Nationale Supérieure des Ingénieurs en Arts Chimiques et Technologiques
Laboratoire du CIRIMAT (SURF)

Diploma Thesis

Surface morphology, structure, and compositional characterization of MOCVD processed silicon oxynitride coatings for aqueous corrosion barriers

Paris Papavasileiou

Supervisors
Andreas Boudouvis (NTUA)
Constantin Vahlas (ENSIACET)

September 2020

Table of Contents

Acknowledgements

The present thesis was conducted under the Erasmus+ framework for education, in collaboration between the School of Chemical Engineering of the National Technical University of Athens and the École Nationale Supérieure des Ingénieurs en Arts Chimiques et Technologiques of Institut National Polytechnique de Toulouse.

Although the completion of the present work signals the end of my 5-year long journey as an undergraduate chemical engineer, it was also a journey of its own. My work in the CIRIMAT laboratory - an international environment – and the experience of living on my own in France were experiences that I will keep close to heart and will reminisce forever. Although a lot of obstacles got in the way, with the CoVid epidemic and the resulting lockdown that took place in France being the two main protagonists, the present work was completed with few problems. There are a lot of people that I must thank for their contribution, big or small.

First, I would like to thank my two supervisors, Andreas Boudouvis and Constantin Vahlas. Professor Andreas Boudouvis was my supervisor in Greece, and he was the one that motivated me to take the big step and pursue a thesis in an international environment. For this motivation and the opportunity that he gave to me, I am deeply grateful. Dr. Constantin Vahlas was my supervisor in France and was the project coordinator in the project I was a part of. I would also like to thank him for the opportunity he gave me and for the support he provided whenever it was needed, in both scientific and every-day issues.

I would also like to thank Konstantina Topka, who was the PhD candidate under whom I worked. Konstantina was the one that trained me and got me accustomed in the project. Me and Konstantina had a lot of interesting discussions regarding the project. Her ideas and opinions played a big role in the steps that I took in completing the present work. Konstantina was available for any question and provided constructive feedback whenever needed. I consider her contribution to this work vital. I will forever be appreciative of her assistance.

Furthermore, I would like to thank some other members of the project. Brigitte Caussat, Hugues Vergnes, Diane Samelor and Francois Senocq all provided priceless feedback and ideas during project meetings. Their contribution was detrimental for the development of the present work.

Also, I would like to thank Babacar Diallo for performing the whole range of IBA methods (RBS, ERDA and NMR) and providing me with valuable results.

Next, I would like to thank all my friends for their support during the tough period of the quarantine. My – almost daily – contact with them helped me retain a high morale during those difficult times.

Finally, I would like to thank my family and especially my parents, Efi and George, for their never-ending motivation and support throughout all those years. Their support has been vital for my whole evolution as a person.

Abstract

The present thesis was conducted under the Erasmus+ framework for education, in collaboration between the School of Chemical Engineering of the National Technical University of Athens and the École Nationale Supérieure des Ingénieurs en Arts Chimiques et Technologiques of Institut National Polytechnique de Toulouse.

The deposition of silica-based materials is widely used in numerous industrial sectors, including microelectronics and pharmaceutics. Depending on their target-application, these materials need to fulfill specific requirements in terms of mechanical properties, durability, and composition. More specifically, the implementation of innovative silicon oxynitrides (SiO_xN_y) coatings in pharmaceutical applications dictates good aqueous barrier and anti-diffusion properties, as well as effective corrosion resistance. In the present work, a study of the structure and composition of the produced thin films was conducted.

First, by using spectrometric ellipsometry, the thickness and composition of the samples was measured. The ellipsometry results were obtained using a two-phase Bruggeman effective medium approximation model (BEMA model), considering the oxynitride films to consist of silica (SiO_2) and silicon nitride (Si_3N_4) building blocks. Towards the end of this work, a 3-phase BEMA model was also used, in order to incorporate carbon in the compositional results.

Then, to acquire in-depth information regarding the chemical species present in the thin films, Fourier-Transform infrared spectroscopy was utilised. Several chemical species were detected and, depending on the deposition conditions and sample position in the reactor, different species and spectral characteristics were observed. The position and intensity of the Si-O-Si TO3 stretching mode and the Si-N was thoroughly analysed as a function of oxygen flow and temperature parameters.

Using both ellipsometry and FTIR analyses, the evolution of the films structure and composition was tracked along the length of the reactor. Samples of the same experiment were compared in order to understand the effect of sample position in the film's final structure. Then, samples from different experiments were compared so that the effect of the applied deposition conditions could be studied.

By using the available compositional results acquired through three distinct Ion beam analysis (IBA) methods, namely Rutherford Backscattering Spectroscopy (RBS), Elastic Recoil Detection Analysis (ERDA) and Nuclear Reaction Analysis (NRA), the several trends observed in the FTIR and ellipsometry studies could be verified. Additionally, new trends regarding other elements of the film, like carbon and hydrogen could be observed in more detail. Via the use of the results obtained by IBA, the 3-phase BEMA ellipsometry model mentioned above was calibrated.

Finally, a chemical etching test was performed on the films using a buffer oxide etch (BOE) solution through which the performance of the films against corrosion were assessed. This performance was then correlated with the nitrogen content in the film.

Key words: Chemical vapor deposition (CVD), Silicon oxynitrides, Solid state analysis, Ellipsometry, FTIR, IBA methods, BOE test

Εκτενής περίληψη (extensive summary – in Greek)

Η παρούσα διπλωματική εργασία εκπονήθηκε εντός του πλαισίου ERASMUS+, σε συνεργασία μεταξύ της Σχολής Χημικών Μηχανικών του Εθνικού Μετσόβιου Πολυτεχνείου και της École Nationale Supérieure des Ingénieurs en Arts Chimiques et Technologiques του Institut National Polytechnique de Toulouse.

Η απόθεση υλικών βασισμένων στην πυριτία χρησιμοποιείται ευρύτατα και σε πολυάριθμους τομείς τις βιομηχανίας, όπως στους τομείς των μικροηλεκτρονικών και της φαρμακοποιίας. Αυτά τα υλικά οφείλουν να εκπληρώνουν συγκεκριμένες απαιτήσεις όσον αφορά τις μηχανικές τους ιδιότητες, την αντοχή τους και την σύστασή τους. Πιο συγκεκριμένα, η χρήση καινοτόμων επιστρώσεων οξυνιτριδίων του πυριτίου (SiO_xN_y) σε εφαρμογές της φαρμακευτικής οδηγεί σε καλές ιδιότητες υδατικού φράγματος, καθώς και καλές ιδιότητες ενάντια στην διάχυση. Πέρα από αυτά, οι επιστρώσεις αυτές είναι πολύ αποδοτικές ενάντια στην διάβρωση. Σε αυτή την μελέτη, εξετάστηκαν η δομή και η σύσταση λεπτών υμενίων οξυνιτριδίου του πυριτίου, με σκοπό την συσχέτιση τους με τις ιδιότητες που προκύπτουν.

Η παραγωγή των υμενίων έλαβε χώρα εντός ενός σωληνοειδούς αντιδραστήρα. Για την παραγωγή τους, χρησιμοποιήθηκε ένα χημικό σύστημα αποτελούμενο από μια πρόδρομη μεταλλοργανική ένωση, την τριδιμεθυλσιλυλαμίνη (tridimethylsilylamine – TDMSA), οξυγόνο (O_2) και αμμωνία (NH_3). Η διεργασία λάμβανε χώρα σε πίεση 730 Torr – μια πίεση ελαφρώς υποατμοσφαιρική, για λόγους ασφαλείας. Η θερμοκρασία δεν ήταν σταθερή σε όλο το μήκος του αντιδραστήρα. Παρόλα αυτά, μια ισοθερμοκρασιακή ζώνη μπορούσε να παρατηρηθεί σε απόσταση μεταξύ 360 και 500 mm από την είσοδο του αντιδραστήρα. Συνεπώς για τις δύο θερμοκρασίες της ισοθερμοκρασιακής ζώνης (625 and 650°C), οι οποίες θεωρούνται ως οι θερμοκρασίες απόθεσης λήφθηκαν τα θερμοκρασιακά προφίλ.

Εξετάστηκαν υμένια προερχόμενα από 10 διαφορετικά πειράματα. Τα διάφορα πειράματα, διάρκειας 2.5–5 ωρών, έλαβαν χώρα χρησιμοποιώντας διαφορετικές αναλογίες αντιδρώντων στην αέρια φάση, καθώς και διαφορετικές θερμοκρασίες απόθεσης. Η ποικιλία πειραματικών παραμέτρων που χρησιμοποιήθηκαν, οδήγησε όπως αναμενόταν σε υμένια διαφορετικής σύστασης και δομής, κάτι που προκαλεί διαφορετικές ιδιότητες.

Οι μέθοδοι ανάλυσης που χρησιμοποιήθηκαν στα πλαίσια αυτής της εργασίας ήταν τρείς, με την κάθε μια να προσφέρει κάτι διαφορετικό στην συνολική μελέτη της στερεής φάσης. Συγκεκριμένα, χρησιμοποιήθηκε η μέθοδος της φασματοσκοπικής ελλειψομετρίας (Spectroscopic Ellipsometry) για την διερεύνηση του πάχους και της σύστασης των παραχθέντων υμενίων. Έπειτα, έγινε χρήση της μεθόδου της φασματοσκοπίας υπερύθρου με μετασχηματισμό Fourier (Fourier Transform Infrared Spectroscopy – FTIR), μέσω της οποίας ερευνήθηκαν σε βάθος οι διάφορες χαρακτηριστικές ομάδες οι οποίες βρίσκονται εντός των υμενίων. Επιπροσθέτως, έγινε χρήση των διαθέσιμων αποτελεσμάτων από τρείς μεθόδους της οικογένειας των μεθόδων ανάλυσης δέσμης ιόντων (Ion Beam Analysis - IBA methods), για την επιβεβαίωση των διάφορων τάσεων που παρατηρήθηκαν μέσω της ελλειψομετρίας και της φασματοσκοπίας υπερύθρου με μετασχηματισμό Fourier. Συγκεκριμένα, έγινε χρήση των μεθόδων: α) της φασματοσκοπίας ανάδρασης διασποράς κατά Rutherford (Rutherford Backscattering Spectroscopy – RBS), β) της ανάλυσης ανίχνευσης ελαστικής ανάκρουσης (Elastic Recoil Detection Analysis – ERDA) και γ) της ανάλυσης πυρηνικών αντιδράσεων (Nuclear Reaction Analysis). Τέλος, για την εκτίμηση της απόδοσης των υμενίων ενάντια στην διάβρωση, έγινε χρήση μιας μεθόδου υγρής χημικής χάραξης, χρησιμοποιώντας ένα (6:1) Buffer Oxide Etch διάλυμα (6 μέρη NH_4F (40%) και 1 μέρος HF (49%), Sigma Aldrich). Στην συνέχεια έγινε απόπειρα συσχέτισης διαφόρων παραμέτρων με την απόδοση των υμενίων στην δοκιμασία που αναφέρθηκε παραπάνω.

Με την μέθοδο της ελλειψομετρίας αναλύθηκαν όλα τα δείγματα από κάθε πείραμα, με την χρήση μιας συσκευής Semilab-SE2000, η οποία λειτουργούσε σε μήκη κύματος εντός του εύρους 300-1000 nm, ώστε να μελετηθεί η εξέλιξη των υμενίων κατά μήκος του αντιδραστήρα. Κάθε υμένιο αναλύθηκε σε 5 διαφορετικά σημεία, ώστε να εξεταστεί η «χαρτογραφία» του κάθε υμενίου. Για την λήψη αποτελεσμάτων πάχους και σύστασης, χρησιμοποιήθηκε αρχικά ένα κατά Bruggeman effective medium approximation μοντέλο, για το οποίο έγινε η παραδοχή ότι τα υμένια αποτελούνται από 2 ξεχωριστές φάσεις: μια φάση καθαρής πυριτίας (SiO_2) και μια φάση καθαρού νιτριδίου του πυριτίου (Si_3N_4). Με αυτόν τον τρόπο, μπορούν να ληφθούν αποτελέσματα όσον αφορά την περιεκτικότητα των υμενίων σε άζωτο, κάτι που φαίνεται να αποτελεί ένα σημαντικό κριτήριο για τις τελικές ιδιότητες των υμενίων. Στην συνέχεια λήφθηκε ο μέσος όρος πάχους και σύστασης των 5 μετρήσεων του κάθε υμενίου, με στόχο την λήψη μια και μόνο αντιπροσωπευτικής τιμής για το κάθε υμένιο. Έπειτα, εξετάστηκε η επίδραση α) των διαφορετικών ροών και αντιδραστηρίων και β) της θερμοκρασίας στο πάχος και την σύσταση των παραγόμενων υμενίων.

Για μεταβλητή παροχή οξυγόνου, με σταθερή παροχή αμμωνίας και TDMSA και θερμοκρασία απόθεσης 650°C παρατηρήθηκαν τα εξής:

- Η απόθεση ξεκινάει σε απόσταση 17 εκατοστών από την είσοδο του αντιδραστήρα, κάτι που αντιστοιχεί σε θερμοκρασία 530°C για το δείγμα.
- Μεγαλύτερες παροχές οξυγόνου προκαλούν αύξηση στον συνολικό ρυθμό απόθεσης.
- Ο μέγιστος ρυθμός απόθεσης παρατηρείται πλησιέστερα στην έξοδο του αντιδραστήρα για αυξημένη παροχή οξυγόνου, ενώ δεν παρατηρείται μέγιστο για το πείραμα που διεξήχθη απουσία οξυγόνου.
- Η ενσωμάτωση αζώτου στα υμένια ξεκινάει σε απόσταση 22 εκατοστών από την είσοδο του αντιδραστήρα, απόσταση που αντιστοιχεί σε θερμοκρασία 610°C
- Η περιεκτικότητα των υμενίων σε άζωτο εξαρτάται από την παροχή οξυγόνου στον αντιδραστήρα. Συγκεκριμένα, αυξημένη παροχή οξυγόνου προκαλεί μείωση στην περιεκτικότητα αζώτου στα τελικά φιλμ.
- Το μέγιστο της περιεκτικότητας σε άζωτο για το κάθε πείραμα εμφανίζεται στο τελευταίο δείγμα του αντιδραστήρα (αυτό που βρίσκεται πιο κοντά στην έξοδο)

Τα ίδια αποτελέσματα λαμβάνονται για πειράματα με μεταβλητή παροχή οξυγόνου και απουσία αμμωνίας. Παρατηρείται ενσωμάτωση αζώτου παρά την έλλειψη αμμωνίας στην αέρια φάση, κάτι που υποδηλώνει ότι η βασική πηγή αζώτου για το υμένιο είναι το μόριο της πρόδρομης ένωσης, TDMSA.

Στην συνέχεια εξετάστηκε η επίδραση της παροχής αμμωνίας, για σταθερή παροχή προδρόμου, οξυγόνου και θερμοκρασία απόθεσης 650°C. Έγιναν οι εξής παρατηρήσεις:

- Αύξηση της παροχής αμμωνίας προκαλεί πτώση του γενικού ρυθμού απόθεσης. Το μέγιστο του ρυθμού απόθεσης παρατηρείται σε παρόμοια τοποθεσία εντός του αντιδραστήρα για όλες τις παροχές αμμωνίας που ελέγχθηκαν. Παρόλα αυτά, η αυξημένη παροχή αζώτου μειώνει την ενσωμάτωση αζώτου στα υμένια.
- Η ενσωμάτωση αζώτου στα υμένια ξεκινάει πάλι σε απόσταση 22 εκατοστών από την είσοδο του αντιδραστήρα (610°C).

Αυξημένη παροχή TDMSA προκαλεί μεγαλύτερη ενσωμάτωση αζώτου στα υμένια, ενώ δεν επηρεάζει σημαντικά τον ρυθμό απόθεσης. Το μέγιστο απόθεσης εμφανίζεται σε τοποθεσία πιο κοντινή στην είσοδο του αντιδραστήρα για αυξημένη παροχή TDMSA, κάτι που αποτελεί ένδειξη της γρήγορης κατανάλωσης του οξυγόνου στην αέρια φάση.

Η μείωση της θερμοκρασίας απόθεσης στους 625°C, προκαλεί πτώση του ρυθμού απόθεσης, κάτι που ήταν αναμενόμενο, λόγω του ενδόθερμου χαρακτήρα της αντίδρασης διάσπασης της πρόδρομης ένωσης. Επίσης, μειώνει την ενσωμάτωση αζώτου στα υμένια.

Με την μέθοδο της υπέρυθρης φασματοσκοπίας με μετασχηματισμό Fourier, εξετάστηκαν 6 δείγματα ανά πείραμα, ώστε να εξεταστεί η επίδραση της θέσης του δείγματος στα χαρακτηριστικά του. Κάθε δείγμα εξετάστηκε σε ένα μοναδικό σημείο. Το σημείο αυτό είχε ήδη αναλυθεί μέσω της ελλειψομετρίας, ώστε κάποια συσχέτιση να είναι δυνατή. Οι αναλύσεις έγιναν μέσω μιας συσκευής Perkin Elmer Frontier που λειτουργούσε στο μέσο υπέρυθρο φάσμα (MIR). Τα δείγματα αναλύθηκαν υπό γωνία 60°, ώστε να γίνει δυνατή η εκμετάλλευση του Berreman Effect. Τα ληφθέντα φάσματα χωρίστηκαν σε δύο κύριες περιοχές ενδιαφέροντος, α) την “hydrated area” μεταξύ 3600 και 2700 cm^{-1} στην οποία παρατηρούνται οι διάφορες δονήσεις που μαρτυρούν την παρουσία υδρογόνου και υδροξυλίων στο υμένιο. Η δεύτερη περιοχή, β) η “fingerprint region”, μεταξύ 1300 και 650 cm^{-1}, δίνει πολύ χρήσιμες πληροφορίες για την δομή των υμενίων. Σε αυτή την περιοχή, μπορούν να παρατηρηθούν δονήσεις σχετικές με δεσμούς Si-N, Si-O, Si-C. Λόγω πληθώρας δεσμών και στις δύο περιοχές, ήταν αναγκαία η αποσυνέλιξη τους, ώστε να μπορούν να παρατηρηθούν επιμέρους περιοχές. Οι κορυφές των οποίων η εξέλιξη εξετάστηκε ήταν οι δονήσεις έκτασης $Si\text{-}CH_3$, Si-O-Si και Si-N.

Παρατηρήθηκε ότι η χρήση μειωμένης παροχής οξυγόνου, προκαλεί μετατόπιση των παραπάνω κορυφών προς χαμηλότερους κυματαριθμούς. Αυτό είναι ένδειξη αυξημένης παρουσίας αζώτου στα υμένια. Επίσης η παροχή οξυγόνου ήταν αυτή που καθόριζε τον χαρακτήρα των υμενίων. Συγκεκριμένα, όσο λιγότερη ήταν η συγκέντρωση του οξυγόνου στην αέρια φάση, τόσο πιο έντονο χαρακτήρα νιτριδίου του πυριτίου είχαν τα ληφθέντα φάσματα. Για υψηλές συγκεντρώσεις οξυγόνου στην αέρια φάση, τα φάσματα είχαν χαρακτήρα κοντινότερο σε αυτόν της πυριτίας. Αυτό το φαινόμενο ήταν ιδιαίτερα έντονο για τα πειράματα όπου χρησιμοποιήθηκαν πολύ χαμηλές παροχές οξυγόνου.

Τα φάσματα επίσης, έδειξαν πολύ χαμηλή απορρόφηση στις διάφορες κορυφές που αντιστοιχούν σε δεσμούς Si-H. Συνεπώς, μπορεί να γίνει η παραδοχή ότι η πλειοψηφία του υδρογόνου που βρίσκεται εντός των υμενίων βρίσκεται στους δεσμούς Si-OH, N-H, H-OH, =CH2 και $-CH_X$.

Επίσης, η χρήση της ανάλυσης FTIR στο πείραμα στο οποίο έγινε χρήση μόνο της πρόδρομης ένωσης ή χρήση της πρόδρομης ένωσης με πολύ μικρή παροχή οξυγόνου (0.3 sccm) για την διεργασία απόθεσης, τόνισε την ανάγκη για την υιοθέτηση ενός νέου ελλειψομετρικού μοντέλου, το οποίο θα προσεγγίζει και την περιεκτικότητα του φιλμ σε άνθρακα.

Τέλος, αξίζει να αναφερθεί ότι η πολυπλοκότητα της πρόδρομης ένωσης είναι εμφανής στα παραγόμενα υμένια. Τα υμένια εμφανίζουν πληθώρα χημικών δεσμών, και αρκετές χαρακτηριστικές ομάδες που περιέχουν άνθρακα. Η αυξημένη ύπαρξη ομάδων άνθρακα και ειδικά -CH_3, δίνει την εντύπωση ότι τα υμένια είναι της μορφής SiO_xN_y:CH_3.

Χρησιμοποιώντας τα διαθέσιμα αποτελέσματα από της μεθόδους ανάλυσης δέσμης ιόντων για τα ποσοστά πυριτίου (μέσω RBS), οξυγόνου, αζώτου, άνθρακα (μέσω NRA) και υδρογόνου (μέσω ERDA) εντός των υμενίων ήταν δυνατή η επιβεβαίωση των τάσεων που αναφέρθηκαν παραπάνω. Εκτός αυτού, έγινε δυνατή η βαθμονόμηση ενός δεύτερου μοντέλου για την ελλειψομετρία. Πρόκειται για ένα κατά Bruggeman effective medium approximation model, το οποίο όμως υπολογίζει 3 φάσεις. Μια φάση πυριτίας (SiO_2), μια φάση νιτριδίου του πυριτίου (Si_3N_4) και μια φάση που θεωρείται ως φάση άμορφου άνθρακα. Το μοντέλο αυτό έδωσε ικανοποιητικά αποτελέσματα όταν ελέγχθηκε για κάποια άλλα δείγματα. Παρόλα αυτά πρέπει να ελεγχθεί σε μεγαλύτερη γκάμα δειγμάτων, για τα οποία υπάρχουν διαθέσιμα ακριβή δεδομένα σύστασης.

Τα διαθέσιμα αποτελέσματα από τις μεθόδους IBA, επιβεβαίωσαν ότι η αυξημένη παροχή οξυγόνου οδηγεί σε υμένια φτωχά σε άζωτο και άνθρακα Αυτό μπορεί να οφείλεται στο ότι το άζωτο και ο άνθρακας ενσωματώνονται στα υμένια μέσω των ίδιων ενδιάμεσων. Μπορεί επίσης να σημαίνει ότι η αυξημένη παροχή οξυγόνου μειώνει της ομάδες μεθυλίων που βρίσκονται στα ενδιάμεσα στην αέρια φάση, οδηγώντας έτσι σε υμένια φτωχά σε άνθρακα. Επίσης επιβεβαίωσαν ότι οι χαμηλές θερμοκρασίες εμποδίζουν την ενσωμάτωση αζώτου στα υμένια. Επιβεβαιώθηκε επίσης, ότι η αυξημένη παροχή αμμωνίας εμποδίζει την ενσωμάτωση αζώτου στα υμένια. Παρόλα αυτά η χρήση αυξημένης παροχής αμμωνίας οδηγεί σε εξαιρετικά χαμηλά ποσοστά άνθρακα εντός των υμενίων, κάτι που πιθανότατα οφείλεται στην διάσπαση των ομάδων μεθυλίου από τα υμένια λόγω της αμμωνίας. Τέλος, οι μέθοδοι IBA κατέδειξαν σημαντικά ποσοστά υδρογόνου εντός των υμενίων, κάτι, που σε συνδυασμό με τα αποτελέσματα του FTIR, υποδεικνύει μεγάλη συγκέντρωση ειδών N-H, Si-OH and CH_x εντός των υμενίων.

Μέσω της μεθόδου χημικής χάραξης με την χρήση διαλύματος (6:1) BOE, προκύπτουν συμπεράσματα για την συμπεριφορά των υμενίων ενάντια στην διάβρωση. Συγκεκριμένα, παρατηρήθηκε ότι το ατομικό ποσοστό αζώτου των υμενίων είναι ο πιο σημαντικός παράγοντας που επηρεάζει την αντίσταση στη διάβρωση. Συγκεκριμένα, υμένια με πάνω από 8% ατομική σύσταση σε άζωτο εμφάνισαν εξαιρετική απόδοση, ανεξάρτητα από τις συνθήκες κάτω από τις οποίες παράχθηκαν. Τα δείγματα αυτά εμφάνισαν ρυθμό διάβρωσης χαμηλότερο από 1 A/s. Δεν εντοπίστηκε κάποια συσχέτιση μεταξύ της θέσης της κορυφής Si-N με τον ρυθμό διάβρωσης, παρόλα αυτά εντοπίστηκε συσχέτιση μεταξύ της θέσης της κορυφής Si-O με τον ρυθμό διάβρωσης. Συγκεκριμένα, ο ρυθμός διάβρωσης μειώνεται όσο η θέση της κορυφής Si-O μετατοπίζεται προς χαμηλότερους κυμματαριθμούς. Αυτό δείχνει ότι η αύξηση του ενσωματωμένου αζώτου μετατοπίζει την κορυφή προς χαμηλότερους κυμματαριθμούς και ταυτόχρονα βελτιώνει την αντίσταση στην διάβρωση μειώνοντας τον ρυθμό διάβρωσης.

Η μελέτη των παραγόμενων υμενίων, η οποία ήταν ο σκοπός της παρούσας εργασίας, ήταν μεγάλης σημασίας για πολλούς τομείς του ερευνητικού προγράμματος. Βοήθησε τόσο στην λήψη αποφάσεων για την επιλογή νέων πειραματικών παραμέτρων. Όπως προαναφέρθηκε η μελέτη των υμενίων που παράχθηκαν μόνο με την χρήση της πρόδρομης ένωσης οδήγησε στην υιοθέτηση ενός χημικού συστήματος χωρίς αμμωνία στα υπόλοιπα πειράματα. Μετά από αυτό το πείραμα, ο ρυθμός απόθεσης και η επιθυμητή ενσωμάτωση αζώτου στα υμένια καθοριζόταν μεταβάλλοντας μόνο τον λόγο της παροχής του οξυγόνου προς την παροχή της πρόδρομης ένωσης. Αυτός ο λόγος φαίνεται να έχει την μεγαλύτερη επίδραση στις τελικές ιδιότητες των υμενίων. Επίσης, η πληθώρα δεδομένων πάχους και σύστασης που εξήγαγε αυτή η μελέτη, βοήθησε σημαντικά στην εξέλιξη του χημικού μοντέλου και στην προσομοίωση της διεργασίας.

List of figures

1. Introduction

The work of this thesis was performed in the premises of the CIRIMAT laboratory, found inside the ENSIACET building located at 4 Allée Emile Monso, 31030 Toulouse, France. This work was part of the HEALTHYGLASS project, financially supported by the Agence nationale de la recherché (ANR).

HEALTHYGLASS will determine innovative, thermally activated metalorganic chemical vapor deposition (MOCVD) processes of amorphous silicon oxide (SiO_2) oxynitrides (SiO_xN_y) and oxycarbides (SiO_xC_y) deposited on complex 3D-substrates, and will define their appropriate composition and structural characteristics in order to obtain efficient and sustainable barrier properties. The targeted function of these coatings is to limit the interaction between the substrate and the potential aquatic solution it will come in contact with, , and thus allow to new advanced applications in microelectronics, pharmaceutics, and other sectors.

There is limited information in the literature on the deposition of SiO_2, SiO_xN_y and SiO_xC_y films with respect to the specifications defined by the project, namely atmospheric pressure and moderate deposition temperature (<570 °C), leading to dense and chemically inert films deposited on confined surfaces at high growth rate. The project team has recently tuned a thermal CVD deposition process of SiO_2 at the internal surface of vials from mixtures of tetraethyl orthosilicate (TEOS) and oxygen. However, these films presented corrosion resistance insufficient in challenging the state of the art. In the frame of this project SiO_xN_y and SiO_xC_y will be processed from organosilicon precursors, such as TEOS and reactive compounds which will activate radical mechanisms to enrich the films with nitrogen and carbon. CVD of SiO_2 will be first investigated as starting point prior focusing on SiO_xN_y and SiO_xC_y which present remarkable barrier properties due to the densification of the network obtained from the partial replacement of O anions by highly coordinated N and C ones.

State of the art protocols for the physico-chemical, structural and mechanical characterization, including microscopy, ellipsometry, nuclear and vibrational spectroscopies, atom probe tomography and nanomechanics tests, will provide information on these complex systems, including details on their surface and their interface with the glass substrate. The quantification of the connectivity of the silicate network, the structural disorder, the distortion of the Si environment, and the distribution of the oxynitrides and oxycarbide species will be monitored by solid state ^{29}Si and ^{13}C NMR, combined with XPS and µ-FTIR. High resolution

^1H NMR and the very recent and challenging Dynamic Nuclear Polarization will reveal the hydrated species which are present on or by the surface.

The hydrolytic resistance and the durability of the coatings will be evaluated by primary etching tests, utilizing hydrofluoric solutions widely used in the literature. The most resistant samples will then be identified, and application-oriented 3D substrates will be coated and then tested in more severe conditions, e.g. ageing over a period of several weeks in basic and acid pH solutions. The releasing and corrosion mechanisms will be investigated and correlations among process conditions, structure and barrier properties will be established.

HEALTHYGLASS will establish process/structure/properties/performance correlations which will lead to outstanding progress at fundamental level and will pave the way towards the application of these multifunctional and durable materials in many sectors concerned by the functionalization of complex surfaces such as micro- and nano-electronics, plastics, medical devices and implants, or gas sensors.

The purpose of this thesis was to provide results regarding the composition and structure of the produced silicon oxynitride films. This results in turn were able to:

a) contribute to the establishment of the process-structure-properties-performance correlation in the frame of the HEALTHYGLASS ANR project
b) help decide the conditions of subsequent thin oxynitride film production experiments
c) to provide satisfactory input data for the development of the chemical model and the process simulation.

My work in the project involved the compositional and structural analysis of the thin films produced using a trisdimethylsilylamine (TDMSA) – oxygen (O_2) – ammonia (NH_3) chemical system. The main methods used were Ellipsometric Spectroscopy, and Fourier Transformation Infrared Spectroscopy (FTIR). The family of Ion Beam Analysis (IBA) methods (RBS, NRA and ERDA) were considered and some of their results will be presented in this work. However, it should be noted that these analyses were either performed by other members of the consortium or outsourced to external partners.

This present thesis will elaborate on the methods used for the solid phase analysis. The theoretical part will provide information regarding the techniques used, while the experimental part will explore the methods and the metrology followed for the probing of the samples. In the Results and Discussion sections the findings of the above characterizations will be presented and discussed, respectively. Finally, in the Conclusions and Suggestions section the overarching outcomes of this thesis will be synopsized, and suggestions will be made as proposals for future research relating to the HEALTHYGLASS project.

2. Theoretical Part

2.1 Ellipsometry

2.1.1 Basic principle

Ellipsometry is a non-destructive method that enables the measurement of the produced films' thickness and optical properties. This spectral acquisition is made possible because of the following phenomenon: When a light beam of a known wavelength and a known polarization state is incident to the surface of an isotropic sample, then the incident light obtains a different state of polarization, an elliptical one. The properties of the new elliptical state of polarization depend on the properties of the film, as well as on the properties of the light [1]. In order to make the measurements and the analysis more convenient, the ratio ρ of the Fresnel p- and s- polarized light amplitude reflection coefficients (r_p and r_s) has to be introduced [2], where the s-component is perpendicular and the p-component is parallel to the incidence plane:

$$\rho = \frac{r_p}{r_s} \tag{1}$$

Both r_p and r_s are complex numbers, which means that the ratio is also a complex number. This number is in turn expressed in terms of Ψ and Δ, where Ψ is the amplitude component, and Δ is the phase difference. This leads to the fundamental ellipsometry equation [1]:

$$\rho = \tan(\Psi) * \exp\,(i\Delta) \tag{2}$$

The amplitude of the ratio of the polarized light reflection coefficients is expressed by $\tan(\Psi)$ while the phase shift between p- and s- light is given by Δ [1]. Ψ and Δ are the raw values directly measured by ellipsometry.

Spectroscopic Ellipsometry is vastly used for the scope of this work. Measurements are taken for a range of several light wavelengths, enabling an increase to the efficiency of the method, since they help obtain additional information regarding the sample. One can extract several optical properties of the studied material for a wide range of wavelengths [2].

2.1.2 Ellipsometry models and equations

To correlate the raw values that were obtained by ellipsometry with the thickness and optical properties of the films, the introduction of a model is needed. The data are then fitted to the model, providing results regarding the macroscopic properties of the film (thickness, refractive index, composition, etc.).

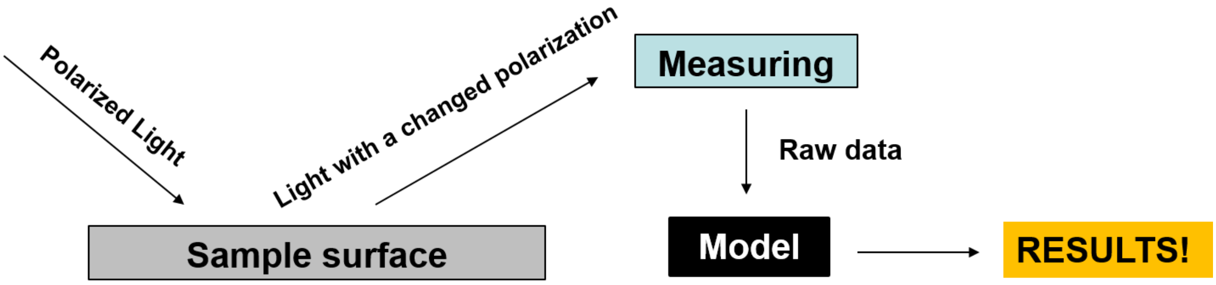

Figure 1: A simple roadmap of the ellipsometry analysis.

For the scope of this work, two different Bruggeman Effective Medium Approximation Models (BEMA) were used. Effective Medium Approximation (EMA) models are able to provide information regarding not only the thickness, the refractive index *n* and the dielectric constant *k* of films, but also information regarding the volumetric fractions f_i of the composite materials that are considered to make up the processed films.

Due to the presence of carbon in the films, two different BEMA models were used:

1. A simple 2 phase model, which took a SiO_2 and a Si_3N_4 phase into account and can give a close and fast approximation of the nitrogen content of the film
2. A more complex 3-phase model, which took a SiO_2, a Si_3N_4 and an amorphous carbon phase into account. This model gives a better carbon content approximation and with the correct assumptions made (based on available IBA results) regarding the carbon phase can also provide a good nitrogen content approximation.

Based on the volumetric fractions obtained for each phase of the film, the molecular fractions of the film can be calculated, based on assumptions made for the properties of each phase. For the 2-phase model the assumptions made were the following:

Table 1: Assumptions made for the 2-phase BEMA model

Phase	Density (g/cm^3)	MR (g/mol)
SiO_2	2.65	60.08
Si_3N_4	3.17	140.283
Carbon	-	12

Then by taking the respective volumetric fraction f_1 and f_2 of each phase, if we consider v_1 and v_2 as the actual volume of each phase, Mr_1 and Mr_2 the molecular weights and d_1 and d_2 the density of each phase, we can calculate the respective molar fractions x_1 and x_2 by using the following equations:

$$f_1 + f_2 = 1 \tag{3}$$

$$f_1 = \frac{v_1}{v_1+v_2} \tag{4}$$

$$x_1 + x_2 = 1 \tag{5}$$

Taking (3), (4) and (5) into account:

$$f_1 = \frac{(x_1*\frac{Mr_1}{d_1})}{((x_1*\frac{Mr_1}{d_1})+(1-x_1)*\frac{Mr_2}{d_2})} \tag{6}$$

Solving (6) for x_1 :

$$x_1 = \frac{f_1*Mr_1*d_1}{Mr_1*d_2-f_1*Mr_1*d_2+f_1*Mr_2*d_1} \tag{7}$$

This way, the molar fraction of Si_3N_4 in the film can be calculated, and thus the nitrogen content of the film.

For the 3-phase model, a similar approach was used. The model was simplified by considering two phases: (a) an oxynitride phase (consisting of SiO_2 and Si_3N_4) and (b) a carbon phase. This way, the equations (3), (4), (5), (6) and (7) can be used. However, an average density and an average molecular weight for the oxynitride phase must be calculated. This was done by using the following equations:

$$d_{avg} = f_{SiO_2} * d_{SiO_2} + f_{Si_3N_4} * d_{Si_3N_4} \tag{8}$$

$$Mr_{avg} = \frac{f_{SiO_2}*d_{SiO_2}*Mr_{SiO_2}+f_{Si_3N_4}*d_{Si_3N_4}*Mr_{Si_3N_4}}{d_{avg}} \tag{9}$$

Then the molecular fraction of the Silicon Oxynitride phase could be calculated:

$$f_{SiO_xN_y} = f_{SiO_2} + f_{Si_3N_4} \tag{10}$$

$$x_{SiO_xN_y} = \frac{d_{avg}*\frac{f_{SiO_xN_y}}{Mr_{avg}}}{d_{avg}*\frac{f_{SiO_xN_y}}{Mr_{avg}} + d_{carbon}*\frac{f_{carbon}}{Mr_{carbon}}} \tag{11}$$

Where Mr_{carbon} = 12 g/mol. The density of the carbon phase is fitted to the IBA results, in order to obtain at.% values for carbon and nitrogen that correspond to the respective ones measured by IBA, validating as such the ellipsometric 3-phase model.

2.2 Infrared Spectroscopy

2.2.1 Introduction

The infrared (IR) area of the electromagnetic spectrum contains radiation of wavenumbers between 12800 and 10 cm^{-1}. This large range of radiation, is generally divided into three distinct ranges, based on the different uses of each range. The three distinct ranges of the infrared spectrum are the following [3]:

- The near infrared (NIR), with wavenumbers between 12800 and 4000 cm^{-1}.
- The middle infrared (MIR), with wavenumbers between 4000 and 200 cm^{-1}.
- The far infrared (FIR), with wavenumbers between 200 and 10 cm^{-1}.

The most valuable applications of the NIR spectral region have been in the quantitative analysis of agricultural and industrial products. The results of the quantitative analysis are used for process control and optimization [3]. In the past, the MIR spectral region was used for the qualitative and structural analysis of organic molecules, based in the absorption spectra. However, with the introduction of Fourier Transformation Infrared Spectroscopy (FTIR), the MIR spectral region has found many more uses, including the quantitative analysis of complex compounds and the analysis of the surface and bulk of solids [3]. The FIR spectral region, while potentially quite useful, has only been made accessible by the introduction of FTIR spectrometers [3].

In IR spectroscopy, a linear wavenumber scale is preferred over the use of wavelength. This is because wavenumbers are proportional to frequency and energy. The frequency of the radiation that is absorbed in IR spectroscopy, is that of the molecular vibration that takes place. The following equation shows the correlation between wavelength λ and wavenumber v:

$$v(cm^{-1}) = \frac{10^4\left(\frac{nm}{cm}\right)}{\lambda(nm)} \tag{12}$$

IR radiation is not potent enough to cause electronic transitions to the molecules, in contrast with X-ray radiation for example. For this reason, it is associated with several molecular species whose different vibrational and rotational states can all be found inside a small energy range. For a molecule to absorb in the IR range, its dipole moment must be altered, because of its vibrational or rotational movement. Only then can differences in the amplitude of a certain movement of the molecule be observed, due to the interaction with the electric component of the IR radiation. When the frequency of the radiation matches a natural vibrational frequency of the molecule, then the molecule absorbs the radiation and undergoes a change in the amplitude of its movement [3]. However, that means that the absorption of IR radiation by molecules like O_2, N_2 and Cl_2 is not possible. For these homonuclear atoms, the dipole moment stays constant during vibrational or rotational movements, prohibiting the absorption of IR radiation.

2.2.2 Types of molecular vibrations

The position of the atoms of a molecule is not fixed. Instead, the relative position of the atoms is always changing through different vibrational or rotational movements. The tracking of the several movements and their correlation with the energies of absorption is easier for molecules with a small number of atoms, however it becomes increasingly difficult as the number of atoms in a molecule increases. The larger the molecule, the more the possible vibrations and interactions between atoms, which have to be taken into account [3].

There are two main types of vibrations observed in molecules: Stretching vibrations and bending vibrations. When the distance between two atoms along the axis of their bond is continuously fluctuating, then the vibration is defined as a stretching vibration. There are two types of stretching vibrations: a) the asymmetrical and b) the symmetrical stretching mode. Bending vibrations are characterized by change in the bond angle between two atoms. There are four types of bending vibrations: a) the wagging vibration, b) the rocking vibration, c) the scissoring vibration and d) the twisting vibration. The difference between these types of bending vibration is the plane where the bending occurs. This is visualized in the figure below:

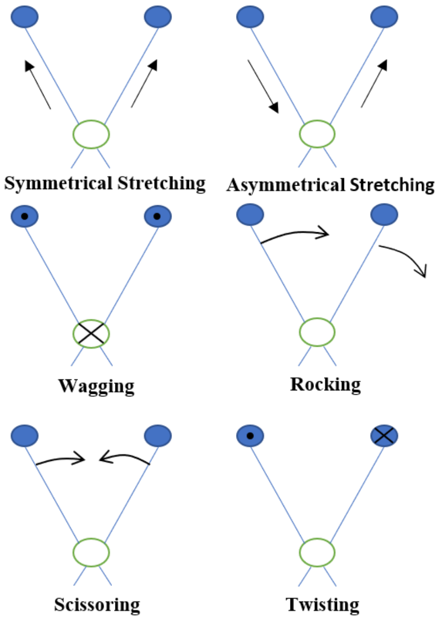

Figure 2: Summary of the different types of molecular vibrations. The x symbol indicates movement away from the reader. The dot symbol indicates movement towards the reader.

For molecules containing more than 2 atoms, the presence of the whole range of vibrations discussed above is possible. This can cause various interactions between the atoms or also a coupling of the vibrations [3]. Sometimes, several vibrations may have similar vibration energies. When analysing the results, this can lead to fewer visible peaks, than those that are expected, due to an overlap of several peaks. This calls for a deconvolution of the resulting bands, so that more precise results can be obtained.

2.2.3 Prediction of the number of vibrations

As mentioned before, when the number of atoms present in the atoms is small, it is easy to predict the number of possible vibrations that can be observed. However, when the number of atoms inside the molecule increases, this prediction is not as simple. Several atoms and different types of bonds might be present inside the molecule, resulting in complex IR spectra. Even then, however, the number of possible vibrations is not that hard to calculate. To locate a point in space, 3 coordinates are required. In order to fix N atoms in place, $3N$ points are needed. When defining the several movements of a molecule, 3 types of movements have to be taken into account [3]:

1. The translational movement of the molecule’s center of gravity.
2. The rotational movement of the molecule around its center of gravity.
3. The different vibrations of each atom present in the molecule.

Since all atoms follow the same translational movement, defining this movement requires 3 degrees of freedom. The same is true for the rotational movement, requiring another 3 degrees of freedom. If we consider that the $3N$ points mentioned above are the total degrees of freedom of the molecule, the possible vibrations for the molecule, are $3N$-6. However, in the case of a linear molecule, the rotation around the bond axis is not possible, making the number of possible vibrations $3N$-5. So, for all types of molecules that contain N atoms (except linear molecules), the possible number of vibrations for the molecule are $3N$-6. For linear molecules, the possible number of vibrations is $3N$-5. Each of these vibrations is called a normal mode [3].

Although predicting the possible vibrations is easy, detecting the actual vibrations in the actual IR spectra is a much more difficult task. It is possible that not all the predicted vibration modes are detected in the IR spectra. This could be due to a plethora of reasons [3]:

1. As mentioned above, it is possible that 2 vibration energies are equal, or almost equal.
2. It is possible that the molecule symmetry prohibits certain vibrations.
3. The vibration energy is found at wavenumbers outside of the instrument’s range.

4. The absorption intensity is too low to be detected by typical methods.

These reasons might hinder the identification of certain molecules, especially if the complexity of the molecule is high. Apart from the above reasons, there are other reasons that influence the wavenumber of certain vibrations. Some vibrations can influence the energy of others, causing a so-called vibrational coupling.

2.2.4 Vibrational coupling

It is possible that the wavenumber of an absorption peak, which is indicative of the vibrational energy, can be affected by another molecular vibration. Several factors can contribute to this [3]:

1. When an atom is present in two different stretching vibrations, then strong coupling of these vibrations can be observed.
2. For two bending vibrations to couple, a common bond must exist between the vibrating groups.
3. One stretching and one bending vibration can only couple when the stretching bond is part of the angle that changes due to the bending vibration.
4. The interaction is stronger when the coupled vibrations have similar energies.
5. No coupling can be observed when 2 or more bonds are found between the groups in question.
6. For two vibrations to couple, the vibrating species must be of the same symmetry.

While such interactions make it difficult to detect and validate the existence of certain species inside the molecule, they give the spectrum of each molecule a distinct shape. This in turn, helps with the identification of the molecule [3]. However, when the analyzed molecule is state of the art, and nothing like it has been analyzed before, these effects might hinder the molecule identifying process.

2.2.5 Instruments used for IR spectroscopy

Several instruments have been used for applications that require IR absorption. However, three different types of instruments are mainly utilized for IR absorption [3]:

1. Dispersive spectrophotometers with a grating monochromator.
2. Fourier Transform spectrophotometers with an interferometer
3. Nondispersive photometers using either filters or absorbing gases for the analysis of atmospheric gases.

In the past, and until the 1980s, the most popular category of the above was the first one, however the introduction of Fourier Transform spectrophotometers, has completely dominated the field of far and mid infrared analysis, due to the speed, reliability and signal-to-noise ratio advantage that it provides [3]. For the above reasons, FTIR spectroscopy was used for the analysis of the produced silicon oxynitride thin films.

2.2.6 Fourier Transform Infrared Spectroscopy (FTIR)

While Fourier Transform spectroscopy was first developed by astronomers in the early 1950s in order to isolate the very weak signals that were received from distant stars from the environmental noise [4], since the 1980s it has been the main type of spectroscopy used for IR applications.

There are many advantages that give FT instruments the edge over their competitors. First, FT instruments have few optical components and no slits. That means that the radiation that reaches the detector is greater than in dispersive instruments. This is called the Jacquinot advantage and it generally provides better signal-to-noise ratios in FT instruments than dispersive instruments. However, at longer wavelengths, were the slits in dispersive instruments can have a very wide width, this effect might be in advance of the dispersive instruments [5]. Second, FT instruments have a greater resolving power and a great reproducibility of wavelength. These two factors make the analysis of complex spectra possible. Third, the detector receives all the information found in the radiation at the same time. This makes the acquisition of spectra tremendously quicker, when compared to dispersive instruments. This advantage can lead to the increase of the signal-to-noise ratio, as explained in the paragraph below. Finally, in the case of thin films, FTIR is a non-destructive method of analysis that enables the identification of several chemical species that are contained in the films.

In this study, the infrared spectra acquired are in the wavenumber range of 400-4000 cm^{-1} and resolution elements of 8 cm^{-1} were chosen. That means that a total of 450 individual measurements should be taken. If we had a dispersive instrument and each measurement took 0.25 seconds, then 112,5 seconds would be required for the acquisition of a single spectrum. If a higher spectral detail was necessary, and resolution elements of 4 cm^{-1} were chosen, then the number of measurements and time required for the acquisition of a single spectrum would be doubled. In dispersive instruments, the choice of low-resolution elements would mean the use of narrower slits, something that would decrease the signal to noise ratio. However, the signal-to-noise ratio can be improved by increasing the number of spectra acquired and averaging them. This effect is described by the following equation [4]:

$$\left(\frac{S}{N}\right)_n = sqrt(n) * \left(\frac{S}{N}\right)_i \qquad (13)$$

Where $(S/N)_n$ is the signal-to-noise ratio for the average value of n spectra acquisitions, while $(S/N)_i$ is the signal-to-noise ratio for a single spectrum acquisition. This means that when using a dispersive instrument, and if increased signal-to-noise is required, the only way is the acquisition of a high number of spectra. In order to increase the signal-to-noise ratio by a factor of 4, 16 spectra would need to be averaged, requiring 1800 seconds or 30 minutes for the example stated above. In FTIR spectroscopy, this problem is non-existent, since the number of all measurements for each spectrum are received simultaneously by the detector [4]. If the time required for the acquisition of a whole spectrum through the use of FTIR is 1 second, that would mean that 1800 spectral acquisitions could be achieved during the 1800 seconds that would be required for 16 spectral acquisitions through the use of a dispersive instrument. This would lead to an increase of the signal-to-noise ratio by a factor of 42. This advantage, which is native to FT spectroscopy, is also called Fellgett advantage [5].

A basic FTIR spectral acquisition would be as follows:

1. With no sample in place, the background spectrum is acquired. This is saved in the memory of the computer and will be in turn subtracted from the samples' spectra, in order to exclude the interfering molecules of the environmental air (mainly CO_2 and) H_2O) from the measurement.
2. The spectrum is acquired with the sample in place.
3. The spectra are presented in graphs of absorbance as a function of the wavenumber.

The absorbance (A) of the sample is calculated as follows [6, pp. 1–17]:

$$A = \log\left(\frac{I_o}{I}\right) \qquad (14)$$

Where I_O the intensity of the background spectrum and I the intensity of the acquired spectrum.

Absorbance A is also related to the concentration of molecules in a sample. This is due to the so called Beer's Law [6, pp. 1–17]:

$$A = \varepsilon l c \qquad (15)$$

Where ε the absorptivity of the sample, l the pathlength and c the concentration of a certain species in the sample.

Due to Beer's Law, the height of a certain peak of the absorbance spectra is linearly correlated to the concentration of the species that the peak corresponds to. By using standards to obtain a calibration curve, quantitative analysis is possible in FTIR.

2.2.7 Applications of FTIR

This method can be used for both qualitative and quantitative chemical characterization of all types of samples: solid, gas and liquid. It has been widely used for the characterization of SiO_2 [7]–[9] and Si_3N_4 [10], [11] thin films, as well as for more complex silicon based films, such as silicon oxynitride films [12]–[14] and even SiONC films [15], [16]. It is also used for the determination of several protein structures [17].

To conclude this chapter, the following can be said regarding FTIR and its use for the aims of this project: As mentioned in chapter 2.2.6, FTIR is a non-destructive method of analysis that enables the identification of several chemical species that are contained in the films. Over the years that this method has existed, a vast number of sample spectra have been acquired and analyzed. This means that a wide variety of information regarding the several chemical species' vibrations and their position on an FTIR spectrum are available in the literature. Therefore, information regarding the species present in state-of-the-art films can be extracted.

2.3 Ion Beam Analysis (IBA) methods

The Ion Beam Analysis methods are a group of nuclear methods, which allow the quantitative analysis of the surface layer of thin films [18]. For this thesis, three distinct IBA methods were utilized, namely Rutherford Backscattering Spectroscopy (RBS), Nuclear Reaction Analysis (NRA) and Elastic Recoil Detection Analysis (ERDA).

2.3.1 Rutherford Backscattering Spectroscopy (RBS)

Rutherford Backscattering Spectroscopy is a widely used method for the surface analysis of thin films. For this thesis, RBS was used for the detection of silicon in the films. Its basic principle is the following: The target surface is bombarded with ions; whose energy level is in the MeV (0.5-4 MeV) scale. The energy of the backscattered projectiles is then recorded by an energy detector. The energy of a backscattered projectile E_1 of mass M_1 is given by the following formula:

$$E_1 = k * E_0 \tag{16}$$

where k is the kinematic factor, given by the following equation:

$$k = \frac{M_1^2}{(M_1+M_2)^2}\left\{\cos(theta) \pm \left[\left(\frac{M_2}{M_1}\right)^2 - \sin^2(theta)\right]^{\frac{1}{2}}\right\}^2 \tag{17}$$

where *theta* is the scattering angle, and M_2 the mass of the target nucleus initially. For $M_1 < M_2$, only the plus sign in eq. (17) applies. For $M_1 > M_2$, eq. (17) has 2 distinct solutions.

Based on the energy recorded, conclusions can be made regarding the composition of the material, as well as for its depth profile. A depth profile of the order several nm can be accurately calculated. RBS also provides a good sensitivity (in the order of parts per million) for the quantification of heavy elements. Its downside is that it does not provide accurate calculations for the lighter elements. For this reason, the use of the other two complementary techniques, NRA and ERDA, is necessary [19].

2.3.2 Elastic Recoil Detection Analysis (ERDA)

Elastic Recoil Detection Analysis (ERDA) was used for the detection of hydrogen in the films. It is by many aspects similar to RBS. However, it succeeds in detecting target atoms with a mass of M_2 that recoil after their collision with the bombarding atoms in the forward direction. RBS cannot detect projectiles when $M_1 > M_2$ and since alpha rays are mostly used for these methods, hydrogen cannot be detected. This obstacle is overcome by the ERDA technique, since the energy transferred to the recoil for a fixed incidence angle is determined by the mass of the target nucleus M_2. In this technique, the energy loss of the scattered ion due to the collision and the final energy of the recoil give information for the final energy of the particle detected, allowing the calculations of the collision depth [20].

2.3.3 Nuclear Reaction Analysis (NRA)

Nuclear Reaction Analysis (NRA) is a method that is widely used for the quantitative determination and depth profiling of light elements and isotopes. It was used for the detection of carbon, oxygen, and nitrogen in the films. In the case of RBS, if a light particle is positioned on top of a heavier particle, then the spectrum detected for the heavy particle will overlap that of the lighter particle. This problem is solved by NRA. Its advantage is that it can detect lighter particles compared to RBS. Apart from that, NRA can also provide information regarding the isotopes present in the film, since nuclear reactions are isotope specific. Several types of nuclear reactions can be used for this method, such as particle-particle reactions, particle-γ reactions and particle-neutron reactions [21].

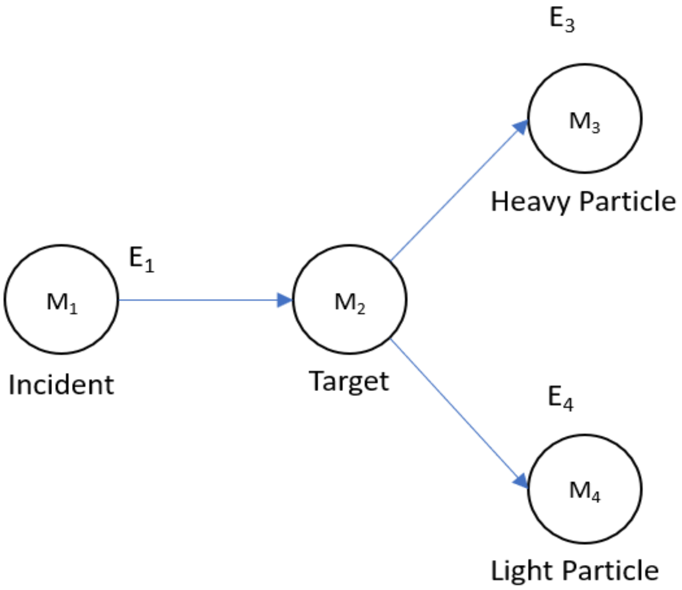

Figure 3: Example of a nuclear reaction observed in NRA.

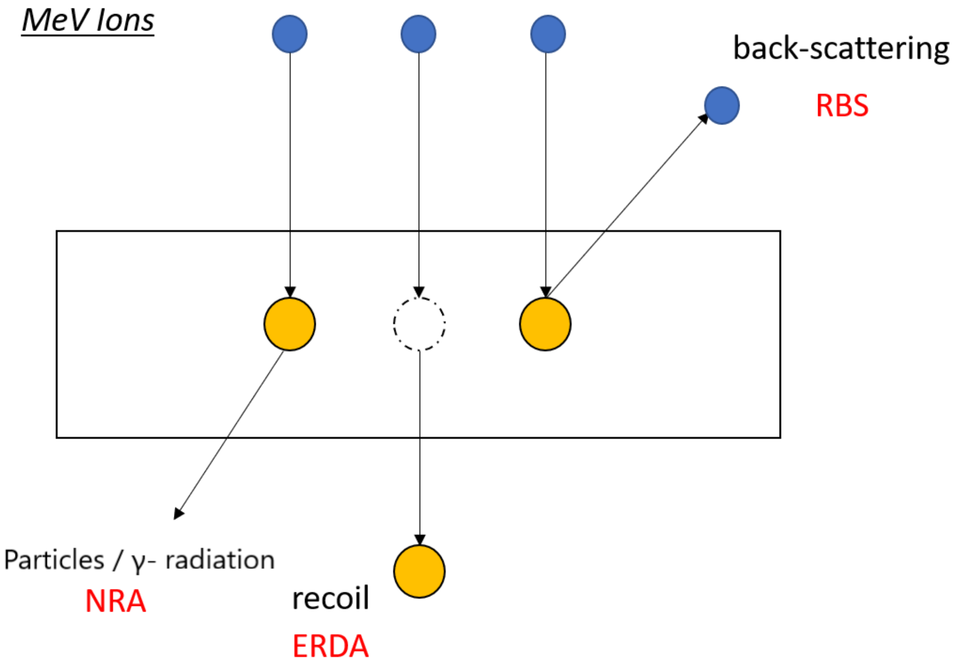

Figure 4: Visualization of the particles detected by each IBA technique used.

2.4 Chemical Vapor Deposition (CVD)

2.4.1 Basic Principle

Chemical Vapor Deposition (CVD) is a chemical process in which the reactants react in the vapour phase near or on a heated substrate and provide solid deposition on its solid surface. The deposition species can be atoms or molecules, or a combination of both. Due to this characteristic, it is classified as a vapor-transfer process [22].

CVD as a process should be examined from many different scopes in order to be optimized. The chemistry of the process, the thermodynamics, as well as the mass and heat transport phenomena taking place should always be taken into account when studying and designing such a process.

For a CVD process to be successful, the activation energy barrier of the required gas phase and solid-gas phase reactions must be overcome. This can be achieved in a variety of ways [22]:

1. Through thermal activation, by using high enough temperatures (sometimes over 900°C depending on the chemistries used)
2. Through plasma activation, which can take place in lower temperatures (e.g. 300-500°C)
3. Through photon activation, usually by using ultraviolet radiation for the activation of the reactants or of several intermediates.

2.4.2 Types of CVD processes

Depending on the way the reactions are activated and the conditions they take place under, the CVD processes can be classified into several categories. Depending on the way of activation type, the processes are categorized as follows:

- When the reactions are thermally activated, then the process is classified as thermal CVD.
- When the reactions are plasma activated, then the process is classified as Plasma Enhanced CVD (PECVD)
- When the reactions are photon activated, then the process is classified as Photon Induced CVD (PHCVD).
- When the reactants are decomposed by a catalytic cracking reaction, the process is classified as Catalytic Chemical Vapor Deposition (Cat–CVD)

Depending on the pressure of the reactor, the processes can be categorized as follows:

- When the process takes place under vacuum, then it is considered a Low-Pressure CVD process (LPCVD).
- When the process takes place under atmospheric (or near-atmospheric) pressure, it is considered an Atmospheric pressure CVD process. (APCVD)

Depending on whether the reactor walls are heated or not, the processes can be categorized as either hot-wall CVD or cold-wall CVD.

Depending on the temperature of the reactor, the processes can be categorized as either low-temperature or high temperature.

As mentioned in section 2.4.1, the thermal activation of several precursors usually requires a temperature higher than 900°C. This leads to several problems, especially when the substrates are sensitive to high temperatures (e.g. glass or plastic substrates). Then, if there are restrictions regarding the use of plasma, which is a reliable way of reducing the process temperature, a practical problem exists. For this reason, several metalorganic precursors are used, in order to reduce the required thermal activation temperature. However, such types of precursors usually have a high vapor pressure, while also being toxic. Thermal CVD processes that use metalorganic precursors are classified as Metalorganic CVD processes (MOCVD). For this project, by using a metalorganic precursor, deposition of a silicon oxynitride material can be observed for temperatures as low as 625°C.

For the scope of this work, the use of a PECVD would seem favorable since the deposition could take place in lower temperatures. This way, the substrate would be thermally unaffected. However, the low temperature at which the deposition takes place for PECVD processes provides a big limitation to the problem. Under the low temperature conditions, the desorption of several by-products and gases from the film would be incomplete. As a result, large quantities of hydrogen could remain as an inclusion in the film. This in turn alters the physical properties of the film, causing vulnerability against chemical etching [22]. Additionally, many PECVD processes require high vacuum, something that leads to a high operational cost and therefore makes the process unattractive for industrial applications. For this reason, a MOCVD process was preferred for the scope of this project.

3. Experimental Part

3.1 Deposition Method

3.1.1 Reactor Properties

The CVD of SiO_xN_y films took place in a horizontal, tubular, hot-wall reactor configuration described in detail in a published work of the HEALTHYGLASS project [23]. The reactor consists of a fused silica tube with an inner diameter of 46 mm and a length of 700 mm, heated by a semitransparent furnace (Trans Temp, Thermcraft Inc.).

280 μm thick monocrystalline silicon (100) wafers (Neyco) were cut in rectangles of 32×24 mm^2 and were used as substrates, after being thoroughly degreased. Inside the reactor, two custom-made, cylindrical, stainless steel substrate holders supported the substrates. These holders had a total length of 450 mm, a 7 mm deep insertion slot, which enabled the vertical support of 18 substrates for each experiment. The first substrate was placed 57 mm away from the reactor inlet.

The CVD reactor inlet consists of four separate gas lines. A N_2 (99.9999%, Messer) dilution line is utilized, whose variable flow allows a constant total gas flow of approximately 4030 sccm across all experiments. This N_2 line was heated at around 100°C. A second N_2 line was used in order to bubble 48 or 147 sccm of N_2 gas through a bubbler system containing the precursor, tridimethylsilylamine (TDMSA), 95%, ABCR). The outlet line of this bubbler was the line that fed the precursor's vapors to the reactor. The bubbler was heated at 80±0.1°C, while the bubbler N_2 line was kept at approximately 95°C to avoid the recondensation of the precursor vapors in the gas phase. An O_2 (99.9995%, Messer) line introduced varying flow rates of O_2. Finally, an NH_3 (99.999%, Linde) gas line introduced varying flow rates of ammonia. All four gas-lines were kept separated and were not mixed until they entered the reactor. The reactor's base and operating pressures were monitored with a Pirani (MKS MicroPirani Transducer Series 925C) and a Baratron (MKS Baratron Type 627) gauges respectively, placed right after the deposition zone and right before a liquid nitrogen trap and a dry pump (Edwards, soXu 20iC). The operating pressure was kept constant at 97.3 kPa (730 Torr) for all runs.

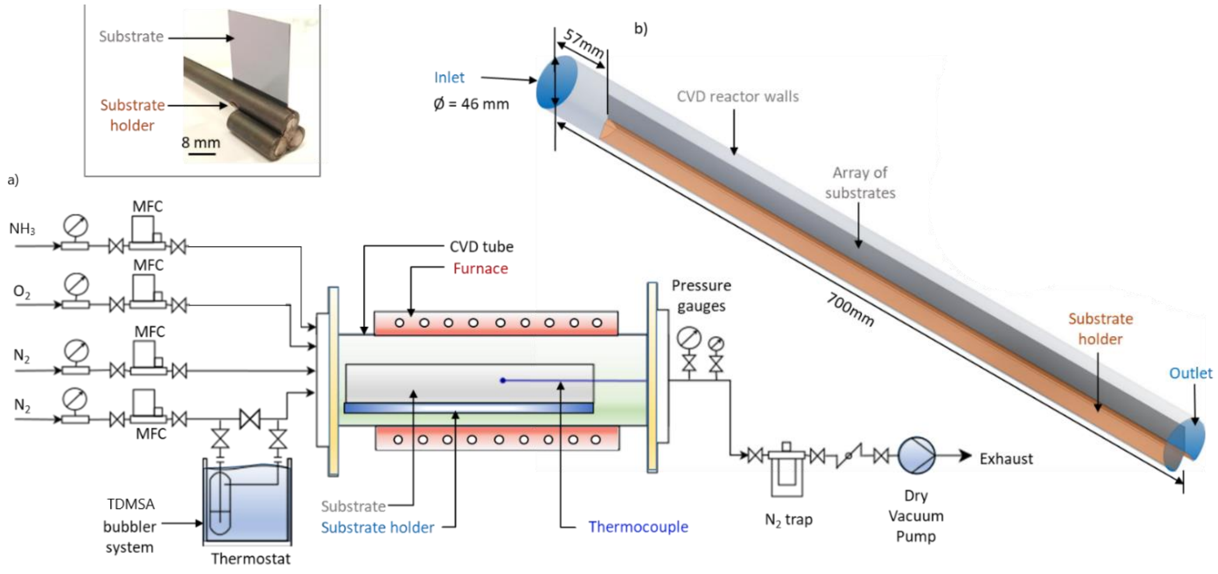

Figure 5: Schematic (a) and 3D (b) representation of the CVD reactor (not true-to-size and proportion). Top left inset photograph shows the substrate holder supporting a Si coupon vertically. Top right inset scheme depicts the symmetry plane, the plotting plane YZ used for surface results presentation and the plotting plane XZ used to present gas phase results [23].

Therman profiles of the reactor were explored at two set point temperatures, namely 625 and 650°C. The wall's temperature profile was measured at 20 mm intervals along the reactor under a N_2 gas flow of approximately 4030 standard cubic centimeters (sccm) using a type-K thermocouple with an accuracy of ±2°C, place at 360 mm from the inlet of the reactor. Two different set point temperatures were used for the reactions, namely 625 and 650°C, defined as the temperature measured at 360 mm from the inlet. An isothermal region can be observed at a distance between 360 and 500 mm from the inlet, as shown in figure 6 below.

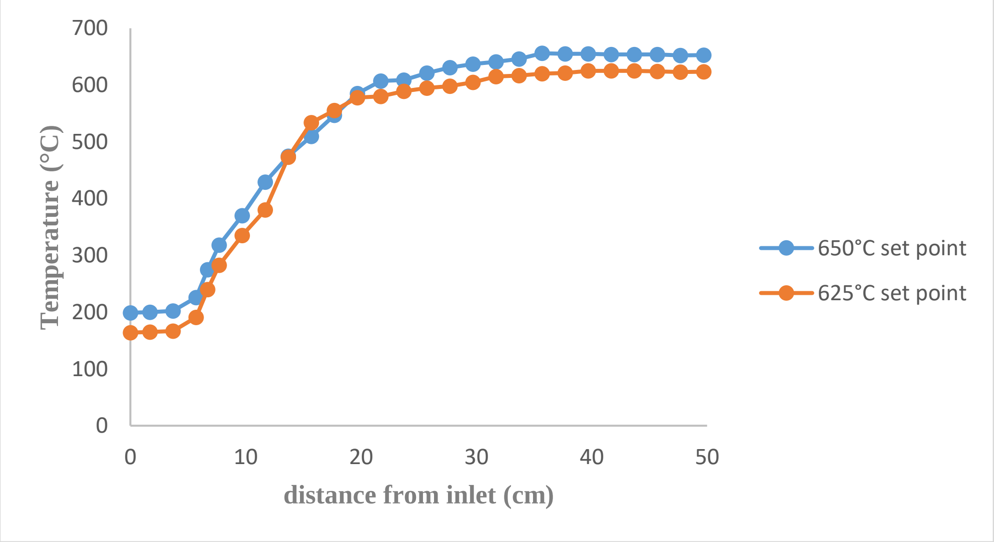

Figure 6: Thermal profile for the two different set points used.

3.1.2 Experimental parameters

Ten runs were performed with a deposition duration ranging from 2.5 h to 5 h, a varying set point temperature and varying reactant flowrates, as summarized in Table 2.

Table 2: Deposition conditions of experimental runs performed in thermal CVD reactor.

Run	**Set Point Temperature (°C)**	**N_2 flow rate through the TDMSA bubbler (sccm)**	**TDMSA flow rate (sccm)**	**O_2 flow rate (sccm)**	**NH_3 flow rate (sccm)**	**N_2 dilution flow rate (sccm)**	**Deposition time (h)**
TD3	650	147	6	2	20	3860	2.5
TD4	650	48	2	2	20	3960	2.5
TD5	650	48	2	0	20	3960	2.5
TD6	650	48	2	0.6	20	3960	2.5
TD7	650	48	2	0.6	0	3980	2.5
TD8	650	48	2	0.6	40	3940	2.5
TD9	650	48	2	0	0	3980	2.5
TD11	650	48	2.67	0.3	0	3980	3.75
TD12	650	48	2	1.2	0	3960	2.5
TD14	625	48	2	0.6	0	3960	5

Experiments TD3 and TD4 were used to examine the influence of the TDMSA flow rate for a set point temperature of 650°C. Experiments TD4 through TD6 were used to examine the influence of the O_2 flow rate under a constant ammonia flow. Experiments TD6 through TD8 were used to examine the influence of the NH_3 flow rate under a constant oxygen flow. Experiments TD7, TD9, TD11 and TD12 were conducted in order to examine the influence of the O_2 flow under constant TDMSA supply and in the absence of NH_3. Between runs TD14 and TD7, the effect of the Set Point temperature was investigated, by fixing all flow rates.

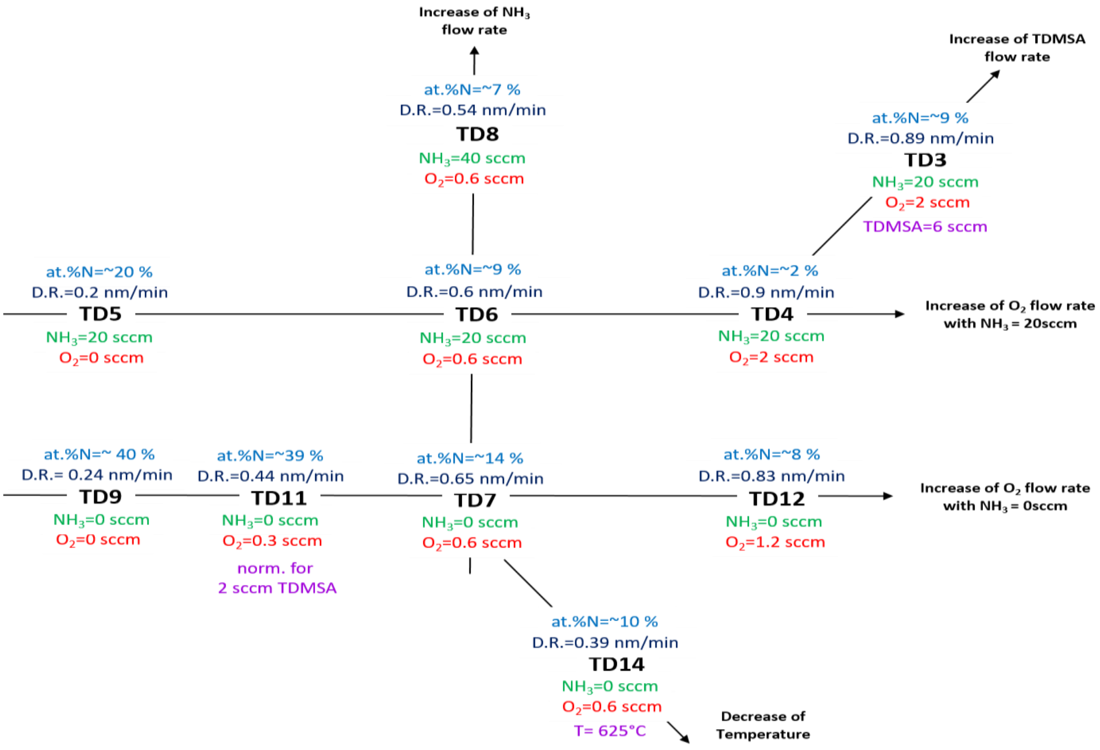

Figure 7: Summary and visualization of the different experiment parameters.

3.2 Characterization Methods

3.2.1 Spectroscopic Ellipsometry

Ellipsometry was utilized in order to obtain accurate local thickness profiles, as well as compositional and refractive index results. A Semilab SE-2000 ellipsometer operating in the 300-1000 nm wavelength range was used.

Figure 8: The Semilab SE-2000 ellipsometer.

The incidence angle was kept constant at 70°. Each sample was probed at 5 points. These 5 points belong on an imaginary line that passes from the center of the sample, as shown in Fig.8. The first point is located 2 mm below the top edge. After that point, 4 more points are probed, with 5 mm intervals.

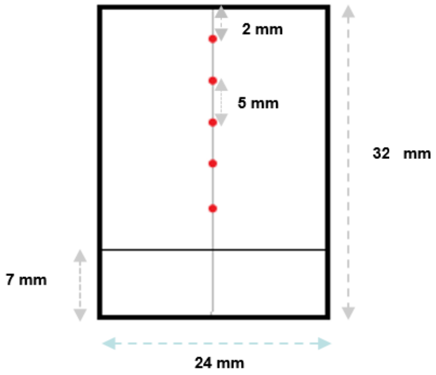

Figure 9: Points on the sample probed by ellipsometry (marked with red dots).

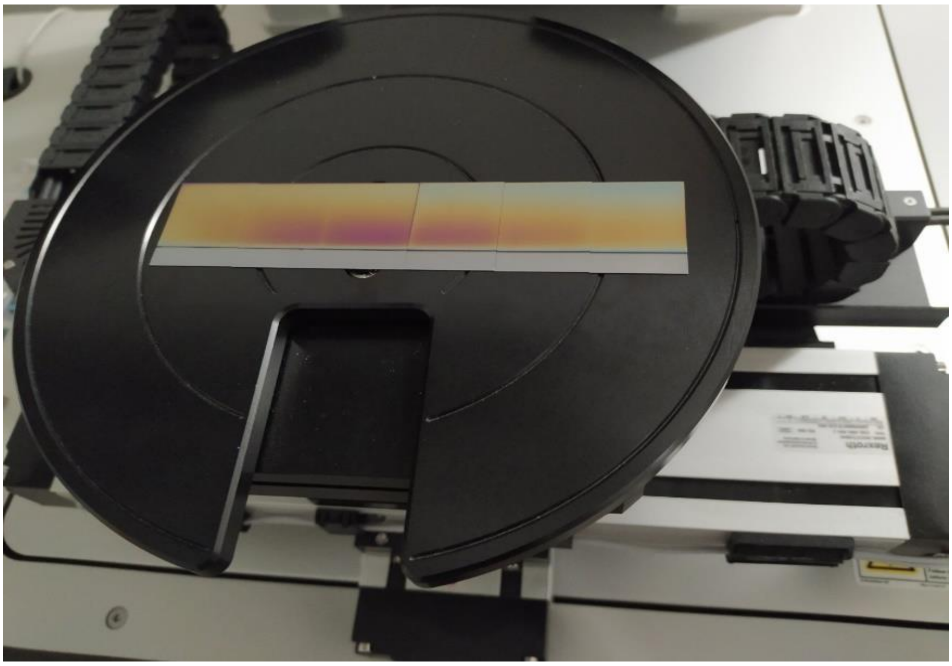

Figure 10: Six different samples ready to be probed.

The spectroscopic ellipsometry data were fitted in the 300-1000 nm wavelength range using the software Semilab SEA. A Bruggeman effective medium approximation model (BEMA) was utilized to extract the measured local thicknesses values, as well as information regarding the composition and refractive index of the films at each point probed. The calculated results were acquired for a R^2 fit of over 0.99. The results of the 5 points of each film were then averaged, providing average thickness, refractive index, and composition values for each sample.

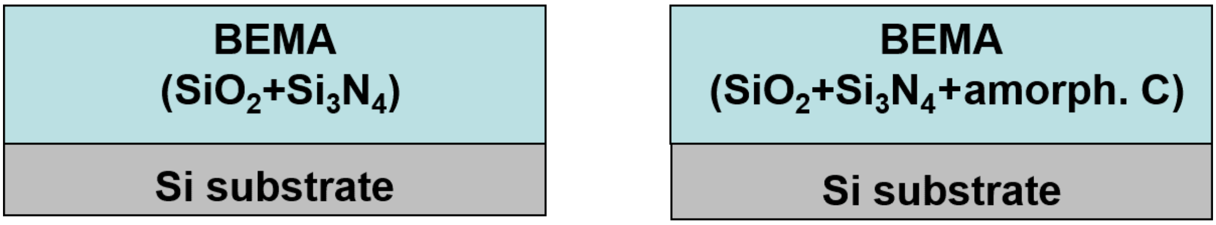

Figure 11: The two different BEMA models used for ellipsometry.

3.2.2 Fourier Transform Infrared Spectroscopy (FT-IR)

FT-IR analysis was used in order to study the resulting film structure of the samples. A Perkin Elmer Frontier FT-IR MIR/NIR spectrometer, equipped with a custom-made substrate holder that enabled the analysis at different incidence angles, was utilized.

Figure 12: The Perkin Elmer Frontier FT-IR MIR/NIR spectrometer.

The spectra were acquired under a 60° angle between the sample and the incident beam, enabling as such the appearance of the different LO3-TO3 pairs, according to the Berreman effect[24]. This effect seems to be strongly evident for the Si-O LO3-TO3 pair in the silica rich films and is an indicator of a predominant silica character when observed. The spectral range between 400-4000 cm^{-1} (MIR) was probed with a resolution of 8 cm^{-1}. Sixty-four spectrum accumulations were taken for each sample, after removal of the background signal. Then, the Si-substrate was probed, and its spectrum was subtracted from the sample spectrum. As a guide for this subtraction, the Si-Si peak ~610 cm^{-1} was used. The factor of the substrate's subtraction was modified until the Si-Si peak's intensity reached zero. Subsequently, the spectra were baseline corrected. Lastly, the resulting spectra were normalized for each sample's thickness, since thickness is a factor that has an effect on the intensity of the spectra, as noted by the Beer-Lambert Law [25].

The exact probed position on the sample is located on the imaginary line that passes from the center of the sample and is the third point that is probed by ellipsometry. The choice of this specific point, combined with the ellipsometry results, can give us more precise information than a randomly chosen point.

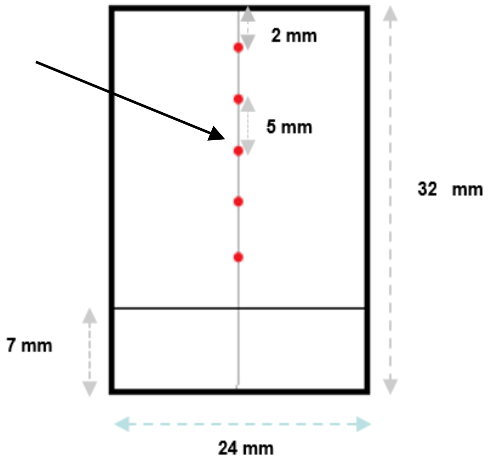

Figure 13: Point that is probed for the FT-IR analyses.

For the initial data manipulation, a Perkin Elmer Spectrograph software (Quantum) bundled with the apparatus was used. However, further data manipulation was needed. The complexity of the material and the different bonds that are contained therein, produce several large bands in the FT-IR spectra. These bands need to be deconvoluted, in order to specify the position and intensity of the underlying peaks. For this task, the Origin 2019 software was used. The spectra were deconvoluted using the NLFit function of the Origin software based on Gaussian curves and the Levenberg Marquardt iteration algorithm. The application of both Lorentzian[26] and Gaussian [27], [28] curves for the deconvolution of such bands is frequently encountered in the literature, with the authors not specifying the particular reasons for these choices. For the scope of the present work, the analyzed spectra seem to be better deconvoluted by Gaussian peaks, and therefore such peaks will be utilized for the processing of the experimental data. The starting points for the deconvolution algorithm were chosen by several visual cues, such as shoulders or peaks that could be observed in the spectra, while also being coherent with the several peak position ranges found in literature. A deconvolution was considered successful if it yielded a value of R^2 higher than 0.98.

3.2.3 Ion Beam Analysis (IBA)

Several Ion Beam Analysis techniques, Rutherford backscattering spectroscopy (RBS), nuclear reaction analysis (NRA) and elastic recoil detection analysis (ERDA) were utilized in order to determine the exact chemical composition of the films. These techniques were housed at the Pelletron facility in CEMHTI, Orléans, France. The analyses were performed by the post-doc researcher Babacar Diallo. These techniques require films with thickness in the range of 100-200 nm.

RBS and NRA were performed at a 166° detection angle with 2 MeV α particles for the former. Oxygen, nitrogen and carbon concentrations were measured through the $^{16}O(d,\alpha_0)^{14}N$, $^{14}N (d,p5)^{15}N$, and $^{12}C(d, p_0)^{13}C$ nuclear reactions respectively, using incident deuterons of 0.9 MeV.

A 2.8 MeV alpha beam was utilized for the ERDA experiments. The sample was positioned at a 15° grazing incidence angle with the recoiled hydrogen getting collected at a scattering angle of 30°. Ten spectra of 1 μC charge were successively collected to get enough repeatability and intensity, and a satisfactory signal/noise ratio was achieved. The strong desorption of hydrogen observed for most samples, presented the need for the individual consideration of the ERDA spectra.

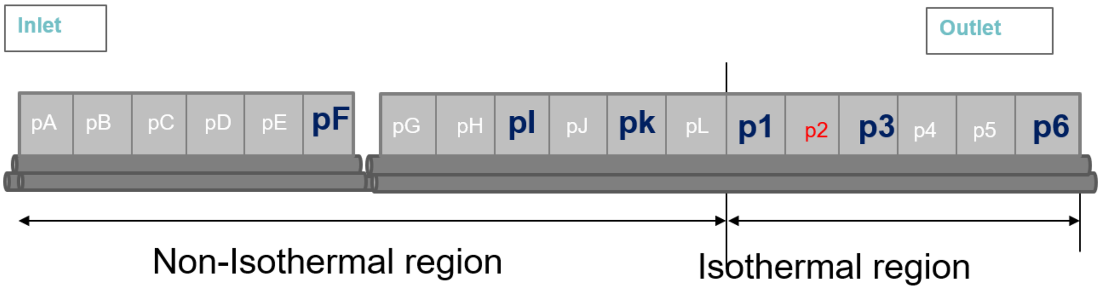

Figure 14: Illustration of the substrate holder. The whole range of samples has been probed by spectroscopic ellipsometry. The samples that have been probed by FTIR are in blue. The samples that have been probed by IBA are in red.

4. Results

4.1 Ellipsometry

As discussed in previous paragraphs, ellipsometry was used to acquire information regarding the samples' thickness and approximate composition.

4.1.1 Effect of the O_2 Flow rate on the produced films

Experiments TD5, TD6 and TD4 were conducted in order to investigate the effect of the O_2 inlet flow rate on the resulting films in the presence of NH_3. For these experiments, the NH_3 inlet flow rate was kept constant at 20 sccm.

First, the above effect on the deposition rate was investigated, using the 2 phase BEMA ellipsometry model. Average values were considered when exploring this effect. That means that the thickness results for the 5 points of each sample were averaged, and then divided by the deposition duration. The results for this set of experiments are presented in Fig.14.

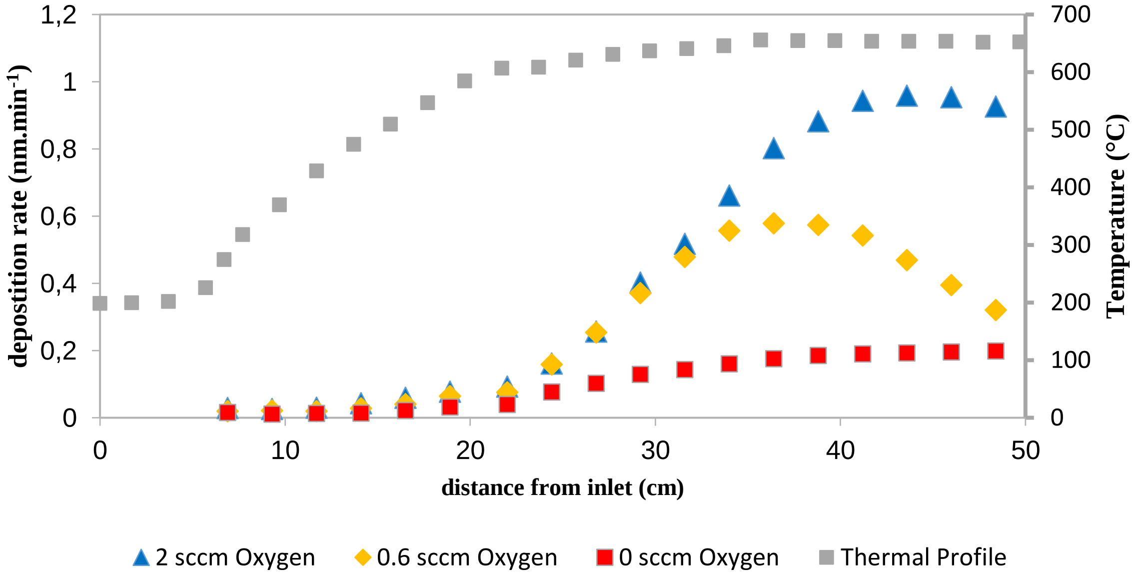

Figure 15: Effect of the O_2 flow rate on the deposition rate (Constant NH_3 flow rate of 20 sccm).

The following observations can be made:

- For all three experiments, the deposition starts at about the same distance from the inlet. It is evident that the deposition starts at about 17 cm from the inlet. That corresponds to a local sample temperature of 530 °C.

- It is evident that an increased oxygen flow rate increases the overall deposition rate of the process.
- For higher oxygen flow rates, the maximum deposition rate shifts towards the end of the reactor. Indeed, it can be observed at a 43.6 cm distance from inlet for an O_2 flow rate of 2 sccm and at a 36.4 cm distance from inlet for an O_2 flow rate of 0.6 sccm. This could be attributed to the lower O_2 concentration in the gas phase, that occur due to the lower flowrate.
- No maximum can be observed for the experiment conducted without an inlet O_2 flow rate.

Then, the effect of the O_2 flow rate on the nitrogen content of the films in presence of constant NH_3 flow was investigated. The nitrogen content below was calculated by the 2 phase BEMA model, as discussed in paragraphs 2.1.2 and 3.2.1. Again, the average molecular fraction of nitrogen in each sample was calculated by averaging the results from the 5 points that were probed for each sample. The results were the following:

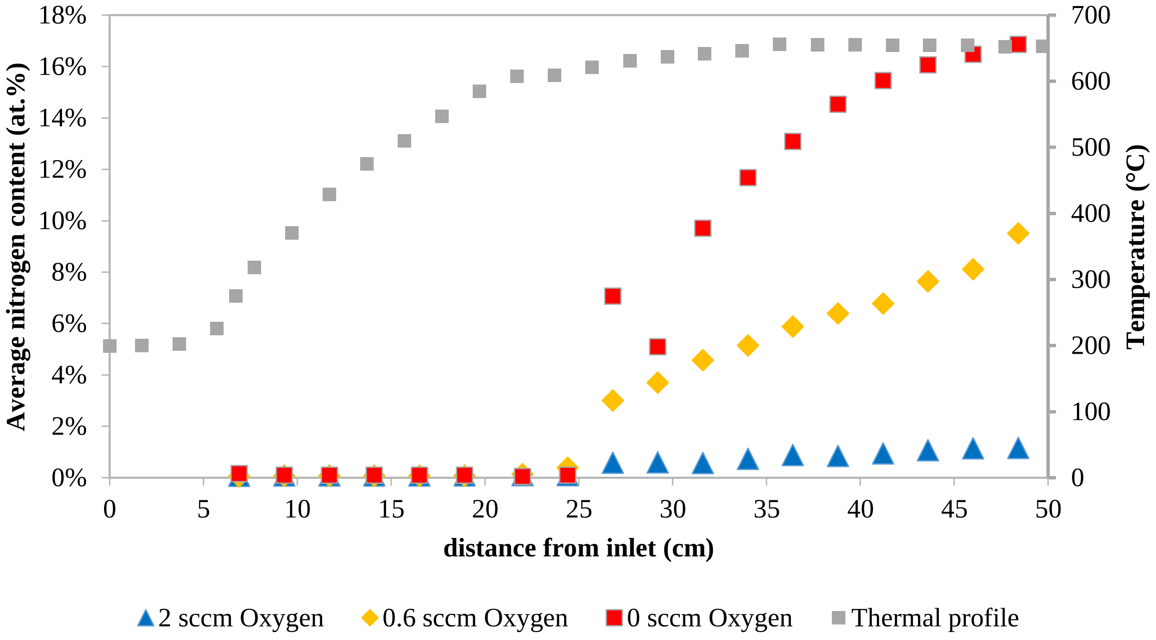

Figure 16:Effect of the O_2 flow rate on the average Nitrogen Content of the films (Constant NH3 flow rate of 20 sccm).

The following observations can be made:

- The nitrogen incorporation inside the films starts at approximately 26.8 cm from the inlet, for all 3 investigated flows of O_2. That translates to a local temperature of 630 °C.

- The higher the O_2 inlet flow rate is, the less nitrogen is incorporated inside the films. The highest nitrogen content was observed for an absence of an O_2 flow.
- The nitrogen incorporation for the film produced under a 2 sccm O_2 flow was minimal. A maximum of 1.2% molar fraction was observed at the end of the reactor.
- The maximum nitrogen content for each experiment can be observed for the final sample of each experiment for all 3 experiments. That could be the effect of a low oxygen concentration in the gas phase towards the exit of the reactor.

Experiments TD7, TD9, TD11 and TD12 were conducted in order to investigate the effect of the O_2 inlet flow rate in the absence of NH_3.

As with the previous case (effect of O_2 flow rate while NH_3 is present), the same strategy was followed for the investigation of the effect of the O_2 flow rate in the absence of ammonia. First, the effect on the deposition rate was investigated. The results are shown in figure 17:

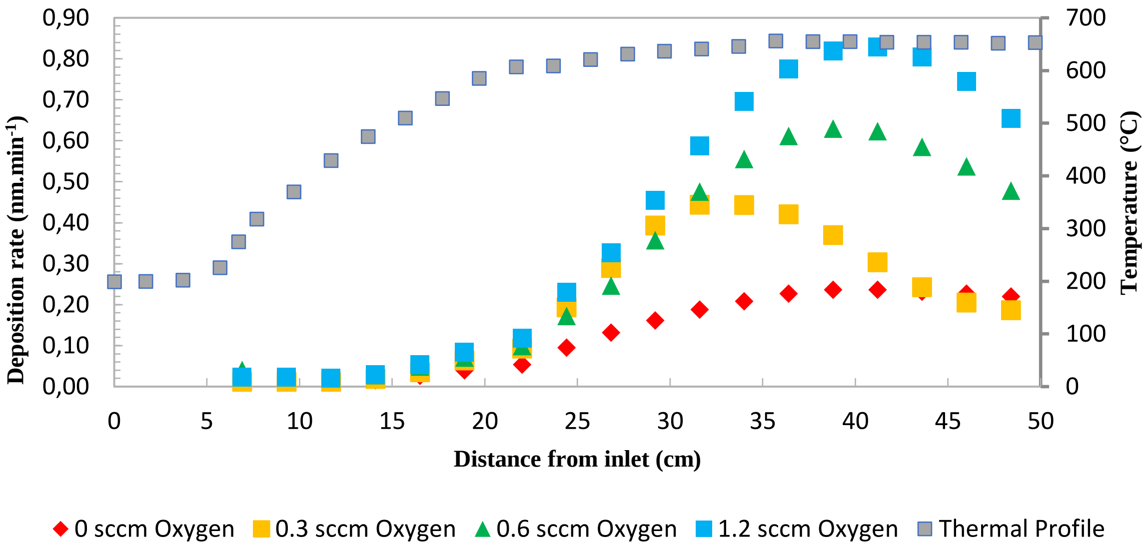

Figure 17 : Effect of the O_2 flow rate on the deposition rate (no NH_3 in the gas phase).

The following observations can be made:

- Similarly, to the experiments where NH_3 was present, the higher the oxygen flow rate, the higher the overall deposition rate of the process.
- The deposition for all experiments starts at 17 cm from the inlet.

- The higher the oxygen flow rate, the deposition rate maximum moves closer to the exhaust of the reactor. This does not appear to be the case for the experiment were 0 sccm of O_2 were used.

Then, the effect of the O_2 flow rate in the on the nitrogen content of the films in the absence of NH_3 was investigated. The nitrogen content below was calculated by the 2 phase BEMA model. The results were the following:

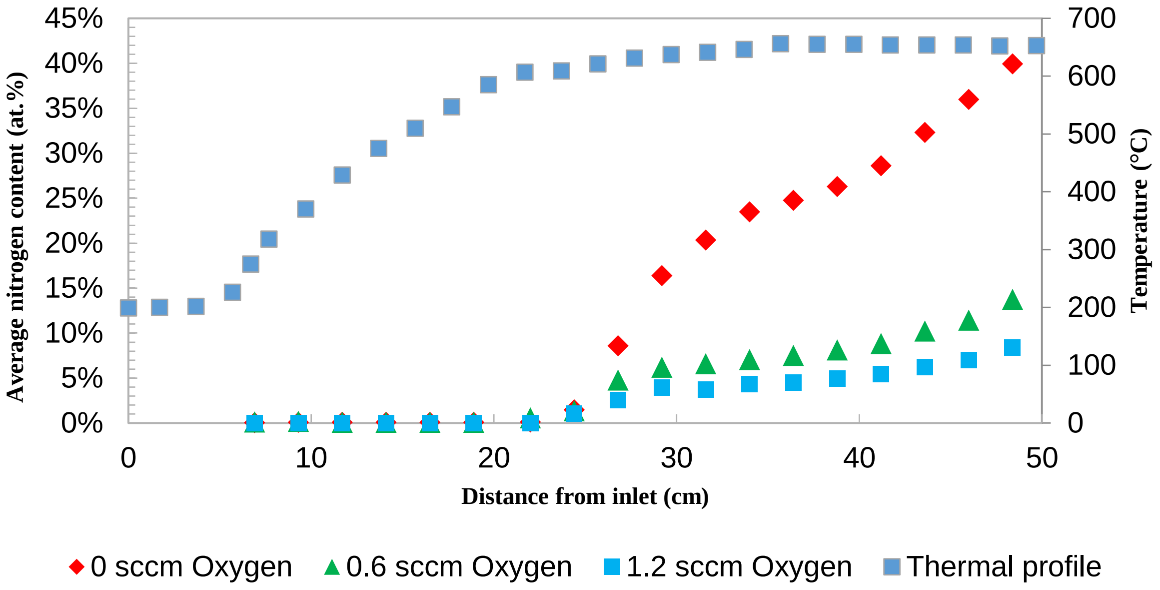

Figure 18: Effect of the O_2 flow rate on the films' Nitrogen content (no NH3 in the gas phase).

The following observations can be made:

- For all experiments, the nitrogen incorporation begins at 22 cm from the inlet. That translates to a local temperature of 610 °C. Additionally, since no ammonia was used, it is concluded that the nitrogen incorporated in the films originates from the precursor.
- The maximum nitrogen content for all experiments is observed at the last sample. That could be the effect of a lower oxygen concentration in the gas phase towards the exit of the reactor, compared to the regions closer to the inlet.
- For the experiment were no oxygen was used (TD9) and therefore the precursor was the main factor for the deposition, the nitrogen content of the film can reach levels up to 40%. However, the 2-phase model provided bad results for an O_2 flow of 0.3 sccm. Therefore, the 40% nitrogen content that was observed here is not considered a reliable result.

- For experiment TD11 (0.3 sccm O_2) IBA results were very different from the results provided by the 2 phase ellipsometric model. For this reason, they are not included in the figure above and will be discussed later.

4.1.2 Effect of the NH_3 Flow rate on the produced films

Experiments TD6, TD7 and TD8 were conducted in order to investigate the effect of the NH_3 inlet flow rate on the resulting films in the presence of O_2. For these experiments, the O_2 inlet flow rate was kept constant at 0.6 sccm.

First, the effect of the NH_3 flow rate on the deposition rate was investigated. The results were the following:

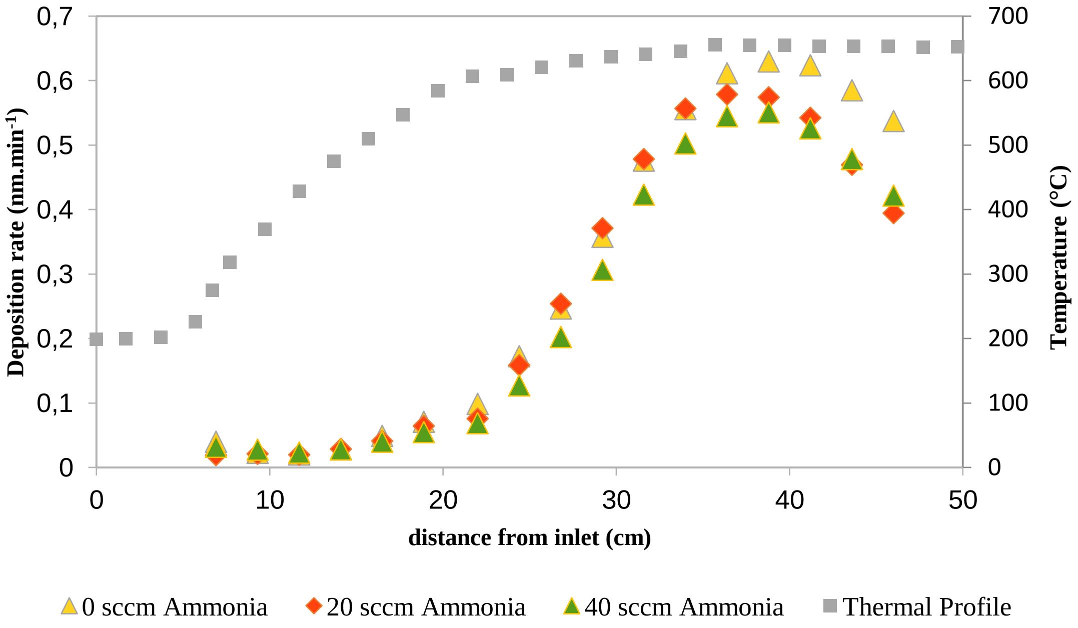

Figure 19: Effect of the NH_3 flow rate on the deposition rate (constant 0.6 sccm O_2 flow rate).

The following observations can be made:

- Similarly to the other experiments, the deposition seems to start at 17 cm from the inlet. That translates to a local temperature of 530 °C.
- The higher the NH_3 flow rate, the lower the overall deposition rate. However, the effect of the ammonia flow rate on the deposition rate does not appear to be that strong.
- A maximum deposition rate has been observed for all experiments. This maximum is observed at a similar distance from the inlet for all studied NH_3 flow rates.

Then, the effect of the NH_3 flow rate on the nitrogen content of the films was investigated. The results were the following:

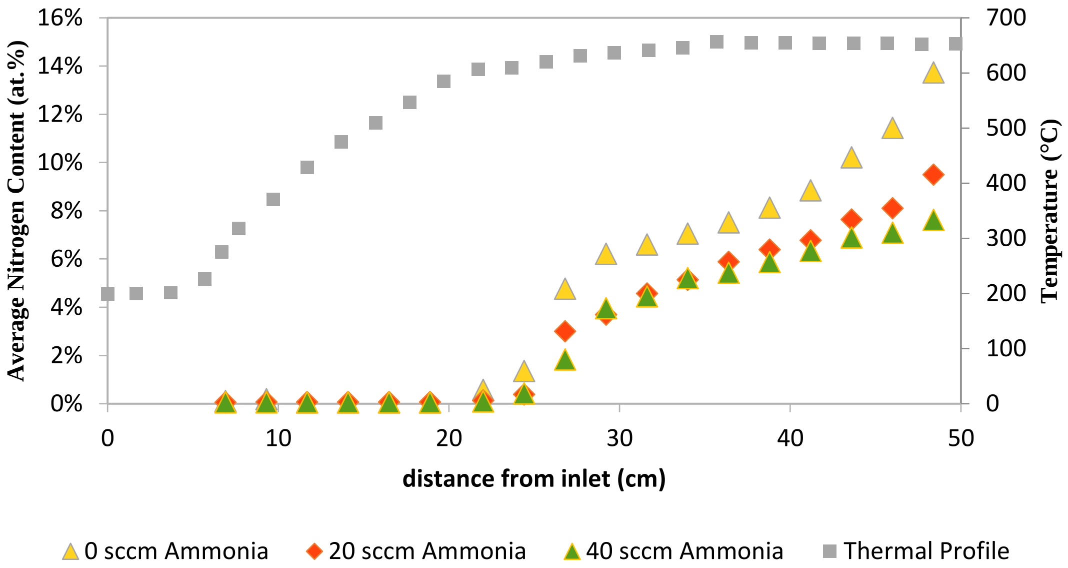

Figure 20: Effect of the NH_3 flow rate on the films' nitrogen content (constant 0.6 sccm O_2 flow rate).

The following observations can be made:

- The higher the NH_3 flow rate, the lower the nitrogen incorporation in the film. This result was not expected and made it clear that the nitrogen incorporation in the film is mostly due to the precursor.
- For all experiments, the nitrogen incorporation begins at 22 cm from the inlet. That translates to a local temperature of 610 °C.
- The maximum nitrogen content for each experiment is observed at the sample closest to the reactor’s exhaust.

4.1.3 Effect of the TDMSA Flow rate on the produced films

Experiments TD3 and TD4 were compared in order to investigate the effect of the TDMSA flow rate on the resulting films. The NH_3 flow rate was kept constant at 20 sccm and the O_2 flow rate was kept constant at 2 sccm.

First, the effect on the deposition rate was investigated. The results were the following:

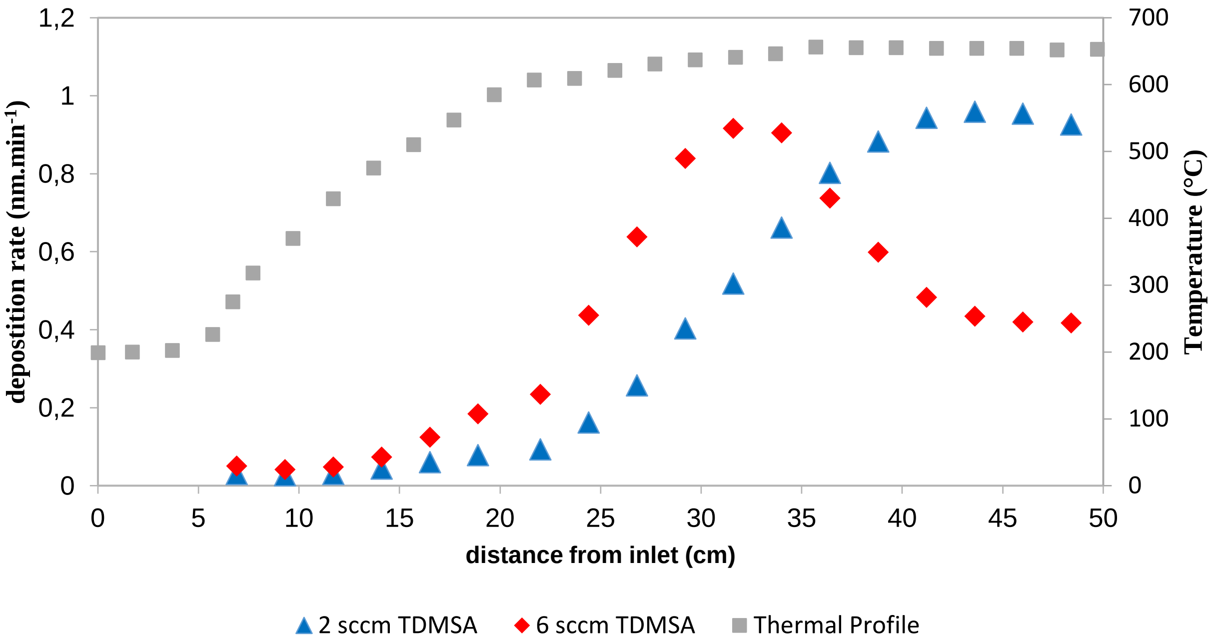

Figure 21: Effect of the TDMSA flow rate on the deposition rate (constant 2 sccm O_2 and 20 sccm NH_3 flow rate).

The following observations can be made:

- The maximum deposition rate observed for both experiments is almost equal. However, it is observed at 32 cm from inlet for a TDMSA flow of 6 sccm and at 42 cm from inlet for a flow of 2 sccm. This could be an indication that the increased concentration of TDMSA leads to a quicker consumption of O_2 in the gas phase. As such, it can be assumed that the oxygen is the limiting reactant.
- For a TDMSA flow rate of 6 sccm, the deposition rate closer to the reactor’s inlet is higher than that of the experiment with a TDMSA flow rate of 2 sccm. However, after the maximum is reached, the deposition rate is lower.

Then the effects on the nitrogen content of the films were investigated. The results were the following:

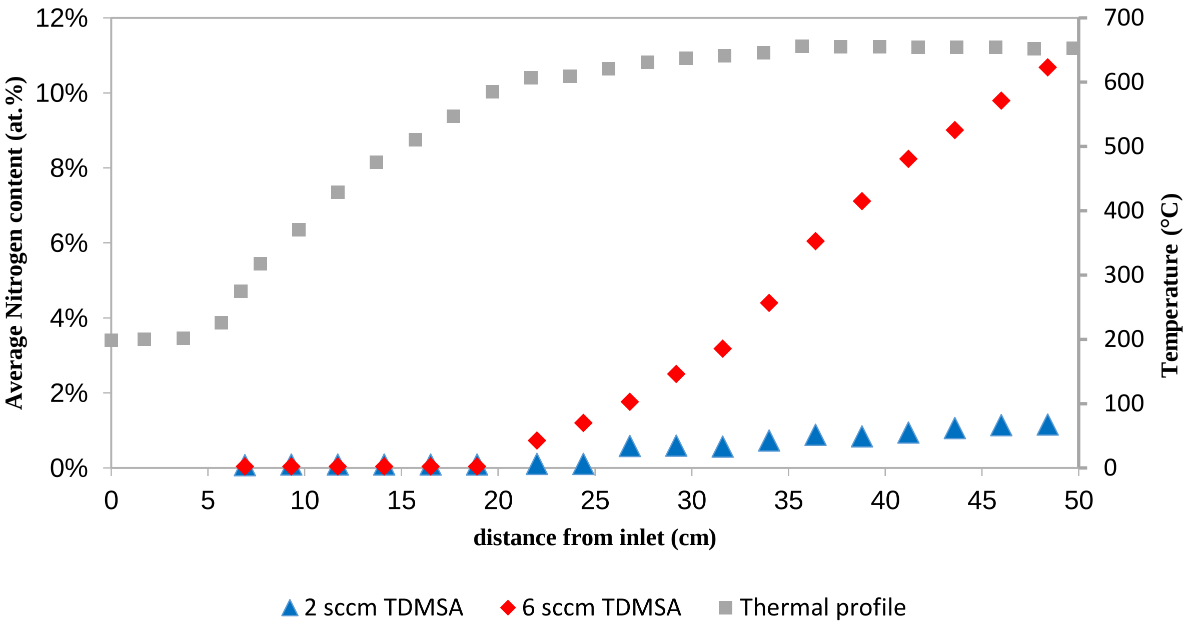

Figure 22: Effect of the TDMSA flow rate on the films' nitrogen content (constant 2 sccm O_2 and 20 sccm NH_3 flow rate.)

The increased amount of TDMSA provides a higher nitrogen incorporation in the films, further confirming that the precursor used is the main source of nitrogen for the films.

4.1.4 Effect of Temperature on the produced films

Experiments TD7 and TD14 were compared in order to investigate the effect of temperature on the resulting films. TD7 was conducted at a set point temperature of 650 °C, while TD14 was conducted at a set point temperature of 625 °C. The inlet composition for both experiments was the same.

The effect on the deposition rate was investigated and the results were the following:

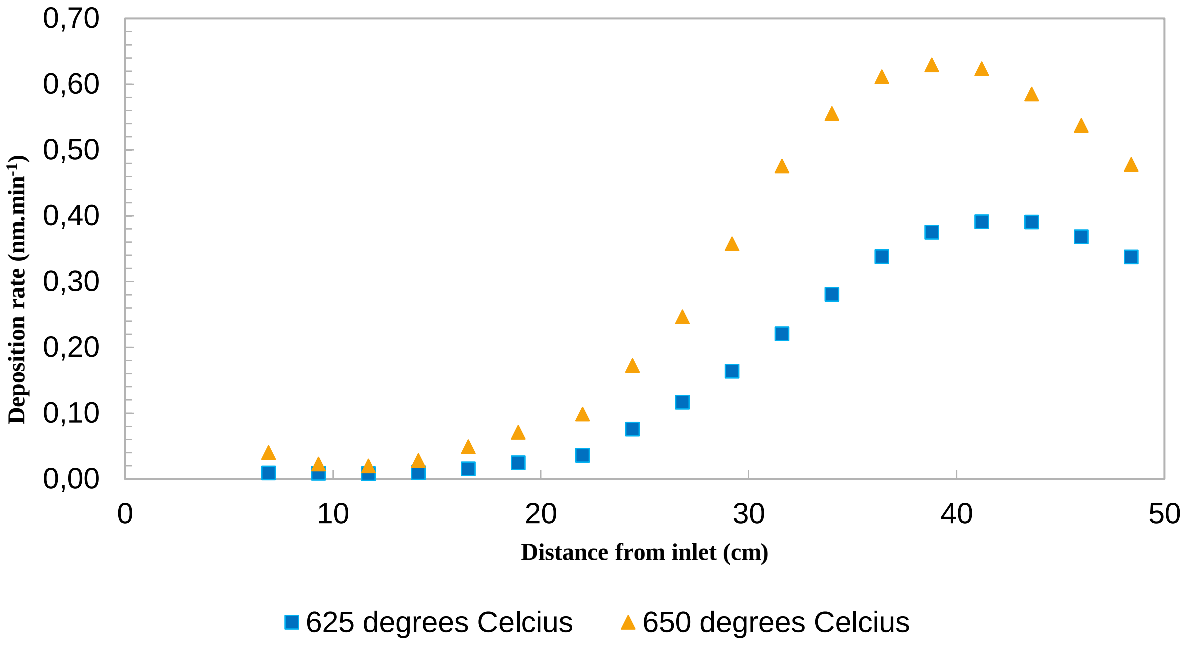

Figure 23: Effect of temperature on the deposition rate (all inlet parameters constant).

The following observations can be made:

- A higher reactor temperature leads to a higher overall deposition rate. That means that the reaction rate becomes faster with the increase in temperature, as expected for endothermic reactions.
- The maximum of the deposition rate is reached closer to the inlet of the reactor for a higher temperature. Again, this is probably because the increase of the temperature results in higher reaction rates per sample, and as such a faster oxygen consumption.

Then, the effect of temperature on the nitrogen content of the films was investigated. The following results were obtained:

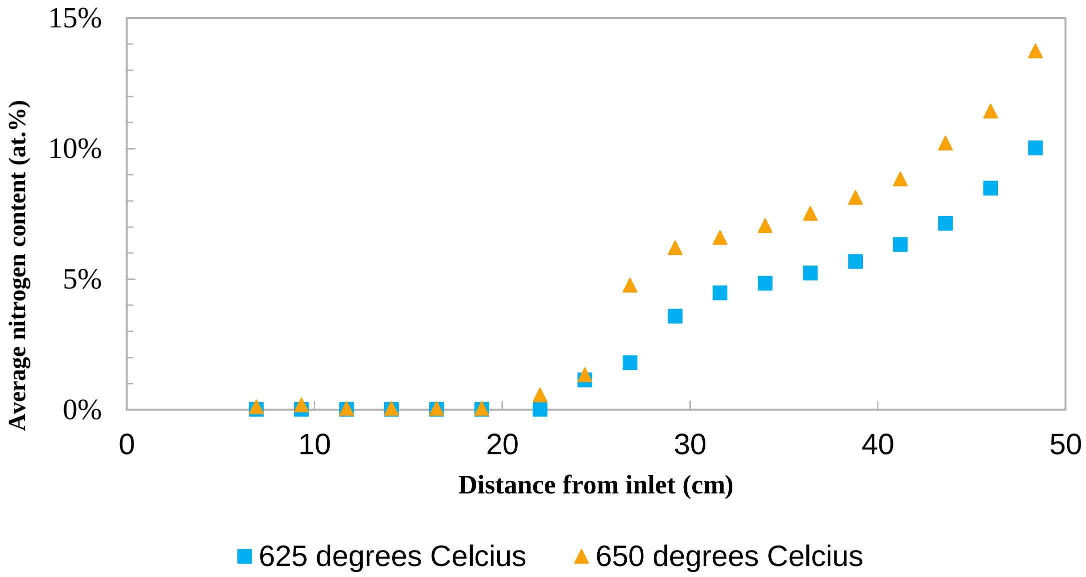

Figure 24: Effect of temperature on the nitrogen content of the films (all inlet conditions constant)

The nitrogen incorporation in the film follows a similar trend and shape. However, the nitrogen incorporation is higher for the experiment that was conducted at 650 °C. This shows that nitrogen deposition is favoured at higher temperatures.

4.2 FTIR

FTIR was utilized in order to obtain information about the several chemical species present in the films. However, in order to clear up and understand better the spectra that were observed, a study of the vibration modes found in SiO_2, Si_3N_4 and SiO_xN_y films was necessary.

4.2.1 Vibration Modes expected in the produced films

The main absorbance peaks expected from SiO_2 films regarding Si-O bonds, as observed by infrared spectroscopy, are the following[9]:

- The rocking mode (Transverse Optical - TO1) at around 455 cm^{-1} [9]
- The bending mode (TO2) at around 805 cm^{-1} [9]
- The symmetric stretching mode (TO3) at around 1080 cm^{-1} [9]
- The asymmetric stretching mode (TO4) at around 1180 cm^{-1} [7]

If the samples are measured under an oblique incidence angle, some longitudinal optical modes can also be observed. This is called the Berreman effect [24]. These modes correspond to the Transverse Optical modes and can be observed in the following wavenumbers[7]:

- LO3 at around 1254 cm^{-1}
- LO4 paired with the TO4 at around 1165 cm^{-1}

These LO modes and their position can provide useful information regarding the structural properties of the network, such as its density [8].

Apart from these peaks, peaks corresponding to hydration in the film's structure may also be observed. Such peaks indicate the presence of hydrogen or hydroxyl groups in the film structure. Specifically, the Si-H stretching mode peak can be found at a band around 2100 cm^{-1} [9], while the wag-rocking vibrations are located at 630-650 cm^{-1}.

Si-OH peaks indicate water contamination and adsorption on the films and can be observed in a wide band around 3600 cm^{-1}, and at 925 cm^{-1} [8]. Of course, peaks corresponding to the H-OH stretching mode can also be observed, at around 3500 cm^{-1} [8].

On the figure below, a typical SiO_2 FTIR spectrum can be observed[8]:

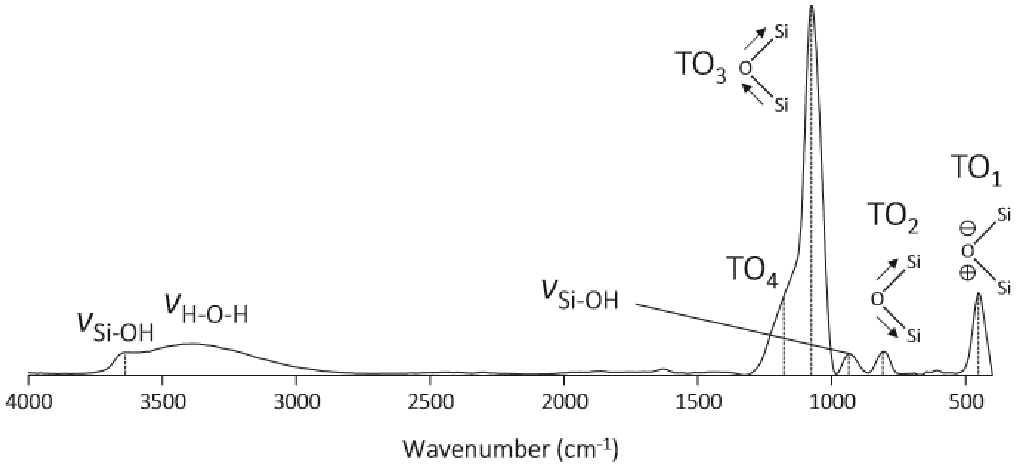

Figure 25:FTIR spectrum of a SiO2 film processed at a temperature of 400°C [8].

The TO3 vibration mode's position depends on the film's thickness, porosity[29], strain, stress, and oxygen content. The TO2 and TO1 modes' position appears to be unaffected by the above parameters [7].

The main absorbance peaks expected in Si_3N_4 films from an infrared spectroscopy regarding Si-N bonds are the following[11]:

- The symmetric stretching mode around 490 cm^{-1}
- The asymmetric stretching mode around 850 cm^{-1}
- A third mode responding to stretching vibrations of the locally distorted configurations at 790 cm^{-1}

As in the case of silicon oxides, the presence of impurities in the silicon nitride films can also be observed in their FTIR spectra.

The H-OH band can be observed, as in the spectra of silicon oxides, and appear as a band around 3300-3500 cm^{-1}. [10]

However, two more peaks that correspond to the N-H bond are also observed in this region. The first one relates to the N-H stretching bond near 3320 cm^{-1}. This band however appears to have a “tail”, which is likely to be caused by hydrogen bonds between the hydrogen atoms of the N-H bond and lone pair electrons on nearby nitrogen atoms[30]. The notation given for this specific type of vibration is N-H---N and it can be found at around 3300 cm^{-1}.

The Si-H bonds that appear in silicon oxides can also be observed at around 2100 cm^{-1}. However, the peak found at around 630 cm^{-1} is hidden by the much more intense Si-N band [31]. All of the aforementioned peak positions depend on the process and the conditions utilized for film production.

On the figure below, a typical Si_3N_4 FTIR spectrum can be observed [10]. The absence of a Si-O-Si peak around 1100 cm^{-1} is clear.

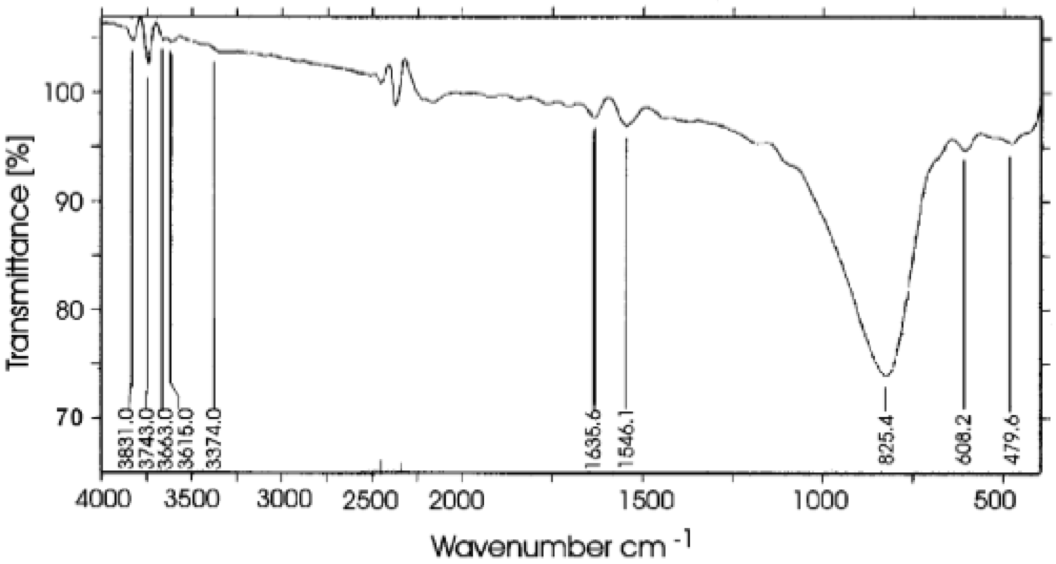

Figure 26: FTIR Spectrum of a PECVD Silicon Nitride film [10].

The precursor, TDMSA, used for the experiments of the present thesis, contains a respectable amount of carbon. For this reason, the Si-CH_3 peak around 1260 cm^{-1}, the =CH_2 peak around 3050 cm^{-1} and the –CH_x peaks around 2960-2800 cm^{-1} will be also taken into account [15].

4.2.2 Areas of focus in FTIR study

The two main areas of interest chosen for the characterization of silicon oxynitride films are the following: A fingerprint region observed between 650 and 1300 cm^{-1}, that contains the majority of the information regarding the main lattice of the film. The second area is the hydrated region found between 2700 and 3600 cm^{-1}, which contains the majority of the hydrogen related absorptions.

In Figure 27, a silicon oxynitride spectrum acquired of a sample containing 7.5 at.% nitrogen produced at 650°C (TD7 experiment) can be observed:

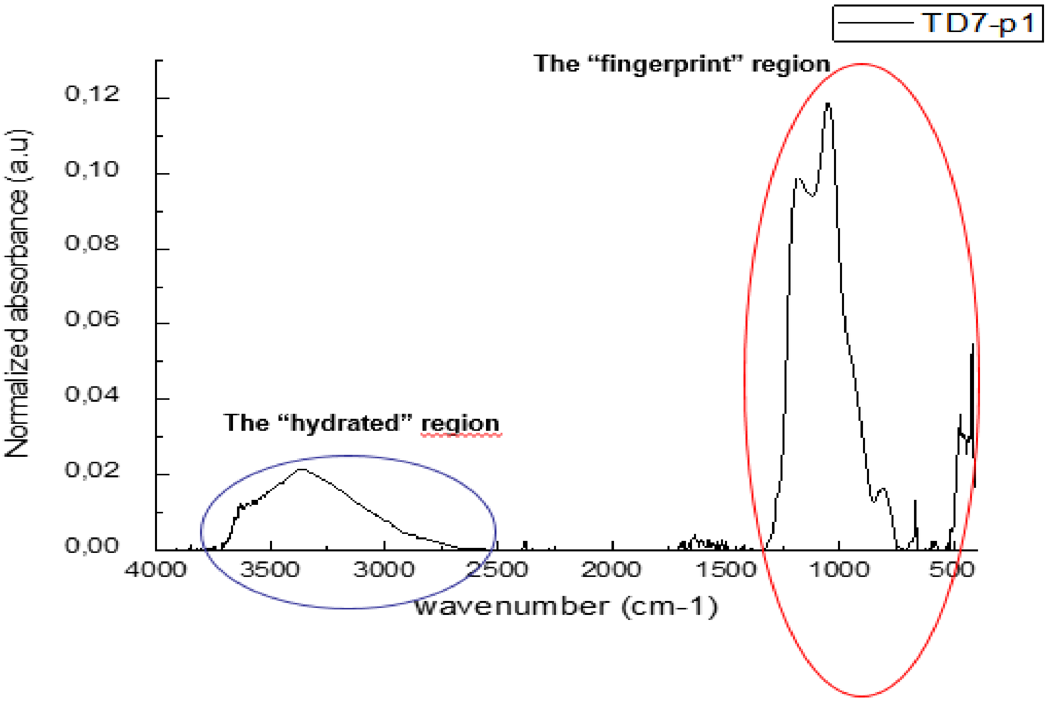

Figure 27: Typical FTIR spectrum acquired from the TD7-P1 sample.

Firstly, the hydrated area around 3600 – 2700 cm^{-1}, which indicates the presence of hydrogen and hydroxyl bonds in the film, is denoted in blue in Figure 27. In this specific area, the following modes can be observed[12], [13]:

- The Si-OH stretching mode, observed around 3600 cm^{-1}
- The H-OH stretching mode, observed around 3500 cm^{-1}
- The N-H stretching mode, observed around 3400 cm^{-1}
- The N-H--N stretching mode, observed around 3350 cm^{-1}
- The =CH_2 stretching mode, observed around 3055 cm^{-1} [15]

- The –CH_x stretching mode, observed between 2960-2800 cm^{-1} [15]

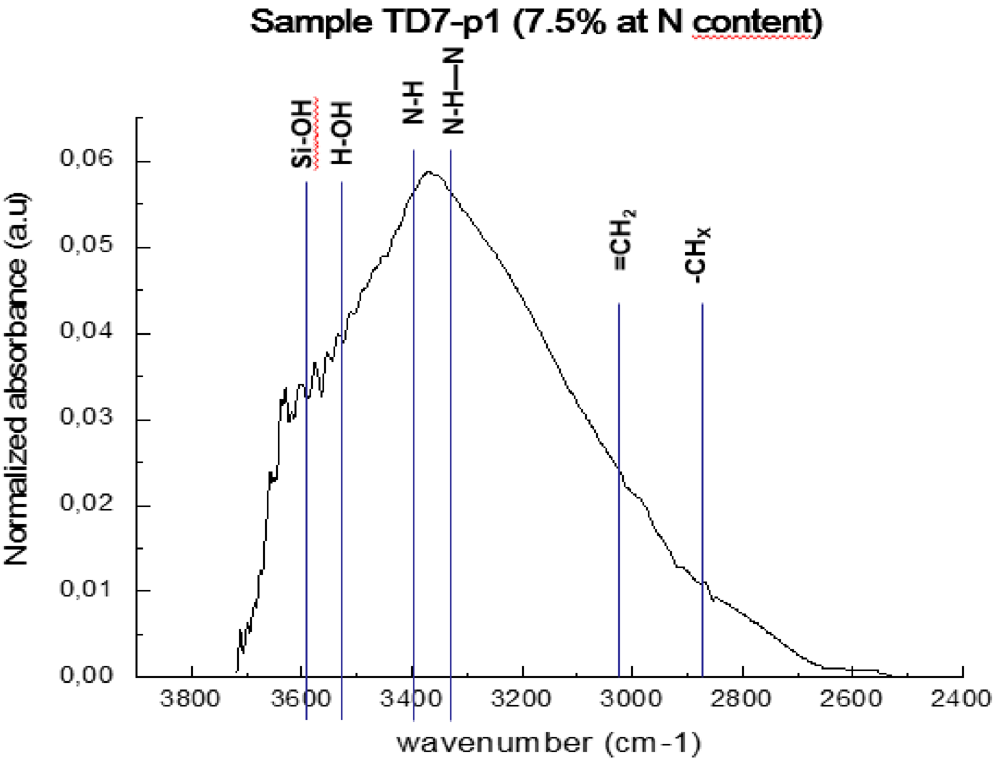

Figure 28: Peaks found in the hydrated area.

In Figure 29, a deconvolution of the "hydrated area" is shown. As mentioned before in chapter 3.2.2, Gaussian curves have been used for the deconvolution of the spectra.

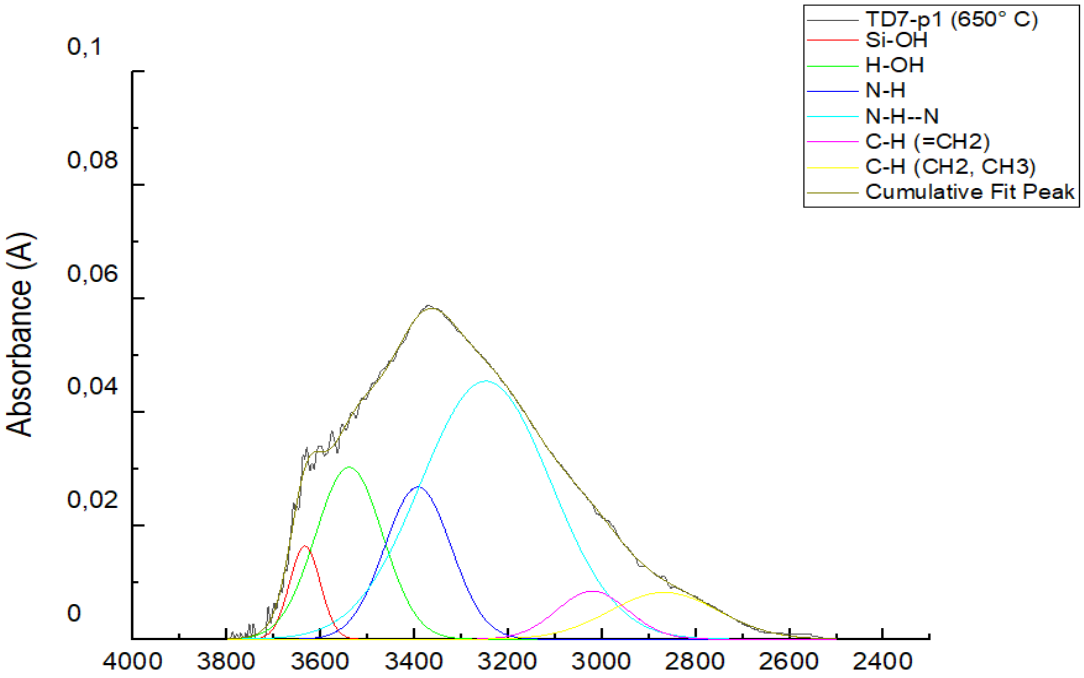

Figure 29: Example of the deconvolution of the "hydrated region".

The second area of interest, the "fingerprint region" can be found around 1300 – 650 cm^{-1}. This area gives precious information regarding the structure of the lattice. In this area, peaks related to Si-N, Si-O, Si-C can be observed. Again, due to the complexity of this area because of the overlapping absorptions, deconvolution is required to correctly identify the exact properties of the peaks.

Specifically, the peaks that appear in this area are the following:

- The Si-$(CH_3)_X$ stretching bond observed around 1270 cm^{-1} [32]
- The Si-O-Si TO4 mode observed at 1160 cm^{-1} [12], [13]
- The Si-O-Si TO3 mode observed at 1040 cm^{-1} [12], [13]
- A possible Si-CH_2-Si stretching mode around 1020 cm^{-1}. [33]
- A Si-OH stretching mode around 925 cm^{-1} , as mentioned in chapter 3 [8]
- A Si-N stretching mode, observed around 940 cm^{-1} [12], [13]
- A Si-O bending mode, observed around 820 cm^{-1} [12], [13]
- A possible Si-C stretching mode, observed around 800 cm^{-1} [34], [35]
- The Si-N symmetric stretching at 490 cm^{-1} [11]
- The Si-O rocking mode at 450 cm^{-1} [12], [13]

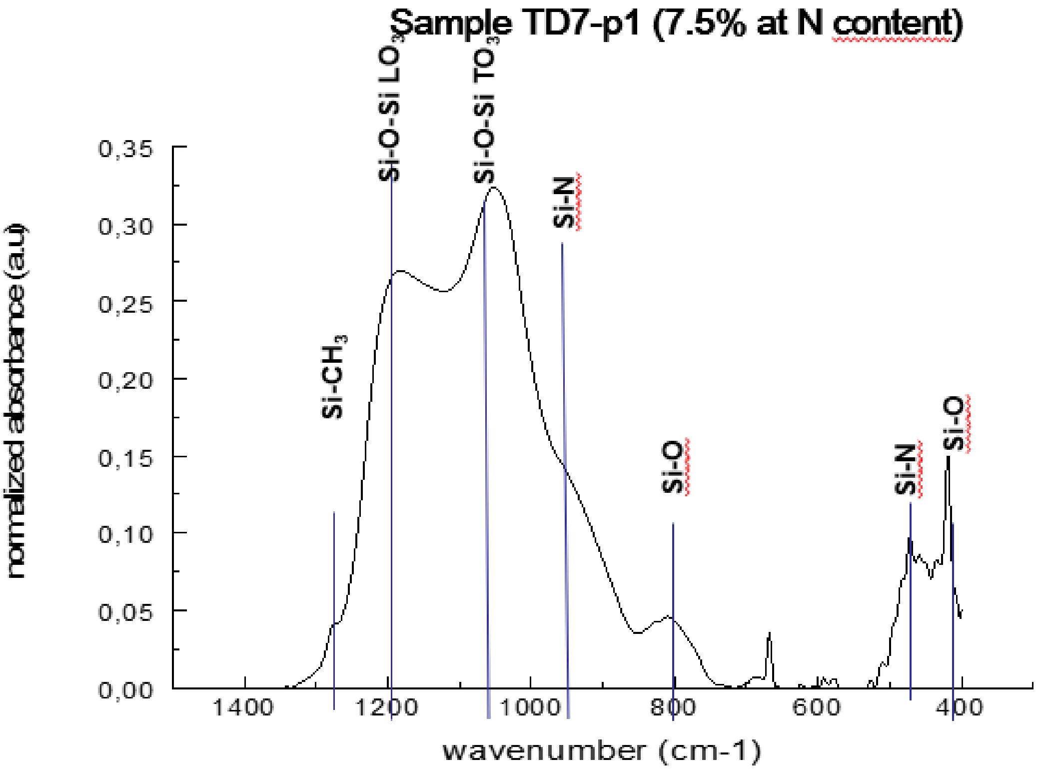

Figure 30: Peaks found in the fingerprint region.

Below, a deconvolution of the “fingerprint region” using Gaussian curves is shown.

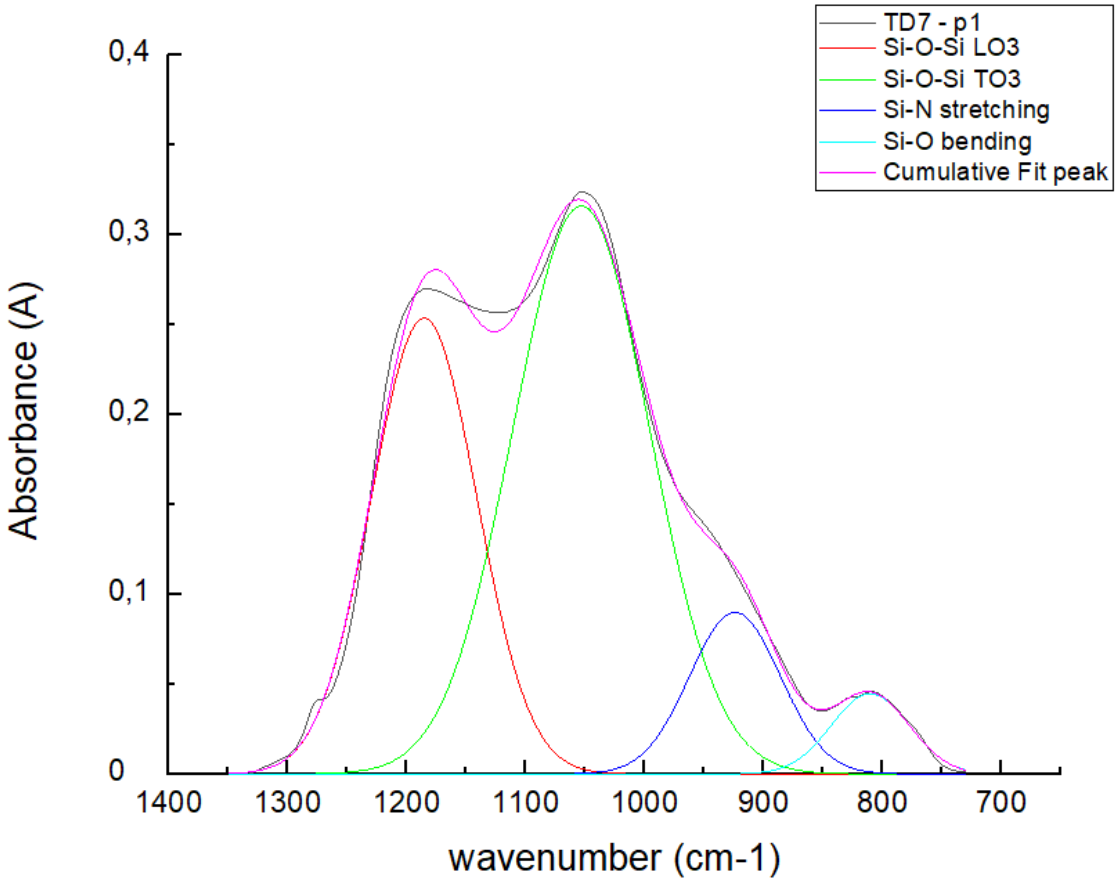

Figure 31: Example of the deconvolution of the "fingerprint region".

The main peaks whose evolution was tracked across all experiments were the Si-N stretching mode, the Si-CH_3 stretching mode and the Si-O-Si symmetric stretching mode (TO_3) peak. The Si-CH_3 peak is identified by the visual observation of the shoulder around 1270 cm^{-1} and not through deconvolution. The other two peaks (Si-O-Si TO_3 and Si-N stretching mode), were tracked through the results obtained via the deconvolution. For these two peaks, the position and intensity were tracked for every sample. This was done in order to correlate the intensity and position of these peaks with the nitrogen content of the films, as calculated by ellipsometry.

Another thing that has to be taken into account, is the deconvoluted peak around 800 cm^{-1}. For the sample studied in Fig.31, this peak has been attributed to the Si-O bending vibration mode. However, several silicon related absorptions take place in that wavenumber area. It is possible that the peak at 800 cm^{-1} is a different Si-N vibration mode, or even a Si-C stretching mode vibration. To correctly attribute the 800 cm^{-1} absorption to the respective bonds, X-ray photoelectron spectroscopy (XPS) analysis will be utilized. The acquisition of high-resolution spectra, coupled with the deconvolution of the N1s and C1s spectra, will give information on the environment of these elements. Through this analysis, some authors [36] have managed to discern between the amount of Si-O, Si-C and Si-N bonds.

It should be noted that the majority of the aforementioned peaks are observed across the majority of the experiments. The existence of the many types of methyl groups inside the films is possibly an indication of a $SiO_xN_y:CH_3$ film.

4.2.3 Tracking of the Si-O-Si TO_3, Si-N and Si-CH_3 stretching modes

Through deconvolution, the tracking of the Si-O-Si TO_3 and Si-N peaks has been made possible across experiments. For the Si-CH_3 peak, only the peak position was tracked without using deconvolution – just by the visual observation of the spectra. The results were the following:

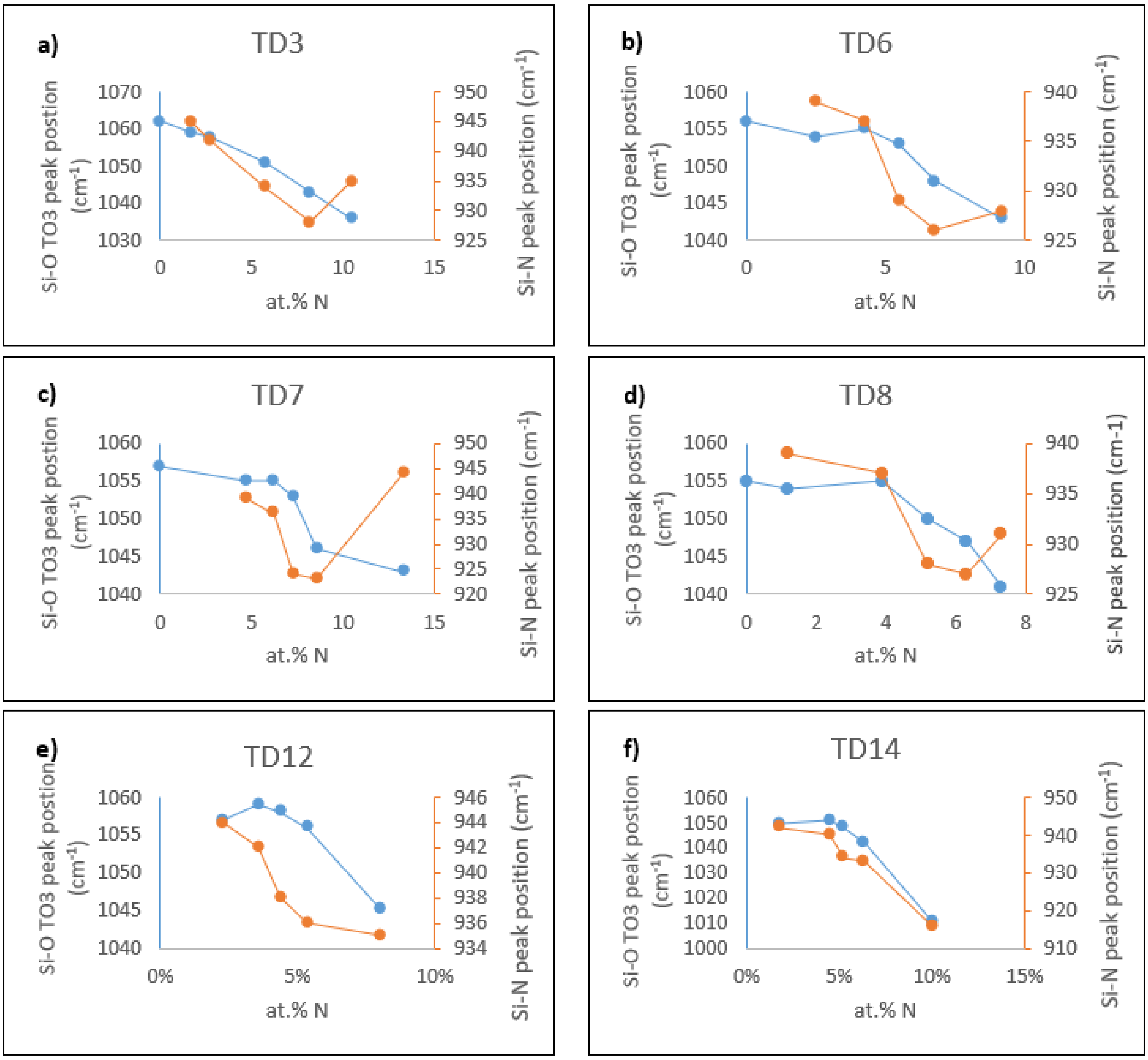

Figure 32: Si-O-Si TO3 and Si-N stretching mode peak positions vs atomic nitrogen content across experiments

It appears that for each experiment, as we are moving closer towards the exhaust of the reactor and the nitrogen incorporation inside the film is increasing, both the Si-O symmetric stretching mode and the Si-N stretching mode peak shift towards lower wavenumbers. This is probably caused by the increase in the nitrogen content of the films. Additionally, a break in the slope of the Si-O-Si symmetric stretching mode is observed globally once the nitrogen at.% exceeds approximately 5 at.%.

Several authors have noted a shift of both peaks towards higher wavenumbers after the annealing of the samples, attributed to the re-organization of the network[37], [38]. Based on this idea, the shift of the Si-N peaks of the final samples of several experiments like TD3, TD6, TD7, TD8 (Fig. 32a, 32b, 32c, 32d) could hint towards a more organized network.

However, no explanation has been given for the overall shift of the peaks towards lower wavenumbers. It is assumed that it is an effect of the increasing nitrogen incorporation in the network [39], [40].

Then, the intensity of the absorbance of the Si-O-Si TO$_3$ and Si-N stretching vibrations based on the nitrogen content of the films was investigated, the results were the following:

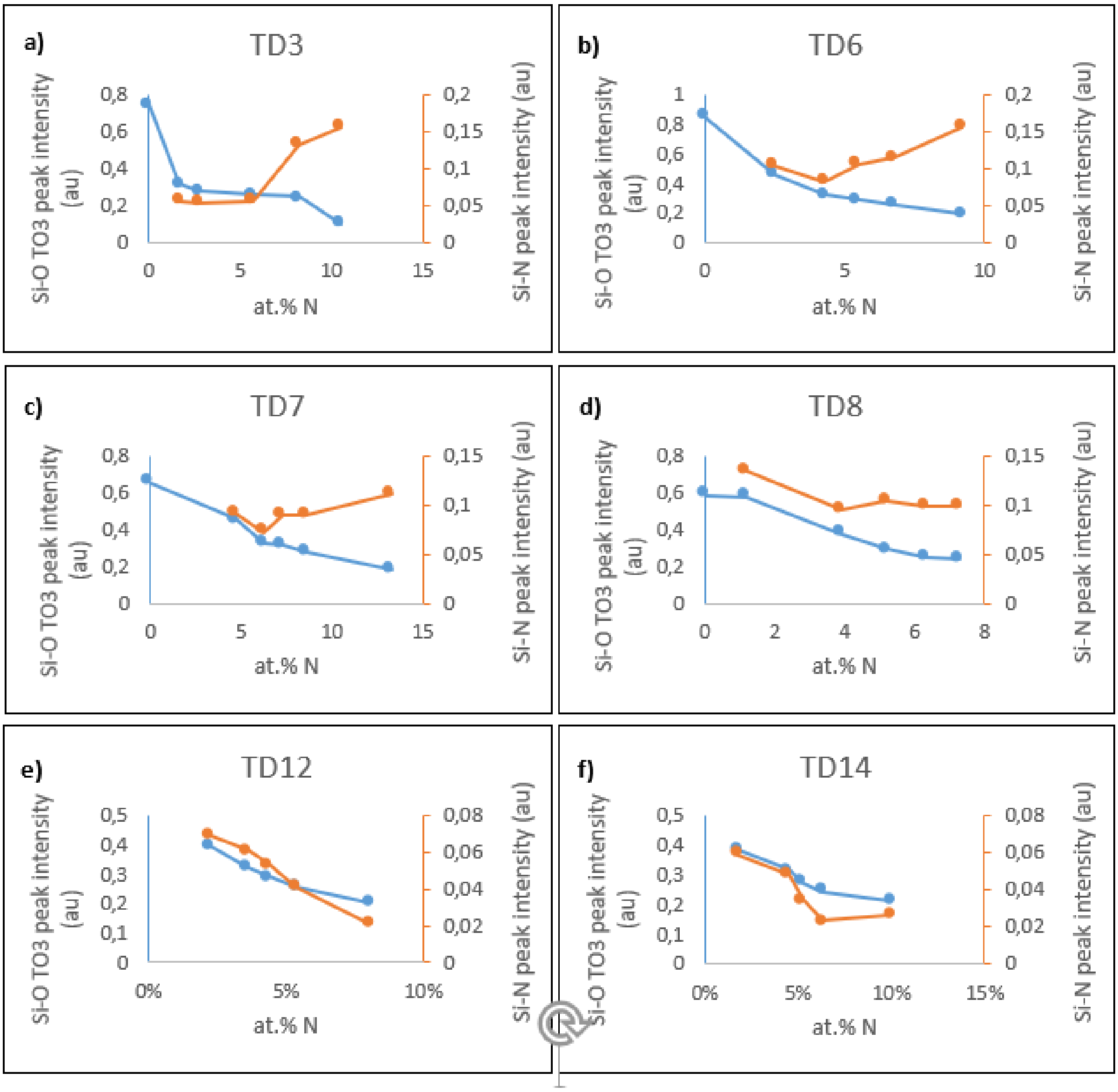

Figure 33: Si-O-Si TO3 and Si-N stretching mode intensities vs atomic nitrogen content across experiments

For experiments TD3, TD6, TD7 (Fig. 33a, 33b, 33c respectively), an increase in the absorbance intensity of the Si-N stretching mode peak is observed, as well as a decrease in the absorbance intensity of the Si-O-Si stretching mode peak. Moreoever, a break in the slope of the Si-N stretching mode intensity is globally observed to happen after approximately 4-5 at.% of nitrogen. Additionally, if Beer's law is taken into account and the absorptivity remains constant, then this could translate to the increase of the Si-N bonds concentration and a decrease of the Si-O-Si bonds inside the film. However, this trend is not observed in films produced from the other three experiments TD8 ,TD12, TD14 (Fig. 33d, 33e, 33f respectively). Instead, both the intensities of the Si-O-Si and Si-N stretching modes decrease. If Beer's law is still taken into account, then this could correspond to either a decrease in the concentration of the species – something which is not possible based on the ellipsometry and IBA results - or due to a change in the absorptivity of the material. Some other factors that could weigh-in on this unintuitive trend could be possible computational errors in the deconvolution of the spectra, or deviations in the thickness values (as calculated by ellipsometry) used for the normalization of the FTIR spectra.

Afterwards, the Si-CH_3 stretching mode peak position correlation with the nitrogen content of the films was investigated. As mentioned above, this peak was tracked by visually observing the shoulder that appears around 1270 cm^{-1}. The results were the following:

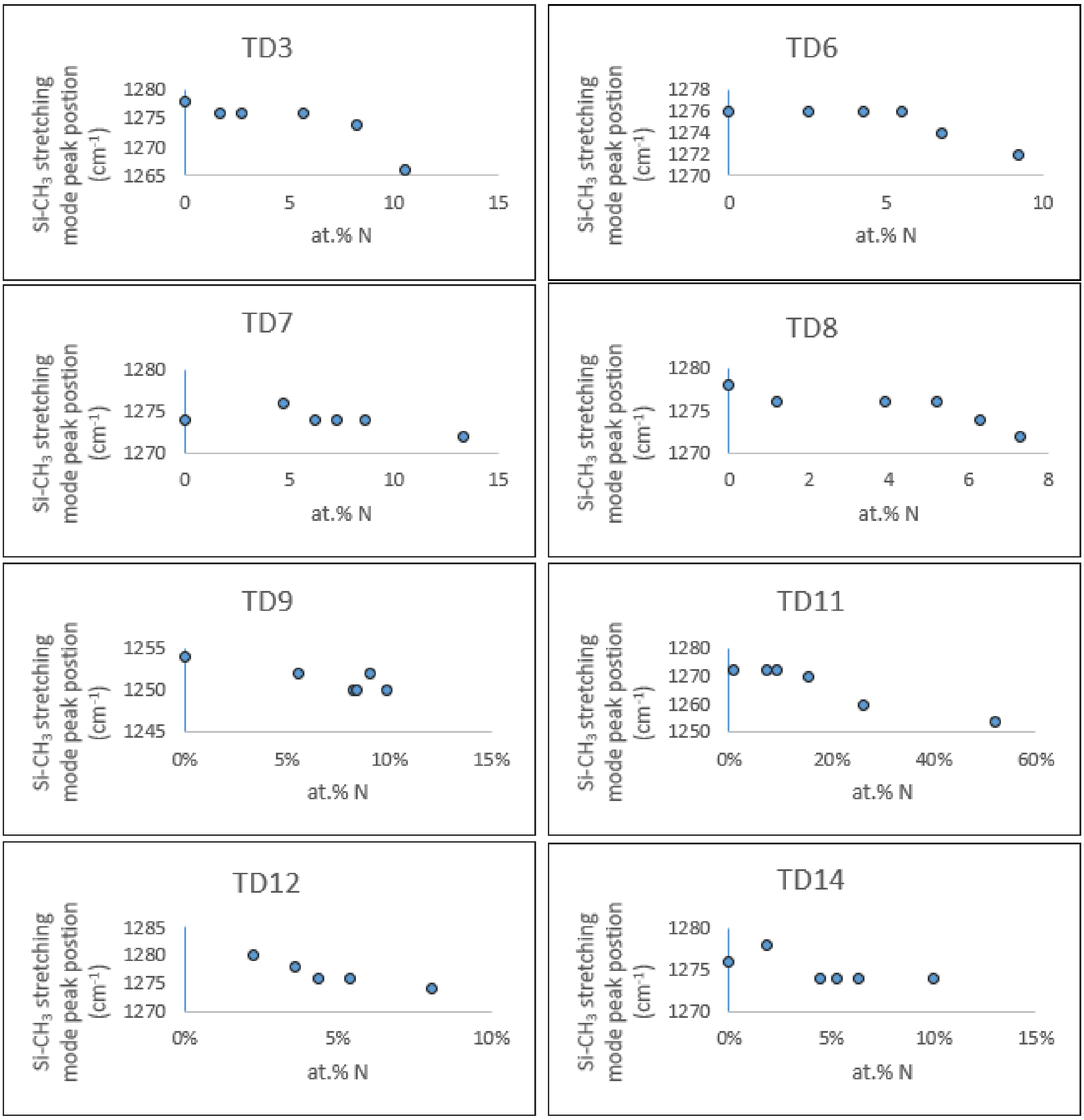

Figure 34: Si-CH_3 stretching mode position vs atomic nitrogen content across experiments.

A generic trend can be observed here. As the nitrogen content of the films increases, the position of the Si-CH_3 stretching mode peak shifts towards lower wavenumbers.

4.2.4 Tracking of possible Si-H peaks

For the investigation of the existence of Si-H bonds inside the films and for its correlation with the experimental parameters, the absorptions occurring in the wavenumber range of 2300-2000 cm^{-1} must be observed. In other CVD methods and especially PECVD, the produced silicon oxynitride films may contain a high concentration of hydrogen, especially in the form of Si-H bonds. In their publication, Varanasi et. al [41], correlate the content Si-H bonds with the passivation properties of the film in physiological conditions. Specifically, the increase of the Si-H bond content hinders the passivation properties of the films, causing them to be partially soluble in certain conditions. The authors also mention that a film with increased Si-H concentration and low nitrogen content is easily soluble. In their publication, the Si-H peak position ranged from 2252-2270 cm^{-1}. Other authors, have positioned the Si-H stretching mode in the band ranging from 2000-2200 cm^{-1} [34] and more specifically around 2120 cm^{-1} [42]. Peter et. al [42] have attributed the peak found around 2200 cm^{-1} to a C=N stretching mode.

For the p1 sample of each experiment (as shown in Fig.14), the FTIR spectra acquired were isolated in the 2300-2000 cm^{-1} wavenumber range, searching for possible absorptions. The results were the following:

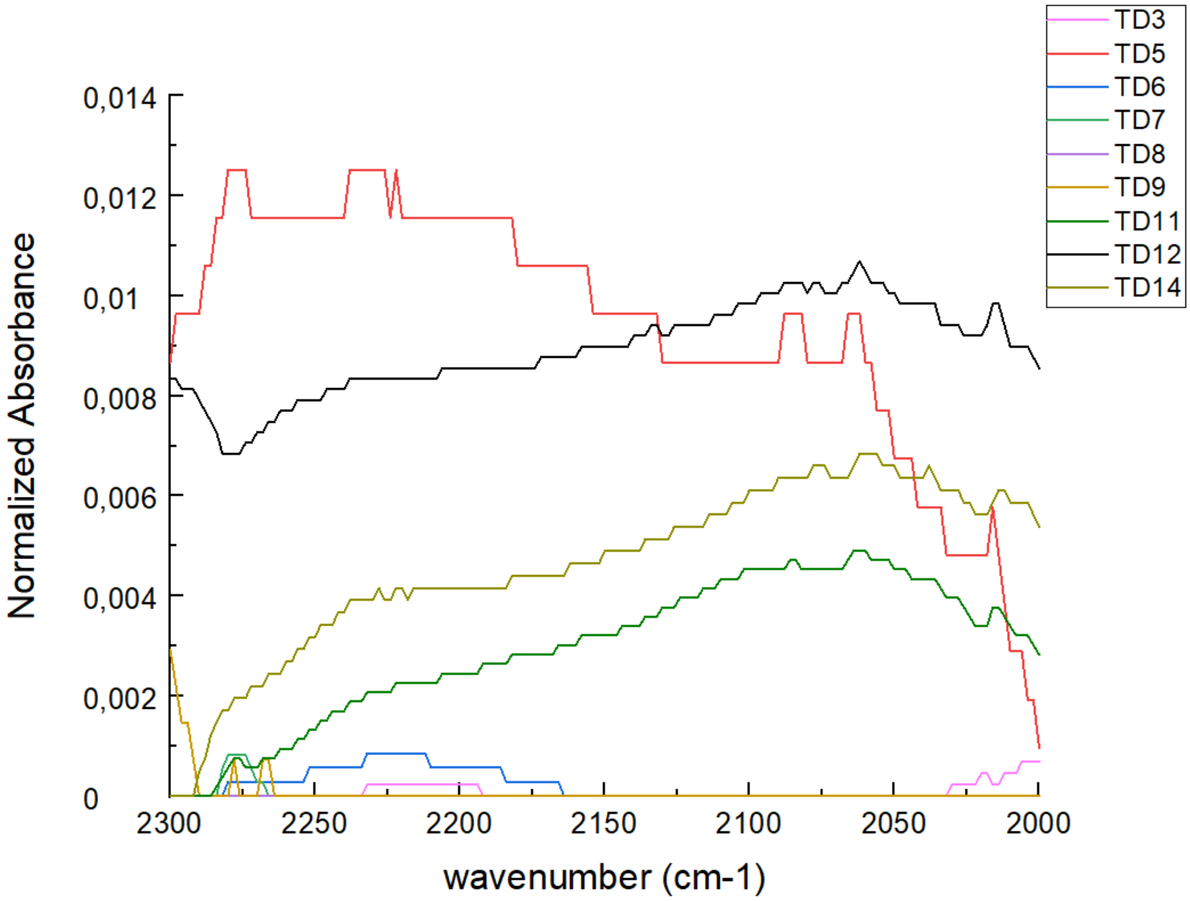

Figure 35: The 2300-2000 cm^{-1} wavenumber range for the experiment series.

Before commenting the figure above, it should be noted that the absorbance intensities measured for this range for all the experiments are quite low. However, the following observations can be made:

1. The films corresponding to experiments TD3, TD6, TD7, TD8 and TD9 show the lower absorbance levels for the whole wavenumber range. The absorbance intensity is almost zero, therefore it could be argued that no Si-H bonds are present in the films (any comment on how this correlates with the gas phase composition?).
2. The films corresponding to experiments TD11, TD12 and TD14 all follow a similar pattern. The highest absorbance in this wavenumber range for all these films can be observed at around 2080 cm^{-1}. Therefore, the presence of Si-H species in these films can be supported. This similar behaviour could be attributed to the fact that all three experiments took place under an ammonia free gas phase, with the oxygen flow and temperature being the only variables.

3. The film corresponding to experiment TD5 shows the most unique behaviour between the films studied. It shows an absorbance maximum around 2230 cm^{-1}. This could be attributed to the C=N stretching mode. The absorbance observed around 2100 cm^{-1} could be attributed to the Si-H stretching mode. For the TD5 experiment, no O_2 was used the gas phase. It was the only experiment for which only the precursor and NH_3 were present in the reactor inlet. This could be the reason for this unique behaviour.

To sum up, although the absorbances detected for the whole range of experiments in the 2300-2000 cm^{-1} wavenumber range were low, certain similarities could be observed for some experiment groups. This appears to have a connection to the experimental parameters used, and more specifically, to the gas phase composition.

It should also be noted, however, that for the TD6, TD7 and TD8 experiments, where absorbance was not detected, the IBA results, which will be presented in more in the following chapter, show a hydrogen content similar to that of the TD11, TD12 and TD14 experiments. This could mean that for the TD6, TD7 and TD8 experiments, hydrogen is mostly found in the Si-OH, N-H and H-OH species present in the films, and not Si-H.

4.2.5 Effect of the O_2 flow rate on the overall character of the films

Another trend was observed, while visually comparing acquired spectra from the whole range of experiments. When higher flow rates of oxygen are used in the gas phase composition, the spectra acquired are similar to silicon oxide spectra – they have a SiO_2 character. When lower flow rates of oxygen are used in the reactor inlet, the spectra acquired are similar to silicon nitride spectra – they have a Si_3N_4 character. The evident LO3-TO3 Si-O-Si peak pair found in silicon oxide films observed due to the Berreman effect [24], was considered a major indicator of the films' character. This trend can of course be linked to the nitrogen content and its correlation to the inlet oxygen flow rate, as discussed in section 4.1.1. This change of character of the films is clearer when comparing the spectra of the samples that are placed near the exhaust of the reactor for different experiments, or when comparing the spectra that were acquired for samples of the same experiment across the reactor. In the figures below, both cases are displayed.

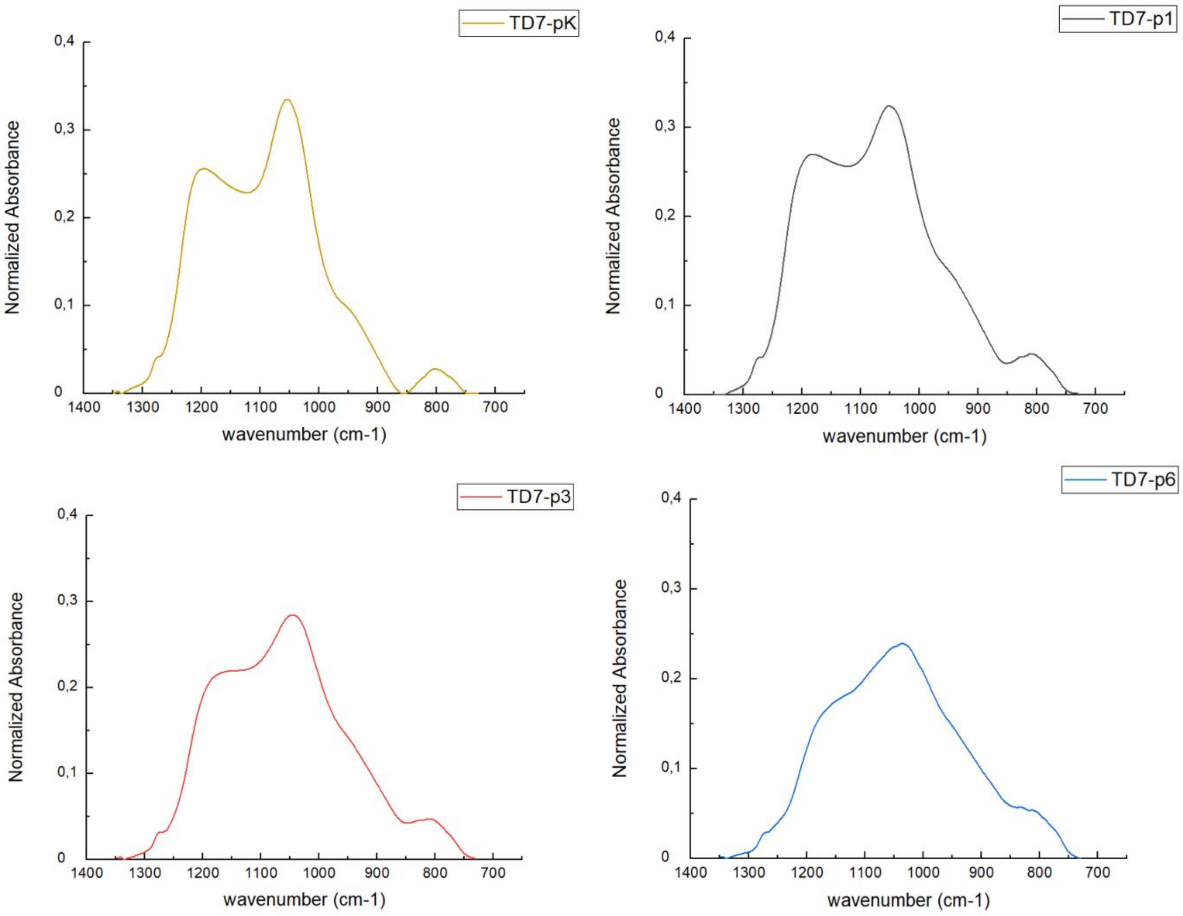

Figure 36: Evolution of the "fingerprint" area for the TD7 experiment.

It is obvious that, while comparing the spectra of the samples from different positions inside the reactor (from TD7-pK to TD7-p6), their character changes. In the TD7-pK sample, the one closest to the reactor inlet between the four, has a clear oxide character. The LO3-TO3 pair is clearly evident, with the two peaks distinctively separated, one around 1200 cm^{-1} and the one around 1050 cm^{-1}, while the Si-N stretching mode, observed as the shoulder around 940 cm^{-1}, has a much lower intensity than that of the Si-O modes. As we move towards the exhaust of the reactor, the Si-O-Si LO3-TO3 pair becomes less evident, with the two peaks slowly merging into almost one (TD7-p6). The shoulder of the Si-N stretching mode becomes broader, more evident and its intensity increases. In the TD7-p6 sample – the one closest to the exhaust of the reactor, the LO3-TO3 Si-O-Si pair is still evident, but much less so. The film still has a dominant SiO_2 character, but the inclusion of nitrogen in the film is obvious. As it has been established in chapter 4.1, oxygen is the main promoter for film formation at the temperatures studied. That means that it reacts easily in the gas phase and readily leads to SiO_2 deposition.

This change is character can be attributed, therefore, to the consumption of oxygen in the gas phase, which leads to lower oxygen concentrations towards the exhaust of the reactor, and as such, a relatively lower SiO_2 deposition compared to Si_3N_4.

Below, the evolution between the final reactor samples for each experiment that was conducted without the use of ammonia in the gas phase can be observed. For the TD12 experiment, 1.2 sccm of O_2 were used in the gas phase. For the TD7 and TD11 experiments, 0.6 and 0.3 sccm of O_2 were used, respectively. For the TD9 experiment, no O_2 was used.

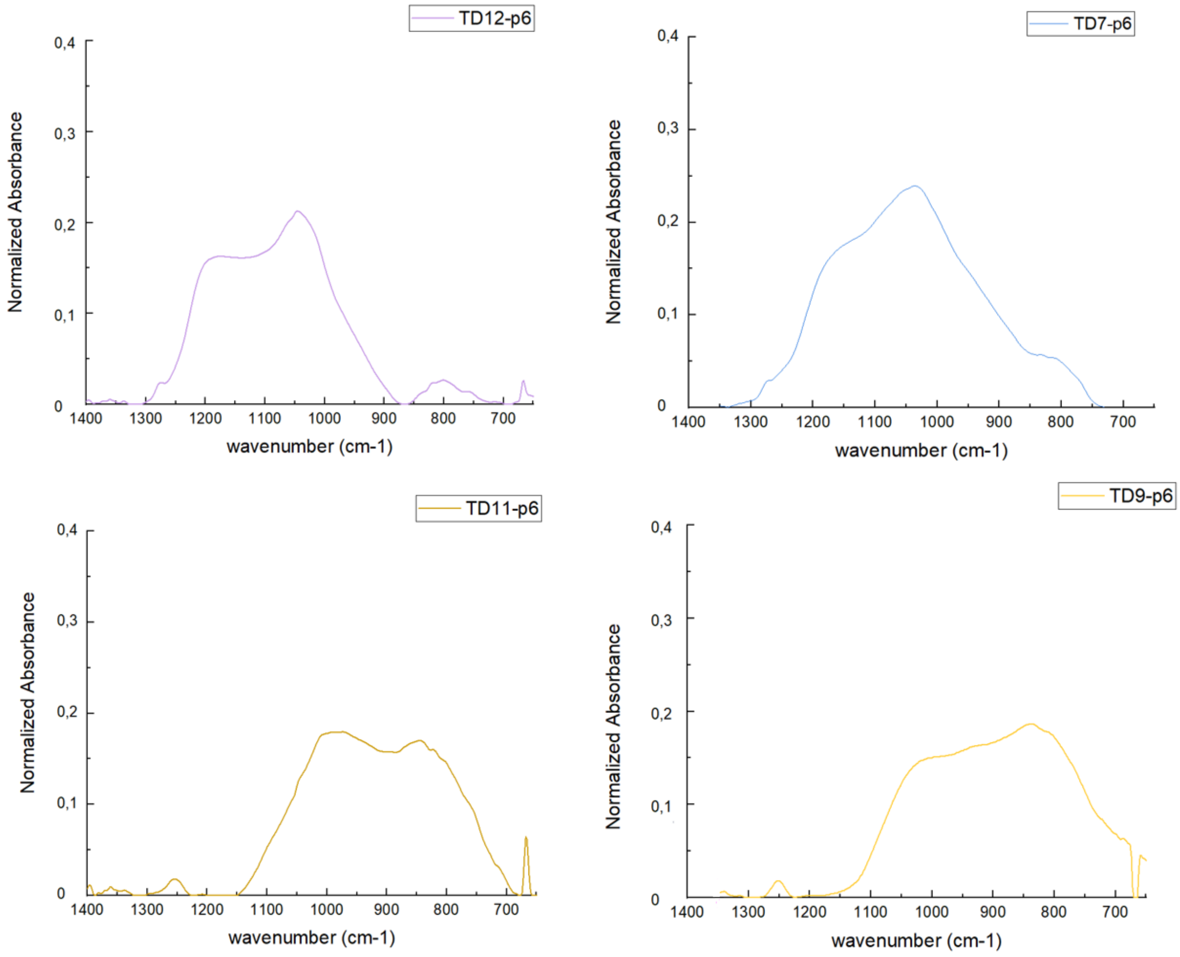

Figure 37: Evolution of the "fingerprint" area for the samples closest to the reactor exhaust. For these experiments, no ammonia was present in the gas phase.

Here, the evolution of the character of the films is much clearer. For the TD12 experiment, the silicon oxide character is evident, as expected thanks to the higher O_2 flow applied. The LO3-TO3 pair is clearly visible. For the TD7 experiment, the LO3-TO3 pair starts to disappear, and the whole band shifts towards lower wavenumbers. For the TD11 and TD9 experiments, the LO3-TO3 pair has disappeared completely, with the Si-CH_3 absorption at around 1260 cm^{-1} being now completely separated from the other absorptions. The whole band has moved towards lower wavenumbers because of the reduction in the intensity of the Si-O peaks (1050-1200 cm^{-1}), and the simultaneous great increase in intensity of the Si-N stretching mode (940 cm^{-1}). Additionally, absorbances at 850 cm^{-1} and 800 cm^{-1} become very pronounced for TD11 and TD9, assumed to be attributed to Si-N and Si-C vibrational modes. Moreover, the lack of Si-O absorption at 1200-1260 cm^{-1} leads to the assumption that the absorption at 1000-1020 cm^{-1} in these two experiments is most probably a Si-CH$_2$-Si absorption, usually hidden under the prominent Si-O character in other experiments. Generally, the TD11 and TD9 films display a character less similar to that of a silicon oxide film, developing a predominant silicon nitride character. In fact, samples produced in the TD9 and TD11 experiments, displayed a great resistance to chemical etching, as it will be discussed in chapter 4.4.

4.3 IBA results

The IBA results were used to compare the stoichiometry of samples from the same p2 position (as shown in Fig. 14), across experiments. Specifically, samples from the TD6, TD7, TD8 and the TD7, TD11, TD12 and TD14 experiments were probed with this method. The first group of samples can indicate differences in the sample composition for a varying oxygen and ammonia flow rates, while the second group of samples is used to investigate differences attributed to varying oxygen flow rates in the absence of ammonia. The TD7 samples can be used to make observations for both sets of experiments.

The results obtained by IBA provide information regarding the atomic composition of the films. This way, they can be used to calibrate and validate the 3-phase BEMA ellipsometry model, by fitting the density of the carbon phase as discussed in paragraph 2.1.2.

4.3.1 Effect of NH_3 flow rate on the atomic composition of the samples

For this study the nitrogen, hydrogen, and carbon content of experiments TD6, TD7 and TD8 was compared. The results were the following:

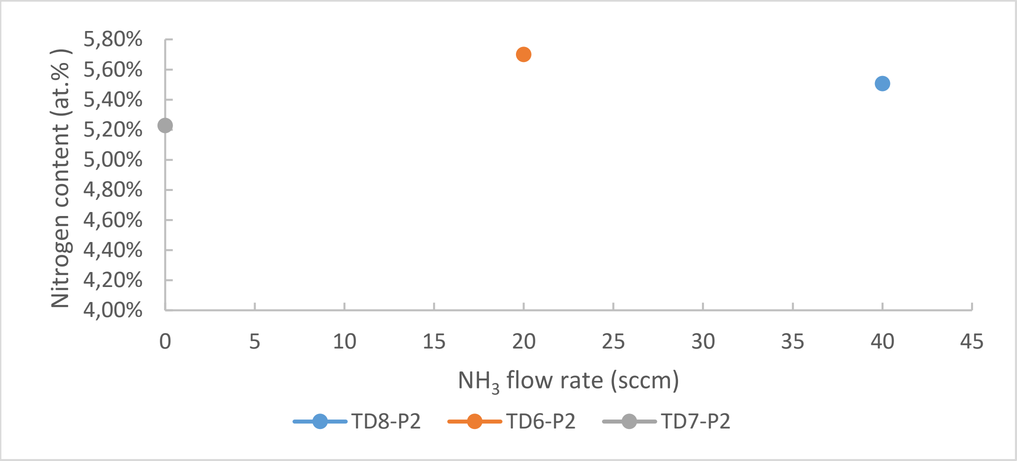

Figure 38: Effect of the NH_3 flow rate on the nitrogen content of the films based on the IBA results.

It appears that the nitrogen content of the film is not heavily influenced by the amount of ammonia used in the gas phase. This confirms the observations and assumptions of paragraph 4.1.2 – the fact that the nitrogen originates from the precursor and its content is mostly controlled by the precursor to oxygen flow ratio.

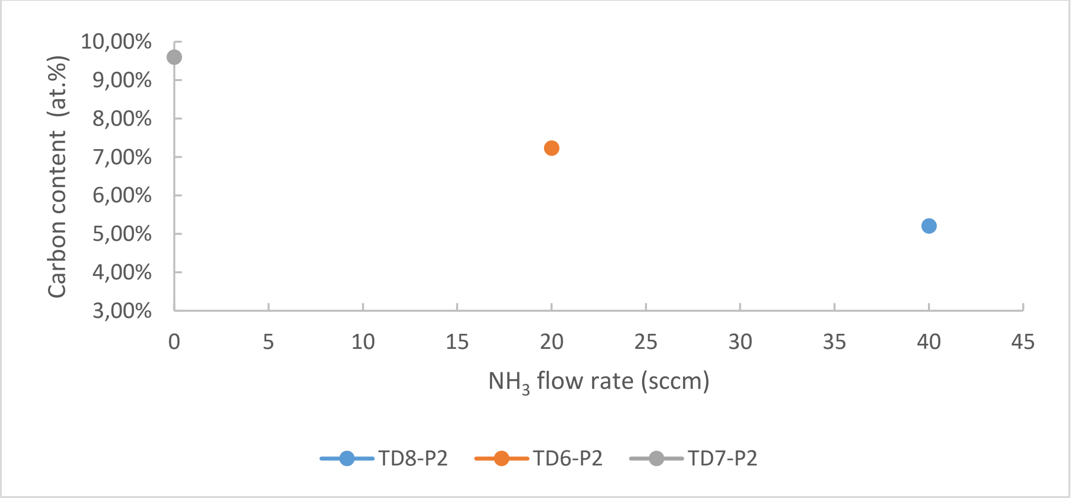

Figure 39: Effect of the NH3 flow rate on the carbon content of the films based on the IBA results

It appears that there is a correlation between the carbon content of the films and the NH_3 flow rate. The higher the amount of ammonia at the reactor's inlet, the lower the carbon content of the films. This could be caused by either the cleavage of the methyl ligands of the film by the ammonia [43], or maybe by the inhibition for film formation from several carbon-containing intermediates due to the presence of ammonia in the gas phase.

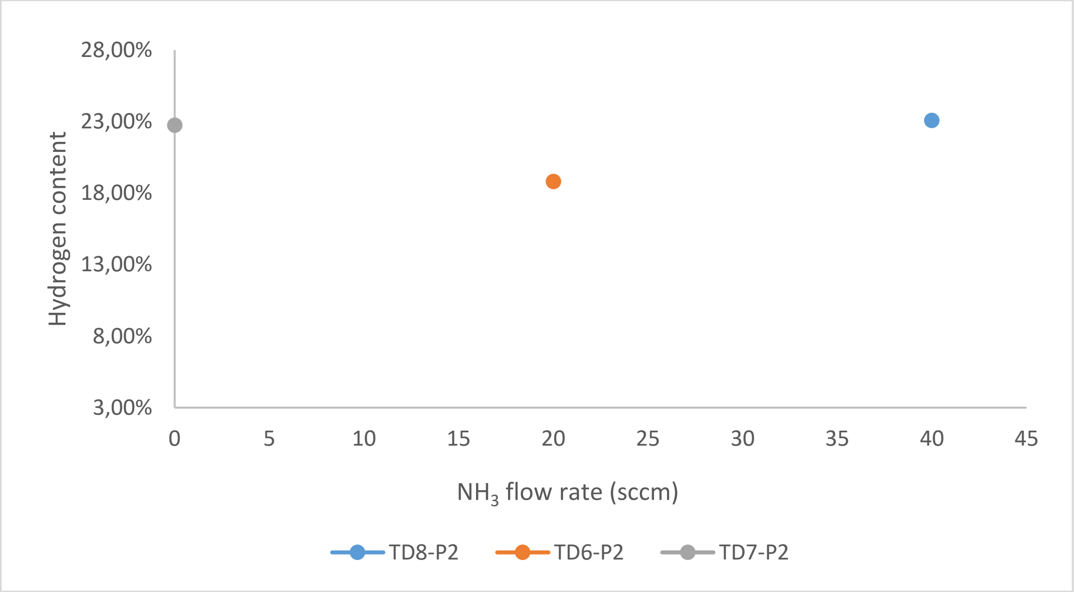

Figure 40: Effect of the NH3 flow rate on the hydrogen content of the films based on the IBA results.

In Fig. 40, no clear correlation between the ammonia flow rate and the hydrogen content of the film can be detected. Interestingly, the hydrogen percentage follows a reverse trend compared to that of the nitrogen content.

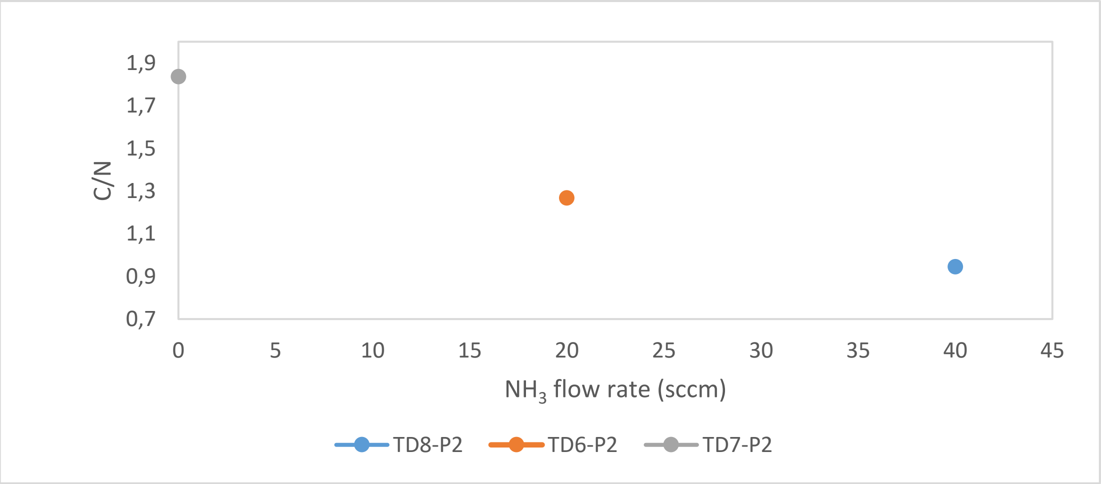

Figure 41: Effect of the NH_3 flow rate on the C/N ratio of the films based on the IBA results.

In Fig. 41, as expected, a trend similar to the evolution of the carbon content of the films is observed. As the ammonia flow rate increases, the carbon-to-nitrogen ratio of the films decreases. The possible reasons for this effect have been mentioned above.

4.3.2 Effect of O_2 flow rate on the atomic composition of the samples in absence of NH_3

For the study of the effect of the inlet oxygen flow rate on the atomic composition of the samples, the results of the TD7, TD11 and TD12 experiments have been compared. The results were the following:

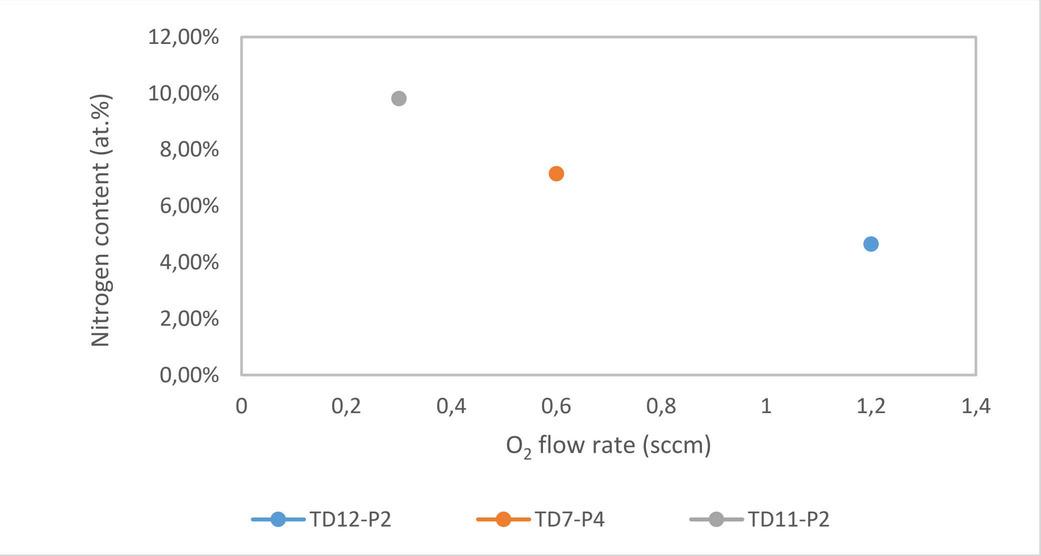

Figure 42: Effect of the O_2 flow rate in the absence of ammonia on the hydrogen content of the films based on the IBA results.

A clear correlation between the O_2 flow rate and the nitrogen content of the films can be observed. The higher the oxygen flow at the reactor's inlet is, the lower the nitrogen content of the films. An explanation for this could be that the nitrogen and oxygen incorporation in the film is done through different and competing reactions.

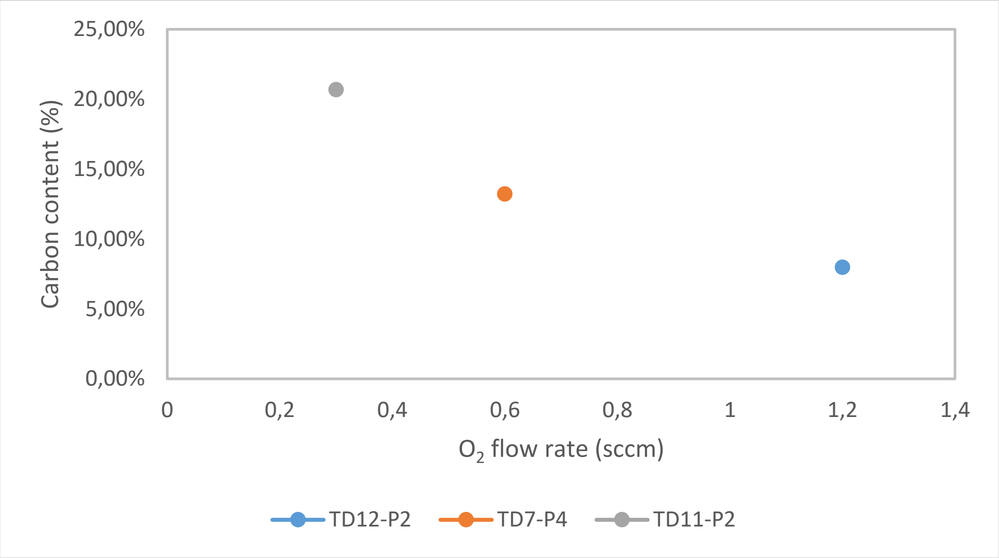

Figure 43: Effect of the O_2 flow rate in the absence of ammonia on the carbon content of the films based on the IBA results.

Here, a clear correlation between the carbon content present in the films and the oxygen flow rate can also be observed. The higher the oxygen flow rate, the lower the carbon content of the films. This could have 2 different explanations. The first is that the nitrogen and carbon are possibly deposited through the same molecule and same reaction, which, as stated above, is in competition with the reaction that causes the oxygen incorporation. The second is that the presence of oxygen in the gas phase might cause the cleaving of the carbon moieties present in the different intermediate species of the gas phase.

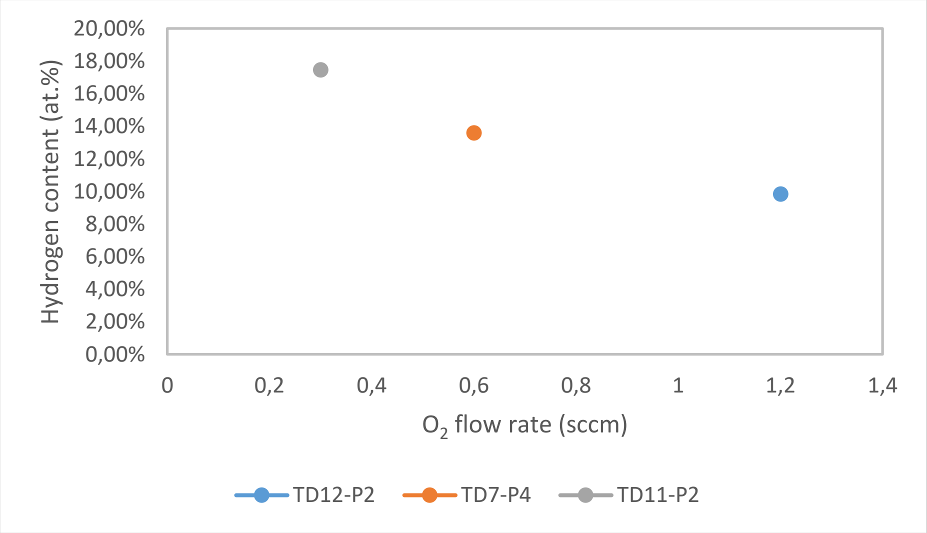

Figure 44: Effect of the O_2 flow rate in the absence of ammonia on the hydrogen content of the films based on the IBA results.

A clear correlation between the oxygen flow rate and the hydrogen content of the films can also be noticed. It appears that as the oxygen flow rate increases, the hydrogen content of the film drops to lower levels. This could be explained by the assumption that the major hydrogen containing chemical species in the film – such as N-H and $–CH_x$ – also contain carbon and nitrogen atoms, which, as established above, are also decreased by the increase of the O_2 flow rate. As a result, it is argued that the hydrogen content of the films is found predominantly in the form of N-H and $–CH_x$.

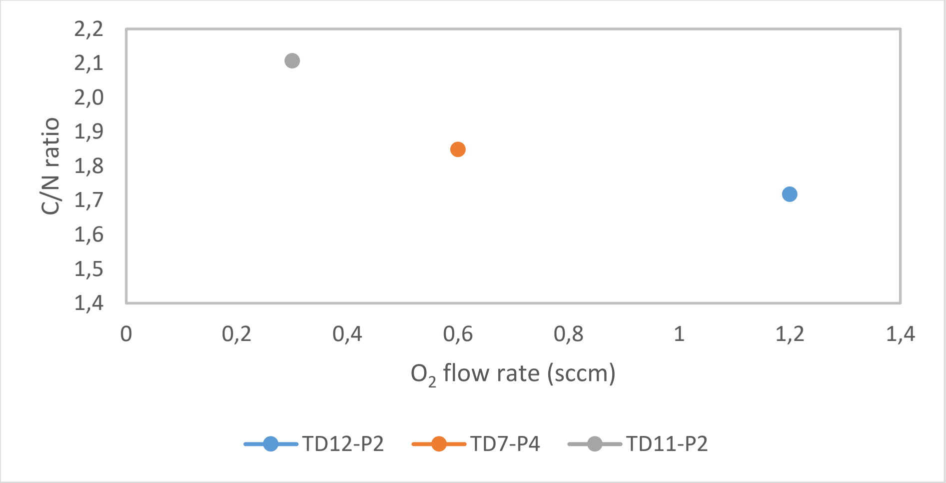

Figure 45: : Effect of the O_2 flow rate in the absence of ammonia on the C/N ratio of the films based on the IBA results.

The graph above provides the following information: The C/N ratio of the films appears to decrease with the increase of the oxygen flow rate. This comes against the explanation given above regarding the deposition of nitrogen and carbon by the same intermediates, because that would mean that the C/N ratio of the films would be constant. The results depicted in this graph are closer to the idea that the increase of oxygen concentration cleavages further the carbon moieties of several reactive intermediates of the gas phase, leading to the deposition of a carbon-nitride material that through intermediates that have progressively lower C/N atomic ratio.

4.3.3 Effect of temperature on the atomic composition of the samples

Experiments TD7 and TD14 were compared in order to investigate the effect of temperature in the final composition of the films. As stated in Table 2, the only difference between these two experiments is their deposition temperature, which was 650 °C for TD7 and 625 °C for TD14.

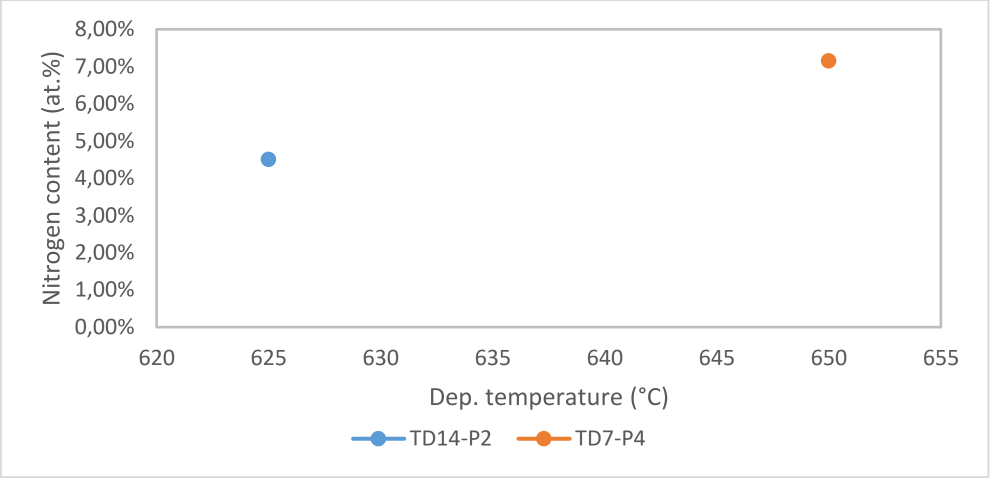

Figure 46:Effect of temperature on the nitrogen content of the films based on the IBA results.

It appears that the higher the temperature, the higher the nitrogen incorporation inside the films. A reason for this could be that the higher temperature either facilitates the reactions that cause the deposition of nitrogen-containing intermediates or increases the number of nitrogen-containing intermediates produced in the gas phase.

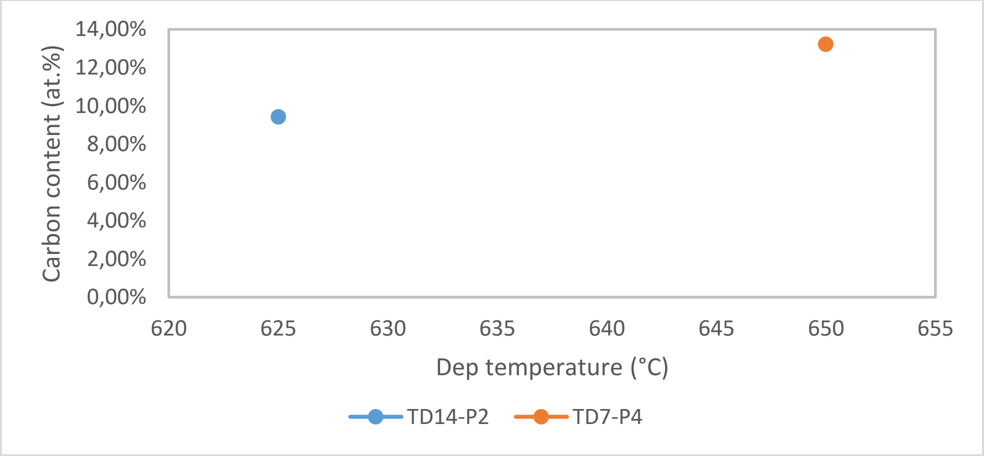

Figure 47: Effect of temperature on the carbon content of the films based on the IBA results.

Here, a tendency similar to that of the nitrogen content is observed. The higher the temperature, the higher the carbon incorporation inside the film. Taking into account the hypothesis made for the tendency of the nitrogen content, a higher temperature could translate to a plethora of nitrogen and carbon containing intermediates in the gas phase, which are in turn deposited on the film with several surface reactions.

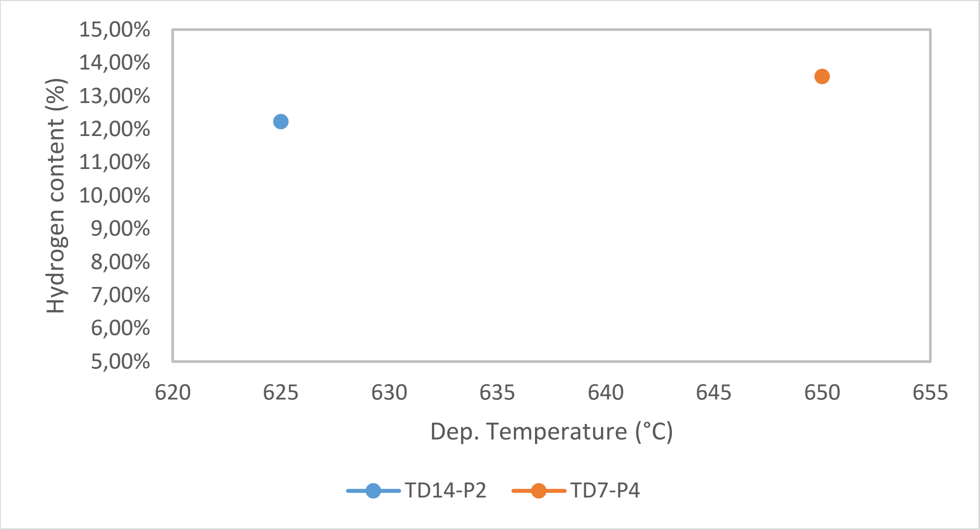

Figure 48: Effect of the deposition temperature on the hydrogen content of the films based on the IBA results.

Following the trend of the nitrogen and carbon content of the films, the hydrogen content of the films also increases with increasing temperature. This result could be supported by the fact that the main hydrogen-containing species found on the films through FTIR are N-H and -CH_X – not ignoring of course the presence of Si-OH. Therefore, an increase of the nitrogen and carbon content of the films appears to also result in a subsequent increase of the hydrogen content.

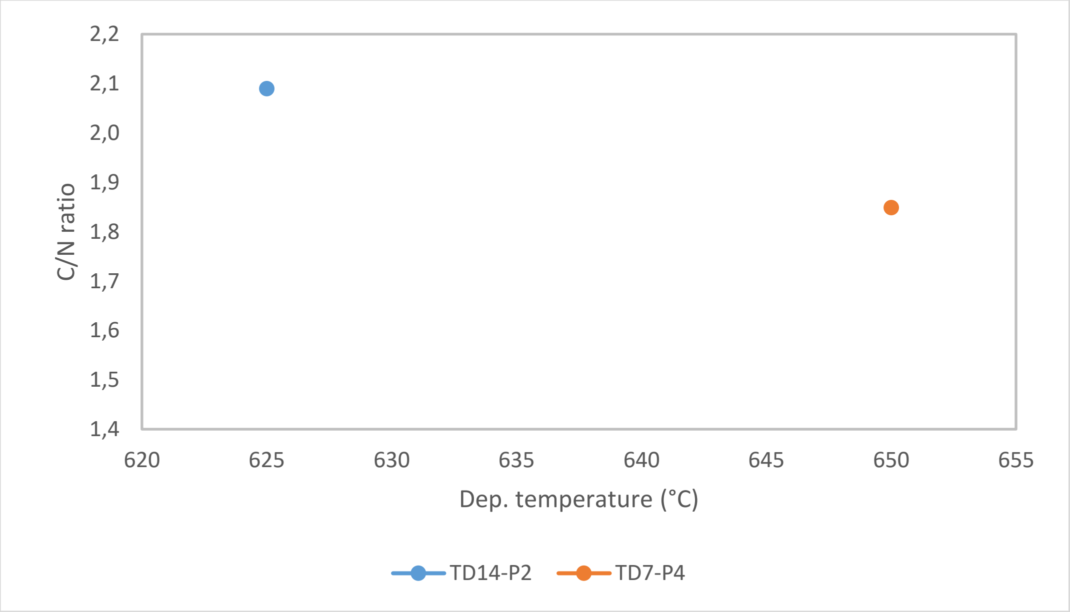

Figure 49: Effect of the deposition temperature on the C/N ratio of the films based on the IBA results.

Interestingly, the C/N ratio of the films seems to decrease with an increase in temperature. It is recalled that the oxygen flow rate was constant in these two experiments. This could mean that either carbon is incorporated via different intermediates depending on the temperature, with intermediates containing more carbon atoms being more common at lower temperatures.

Another possibility is that the carbon-cleaving effect of the oxygen is more effective at higher temperatures. Even though the carbon content increases with the temperature, the C/N ratio decreases, hinting at a simultaneous activation of the carbon-cleavaging effect, and an activation of the carbon-nitride film-forming intermediate, which at higher temperatures has lost some of its carbons.

4.3.4 Calibration and validation of the 3-phase BEMA ellipsometry model for samples produced under an ammonia-free gas phase

As stated at the beginning of the chapter, certain IBA results were necessary for the calibration – and later for the validation – of the 3-phase BEMA ellipsometry model. Using the IBA results derived for the TD3-p2 sample (10.7% C and 5.8% N), the carbon density needed for the calculations of the 3-phase model was fitted. It was determined equal to 0.652 g/cm^3 and provided excellent fit for the carbon content of the film and provided a nitrogen content equal to 4.6%. A carbon phase with such a low density can be explained by the fact that this phase was added to the model just to provide an estimation of the carbon content and should not be thought of as a clear carbon phase. There are natures of carbon mentioned in the literature, such as soot [44], with a density comparable to the one used to calibrate our model. The film of course, does not contain soot, but in order to provide reasonable estimations using this model, a lower than expected value for the density of the carbon phase must be tolerated. After all, this hypothetical “carbon phase” could contain a lot of hydrogen and other impurities.

After finding the value of the density, the model was tested and compared with the IBA results of the TD11, TD12, TD14 experiments. The results were the following:

Table 3: Comparison of the 3-phase BEMA model and IBA results.

Experiment	**at% nitrogen 3-phase BEMA model**	**at% nitrogen IBA**	**at% carbon 3-phase BEMA model**	**at% carbon IBA**
TD11	12.7	9.8	24.5	20.7
TD12	2.9	4.7	8.6	8.0
TD14	3.2	4.5.	8.9	9.4

One could say that the model provides estimations regarding the nitrogen and carbon content of the films, that is not far from the more accurate results provided by the IBA methods. It should be noted however, that the ellipsometry model that is used cannot provide information on the hydrogen content of the films. That means that the atomic contents that are provided by this model, especially that of silicon and oxygen, contain inside them a "hidden" hydrogen atomic percentage, which is ignored by the model.

4.4 Wet etching corrosion resistance

A (6:1) buffered oxide etch (BOE) solution (6 parts of NH_4F (40%) and 1 part of HF (49%), Sigma Aldrich), was used in order to determine the wet etching corrosion rates of the produced films. This type of etching solution is used mainly on silicon nitride films (Si_3N_4), however its use in silicon oxynitride can also provide valuable results. This specific solution was chosen after preliminary results of wet etching corrosion tests conducted with the Pliskin solution (3 parts hydrofluoric acid (49 %), 2 parts of nitric acid (70 %), and 60 parts of distilled water) made it clear that the samples were fully resistant to it. As such, the more aggressive BOE solution was selected.

Resistance to this type of etching is considered important for determining the barrier properties of the films and therefore for their desired applied use. Some authors have correlated the etching rate of silicon nitride films to their hydrogen content [45], while more recent studies have suggested that the etching rate is higher for films with higher N-H bond contents [46] or films containing higher hydrogen content in general[47]. However, other authors have mentioned that silicon nitride films deposited over an oxide layer can provide better surface passivation [48]. This could be the case with a silicon oxynitride film, and therefore the BOE wet etching corrosion test was selected to investigate the films' corrosion resistance.

Ellipsometry measurements of the films were taken before the test. Afterwards, the sample are placed in the BOE solution and the duration of etching is timed using a stopwatch. After that, ellipsometry measurements are taken again in order to determine the thickness loss over the etching time measured by the stopwatch, giving as such the respective etching rate. The nitrogen content of the film was determined by using the 2-phase ellipsometry model. Then, the etching rates of the films were plotted against their nitrogen content. The results were the following:

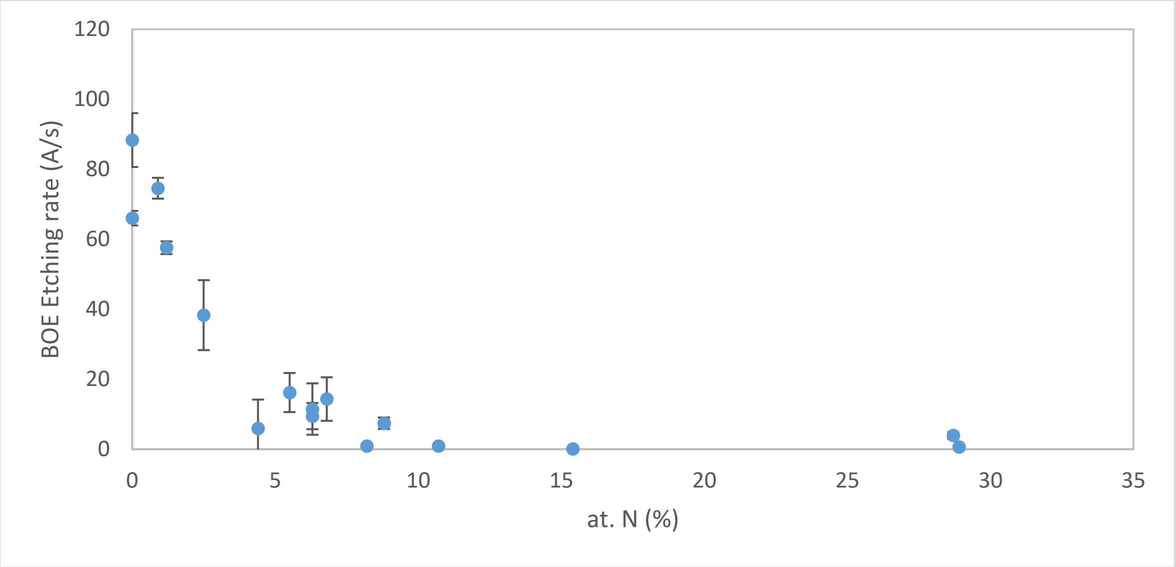

Figure 50: Effects of the film nitrogen content (as calculated by the 2-phase ellipsometry model) on the BOE etching rate.

It appears that the nitrogen content of the films plays a significant role on the etching rate of the produced silicon oxynitride films. The higher the nitrogen content of the films, the lower the observed etching rate, and as such, the higher the resistance of the material against corrosion. The highest resistance to the BOE test was displayed on the following samples:

1. TD5-p3, which was produced under an oxygen free gas phase, using only O_2 and TDMSA as the reactants, and having a nitrogen content of 15.4%.
2. TD11-p3, which was produced under an ammonia free gas phase, using 0.3 sccm of O_2, with a nitrogen content of 28.9%.
3. TD3-p6, which was produced using excess TDMSA, O_2 and NH_3 in the gas phase, with a nitrogen content of 10.7%.
4. TD9-p3, which was produced using only TDMSA in the gas phase, with a nitrogen content of 28.7%.

It is observed that, despite the differences in gas phase composition, any sample with a nitrogen content higher than 8 at.% had a remarkable resistance against corrosion.

Additionally, the etching rate results were plotted against the Si-N stretching mode and Si-O-Si TO3 peak positions of the several films, in order to investigate a possible correlation. The results were the following:

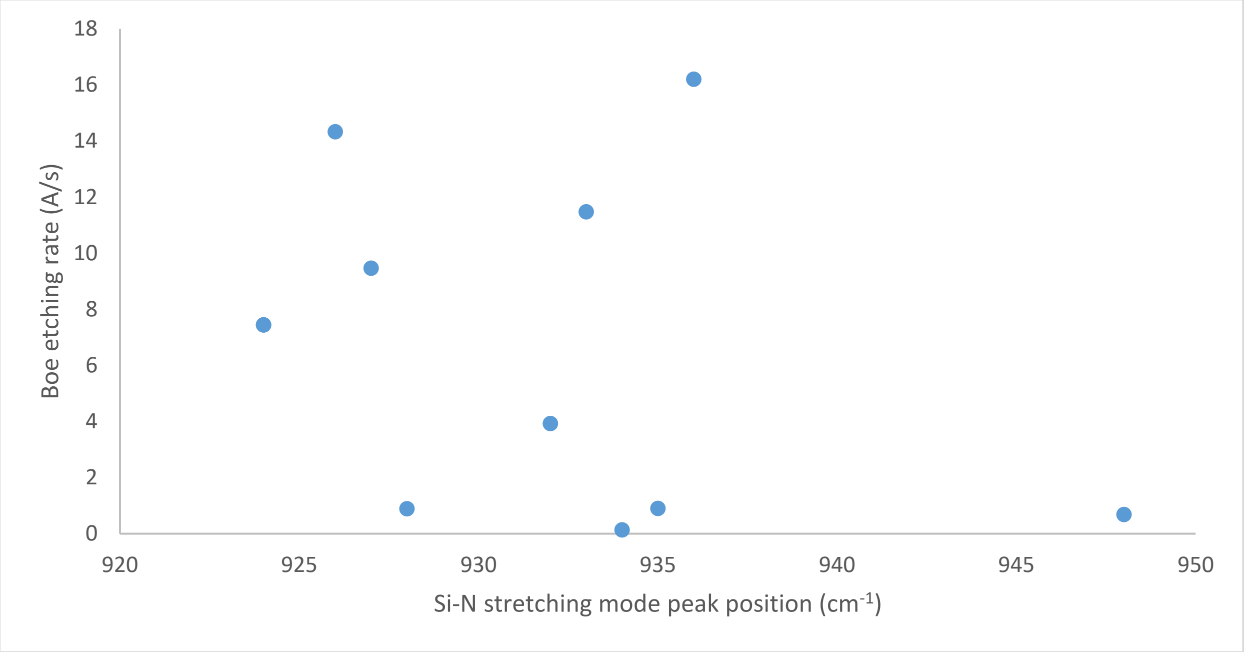

Figure 51: Effect of the Si-N stretching mode peak position on the observed etching rate.

No specific correlation between the position of the main Si-N peak observed by FTIR and the calculated etching rate was observed.

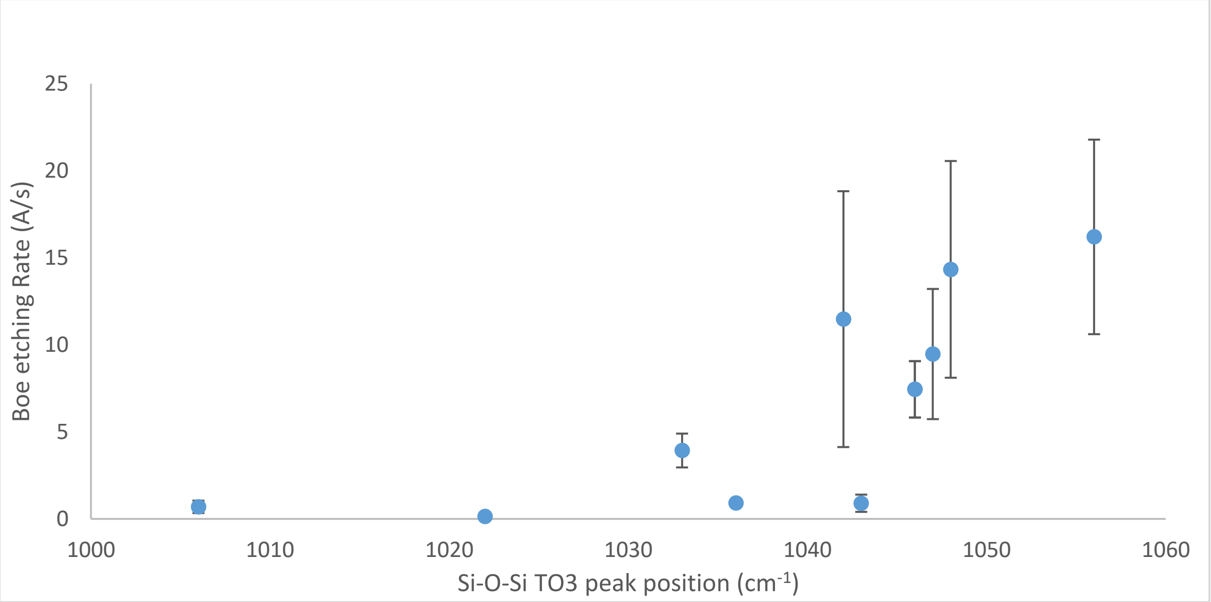

Figure 52: Effect of the Si-O-Si TO3 stretching mode peak position on the observed etching rate.

However, a visible correlation exists between the etching rate and the Si-O-Si peak position. The higher the wavenumber of the peak position, the higher the etching rate of the film. The exponential behavior of this plot is similar to the reverse exponential trend of the etching rate plotted as a function of the nitrogen content (Fig. 50). As an indirect correlation, it is proposed that the increase of the nitrogen content in the films is one of the factors that drives the shift of the Si-O-Si TO3 peak towards lower wavenumbers, and is additionally the key parameter for the improvement of the etching rate.

5. Conclusions

The solid phase analysis of the produced films is of great importance, when the need for process optimization is vital for the improvement of the films' properties relating to the target applications. The results obtained via the analysis of the solid phase can contribute greatly to the establishment of the correlation between the process conditions, the structure and properties of the film and the film's performance. The analysis of the solid phase of films produced under a plethora of varying experimental conditions can show the way towards the most favorable process conditions, under which a film, with the best properties for the targeted performance requirements, can be produced. Apart from that, the results of the solid phase analysis – combined with the results of the reactor's gas phase analysis – is essential information for the development of a representative chemical model, which could be used to formulate a realistic deposition mechanism. In turn, the development of an accurate chemical model, will aid the simulation of the deposition process. As a consequence, such simulations can be used for process optimization, and for the prediction of multiple potential sets of flow rate, temperature, and gas phase composition parameters using the TDMSA/ NH_3/ O_2 chemical system, that would otherwise be too time- and material-consuming to test with actual experiments via a trial and error approach.

Via the use of ellipsometry, accurate results regarding the films' thickness were given. This method was used for the measurement of the deposition rate of each experiment and was therefore of great use for the construction of the aforementioned model development. Additionally, ellipsometry provided certain trends (via the use of the 2-phase BEMA model) regarding the nitrogen content and thickness of the films, sample by sample, as an evolution of the position and local temperature inside the reactor. It was observed that the deposition rate is highly dependent on the flow rate of O_2, with oxygen being the main promoter for film formation, increasing the deposition rate with higher oxygen flows. However, a higher O_2 flow rate also hindered the incorporation of nitrogen inside the films, a result globally observed across all experiments. On the other hand, an increase in NH_3 flow rate appeared to slightly hinder both the deposition rate and the nitrogen incorporation inside the films. Through a series of experiments, which validated that the incorporated nitrogen actually originates from the TDMSA precursor, it is concluded that, for the flow rates and temperature ranges that were studied, the addition of ammonia in the gas phase is redundant and can be ignored.

The increase in the flow rate of the TDMSA precursor increased the deposition rate, with the maximum deposition rate being observed closer to the inlet of the reactor. However, after this maximum, the deposition rate decreases, and it is concluded that the consumption of the available oxygen in the gas phase is the reason to decreasing deposition rates observed at the exhaust of the reactor. The addition of TDMSA precursor also led to a dramatic increase in the nitrogen incorporation inside the films, further confirming the conclusion that the incorporated nitrogen stems from the TDMSA compound.

As expected for endothermic reactions, the use of lower temperatures leads to a decreased overall deposition rate, while at higher temperatures, the various surface reactions that form the SiO_xN_y film can take place with higher reaction rates. A key result was that the decrease in temperature also negatively affected the nitrogen incorporation, hinting at a clear requirement for higher temperatures when elevated concentrations of nitrogen are desired in the produced material. Finally, the combination of FTIR analysis and the correlation of its results to those of ellipsometry, confirmed the conclusion the nitrogen-containing species originate from the precursor molecule and not from the added NH_3 gas that is supplied in the reactor.

Via the use of FTIR, the several types of species present in the films could be observed. In all the films studied, either the Si-O stretching mode or the Si-N stretching mode were the predominant absorptions observed in the spectra. Most of the work involved the tracking of their intensity and their position across all experiments. The films also contained several hydrogen related species, such as Si-OH and H_2O. The general trend that was observed, was that the use of lower flow rates of O_2 led to a shift of the Si-O and Si-N peaks towards lower wavenumbers. This is a sign of higher nitrogen incorporation inside the films [39], [40]. The general character of the films shifted from a silicon oxide character to a silicon nitride character, depending on the amount of O_2 present in the gas phase. The less the oxygen present in the gas phase, the more the films obtain a character closer to a silicon nitride than a silicon oxide. This was very evident in experiments where little to no oxygen was used. In those experiments, the spectra obtained through FTIR were surprisingly different from spectra of other experiments. They were in a category of their own – due to their carbon content – and led to the reconsideration of the 2-phase BEMA ellipsometry model, highlighting the need of a 3-phase BEMA model, which, in addition to the SiO_2 and Si_3N_4 phases, is also considering an amorphous carbon phase. Furthermore, no evident Si-H peaks were observed in the spectra, something that leads to the assumption that the amount of hydrogen bonded uniquely to silicon is very low. The complexity of the precursor, TDMSA, was also evident on the resulting films. Not only were its $–CH_3$ moieties identified in the produced materials, but it also led to multiple different chemical species.

The family of IBA methods (RBS, ERDA and NRA) were of utter importance for the confirmation of the trends observed through ellipsometry and FTIR and for the calibration of the 3-phase BEMA model. Indeed, through the results of the IBA methods, it was confirmed that an increased O_2 flow rate leads to films poorer in nitrogen and carbon. It was also confirmed that the use of lower temperatures hinders nitrogen deposition. Additionally, based on the IBA results, it appears that increased flow rates of both NH_3 and O_2 lead to a decreased nitrogen content inside the films. However, the increase of ammonia resulted in lower carbon percentages, through cleavaging of the methyl ligands, as is known from the literature. Oxygen appears to inhibit the deposition of intermediates containing a high number of carbon atoms. This could either mean that the majority of carbon is contained in the species that are responsible for the co-deposition of nitrogen and carbon, or that O_2 in the gas phase reduces the methyl moieties contained in the different intermediates, which then result in the formation of nitrogen-containing films poorer in carbon. IBA also indicated respectable amount of hydrogen inside the films, something, which combined with the FTIR results, points to a high amount of N-H, Si-OH and CH_x species inside the produced material.

Via the chemical etching by a BOE solution, results regarding the performance of the films against wet etching corrosion were acquired. It appears that the nitrogen content of the films is the key parameter that impacts the resistance to corrosion, with higher nitrogen contents significantly improving the anticorrosion behaviour. Additionally, it was concluded that as long as the nitrogen content exceeded a value of approximately 8 at.%, films had a remarkable and similar corrosion resistance, regardless of the gas phase composition under which they had been produced. For these samples, the etching rate dropped at values lower than 1 $A.s^{-1}$. No direct correlation could be made between the position of the Si-N absorption to the etching rate, however a trend was observed for the Si-O absorption, indicating that an increase in nitrogen content shifts the Si-O absorption towards lower wavenumber and simultaneously improves the corrosion resistance by decrease the etching rate.

In summary, all the above results and trends were of great aid in deciding new experimental parameters. The analysis of the films produced in the absence of oxygen and ammonia was a turning point for the project, which led to the adoption of an ammonia-free chemistry for the experiments following thereafter. The deposition rate and nitrogen deposition for the following experiments was then only determined by adjusting the oxygen-to-TDMSA ratio. This ratio was found to have the biggest effect on the resulting films, their composition, chemical structure and therefore their functional properties. Lastly, the ellipsometry results were also of great importance and helped in the systematic extraction and use of a large amount of data, which played the key role for the development of the chemical model and the process simulation.

6. Perspectives

As an extension of the results of the present work, several ideas for further research and improvement are proposed.

First, the further calibration, validation, and improvement of the three-phase ellipsometry model could be of great importance. By using this model, important approximations can be made regarding the films' composition across multiple samples in the reactor, without having to pass every single sample through the more costly and time-consuming IBA characterizations techniques. Proposals for further improvement of the model are AFM analyses for the definition of a surface roughness layer, as well as SEM or TEM cross-section analyses, for the validation of selected samples' film thickness.

Second, the effect on the carbon and hydrogen content of the films on their etching resistance must be further investigated. Because the IBA methods were the only techniques able to give accurate hydrogen percentages, it is highly suggested to couple these methods with the wet etching corrosion test. Alternatively, a further calibration of the three-phase ellipsometry model, that would additionally give information on the hydrogen content, could also be used.

Third, the possible correlation between the position of the Si-O-Si TO3 peak and the films' performance in chemical etching tests must be further investigated, through additional etching and FTIR results, to enrich the current database.

While for silicon nitride films, an increased amount of N-H [46] species and the increased amount of nitrogen and hydrogen content inside the film [47] seems to result in worse performance against corrosive solutions, this does not seem to be the case for the films produced by this work. An increase in nitrogen content seems to be the main factor impacting the films' performance in the wet etching test. However, the effect of the N-H species amount on the films' performance should be further investigated, by combining FTIR and IBA results.

The complexity of the FTIR spectra does not allow the precise identification of some peaks. The value of XPS analysis for the distinction and the quantification of the several species bonded to silicon atoms will be of great importance for a deeper understanding and a more precise identification of the network existing inside the films. This way, light will be shed to the amount of oxygen, nitrogen and carbon connected to silicon atoms within the film.

Finally, in order to have a better understanding of the factors that lead to a better film performance, emphasis should be place on the solid-state NMR[49]. Moreover, the wettability of the films could be of great importance in their performance in applications relating to corrosion. For this reason, surface energy analysis results would be of great interest. Both the results of NMR and the surface energy calculations should be correlated with the results of the present work, in order to provide a clear and complete idea regarding the factors, which impact the films’ anti-corrosion and barrier behaviour. Lastly, the importance of each of these factors to the films’ performance should be investigated.

References

[1] Y.-X. Zheng, R.-J. Zhang, and L.-Y. Che, ‘Ellipsometry and Its Applications in Stoichiometry’, in *Stoichiometry and Materials Science - When Numbers Matter*, A. Innocenti, Ed. InTech, 2012.

[2] H. G. Tompkins and E. A. Irene, Eds., *Handbook of ellipsometry*. Norwich, NY : Heidelberg, Germany: William Andrew Pub. ; Springer, 2005.

[3] D. A. Skoog, F. J. Holler, and S. R. Crouch, ‘An Introduction to Infrared Spectrometry’, in *Principles of instrumental analysis*, 6th ed., vol. 16, 34 vols, Belmont, CA: Thomson Brooks/Cole, 2007, pp. 430–454.

[4] D. A. Skoog, F. J. Holler, and S. R. Crouch, ‘Components of Optical Instruments’, in *Principles of instrumental analysis*, 6th ed., vol. 7, 34 vols, Belmont, CA: Thomson Brooks/Cole, 2007, pp. 164–212.

[5] W. D. Perkins, ‘Fourier transform infrared spectroscopy. Part II. Advantages of FT-IR’, *J. Chem. Educ.*, vol. 64, no. 11, p. A269, Nov. 1987, doi: 10.1021/ed064pA269.

[6] B. C. Smith, *Fundamentals of Fourier Transform Infrared Spectroscopy*, 0 ed. CRC Press, 2011.

[7] W. Bensch and W. Bergholz, ‘An FT-IR study of silicon dioxides for VLSI microelectronics’, *Semicond. Sci. Technol.*, vol. 5, no. 5, pp. 421–428, May 1990, doi: 10.1088/0268-1242/5/5/008.

[8] S. Ponton *et al.*, ‘Investigation of the densification mechanisms and corrosion resistance of amorphous silica films’, *J. Non-Cryst. Solids*, vol. 515, pp. 34–41, Jul. 2019, doi: 10.1016/j.jnoncrysol.2019.04.005.

[9] A. Pecora, L. Maiolo, G. Fortunato, and C. Caligiore, ‘A comparative analysis of silicon dioxide films deposited by ECR-PECVD, TEOS-PECVD and Vapox-APCVD’, *J. Non-Cryst. Solids*, vol. 352, no. 9–20, pp. 1430–1433, Jun. 2006, doi: 10.1016/j.jnoncrysol.2005.10.030.

[10] G. Beshkov, S. Lei, V. Lazarova, N. Nedev, and S. S. Georgiev, ‘IR and Raman absorption spectroscopic studies of APCVD, LPCVD and PECVD thin SiN films’, *Vacuum*, vol. 69, no. 1–3, pp. 301–305, Dec. 2002, doi: 10.1016/S0042-207X(02)00349-4.

[11] F. Giorgis *et al.*, ‘Optical, structural and electrical properties of device-quality hydrogenated amorphous silicon-nitrogen films deposited by plasma-enhanced chemical vapour deposition’, *Philos. Mag. B*, vol. 77, no. 4, pp. 925–944, Apr. 1998, doi: 10.1080/13642819808206395.

[12] F. Ay and A. Aydinli, ‘Comparative investigation of hydrogen bonding in silicon based PECVD grown dielectrics for optical waveguides’, *Opt. Mater.*, vol. 26, no. 1, pp. 33–46, Jun. 2004, doi: 10.1016/j.optmat.2003.12.004.

[13] B. Hallam, B. Tjahjono, and S. Wenham, ‘Effect of PECVD silicon oxynitride film composition on the surface passivation of silicon wafers’, *Sol. Energy Mater. Sol. Cells*, vol. 96, pp. 173–179, Jan. 2012, doi: 10.1016/j.solmat.2011.09.052.

[14] A. del Prado, I. Mártil, M. Fernández, and G. González-Díaz, ‘Full composition range silicon oxynitride films deposited by ECR-PECVD at room temperature’, *Thin Solid Films*, vol. 343–344, pp. 437–440, Apr. 1999, doi: 10.1016/S0040-6090(98)01701-5.

[15] M. A. Schiavon, K. J. Ciuffi, and I. V. P. Yoshida, ‘Glasses in the SiOCN system produced by pyrolysis of polycyclic silazane/siloxane networks’, *J. Non-Cryst. Solids*, vol. 353, no. 22–23, pp. 2280–2288, Jul. 2007, doi: 10.1016/j.jnoncrysol.2007.03.004.

[16] L. M. Zambov, B. Ivanov, C. Popov, G. Georgiev, I. Stoyanov, and D. B. Dimitrov, ‘Characterization of low-dielectric constant SiOCN films synthesized by low pressure chemical vapour deposition’, *J. Phys. IV*, vol. 11, no. PR3, pp. Pr3-1005-Pr3-1012, Aug. 2001, doi: 10.1051/jp4:20013126.

[17] M. Jackson and H. H. Mantsch, ‘The Use and Misuse of FTIR Spectroscopy in the Determination of Protein Structure’, *Crit. Rev. Biochem. Mol. Biol.*, vol. 30, no. 2, pp. 95–120, Jan. 1995, doi: 10.3109/10409239509085140.

[18] C. Jeynes and J. L. Colaux, ‘Thin film depth profiling by ion beam analysis’, *The Analyst*, vol. 141, no. 21, pp. 5944–5985, 2016, doi: 10.1039/C6AN01167E.

[19] M. Mayer, ‘Rutherford Backscattering Spectrometry (RBS)’, presented at the Workshop on Nuclear Data for Science and Technology: Materials Analysis, Trieste, May 19, 2003, Accessed: Sep. 02, 2020. [Online]. Available: http://users.ictp.it/~pub_off/lectures/lns022/Mayer_1/Mayer_1.pdf.

[20] Y. Serruys, J. Tirira, and P. Trocellier, ‘A new IBA handbook on ERDA’, in *AIP Conference Proceedings*, Denton, Texas (USA), 1999, pp. 579–582, doi: 10.1063/1.59197.

[21] M. Mayer, ‘Nuclear Reaction Analysis (NRA)’, presented at the Workshop on Nuclear Data for Science and Technology: Materials Analysis, Trieste, May 19, 2003, Accessed: Sep. 03, 2020. [Online].

[22] Hugh O. Pierson, *Handbook of chemical vapor deposition*, 2nd ed. Norwich, NY: Noyes Publications, 1999.

[23] K. C. Topka *et al.*, ‘Large temperature range model for the atmospheric pressure chemical vapor deposition of silicon dioxide films on thermosensitive substrates’, *Chem. Eng. Res. Des.*, vol. 161, pp. 146–158, Sep. 2020, doi: 10.1016/j.cherd.2020.07.007.

[24] B. Harbecke, B. Heinz, and P. Grosse, ‘Optical properties of thin films and the Berreman effect’, *Appl. Phys. Solids Surf.*, vol. 38, no. 4, pp. 263–267, Dec. 1985, doi: 10.1007/BF00616061.

[25] D. F. Swinehart, ‘The Beer-Lambert Law’, *J. Chem. Educ.*, vol. 39, no. 7, p. 333, Jul. 1962, doi: 10.1021/ed039p333.

[26] N. Primeau, C. Vautey, and M. Langlet, ‘The effect of thermal annealing on aerosol-gel deposited SiO2 films: a FTIR deconvolution study’, *Thin Solid Films*, vol. 310, no. 1–2, pp. 47–56, Nov. 1997, doi: 10.1016/S0040-6090(97)00340-4.

[27] C. K. Wong, H. Wong, C. W. Kok, and M. Chan, ‘Silicon oxynitride prepared by chemical vapor deposition as optical waveguide materials’, *J. Cryst. Growth*, vol. 288, no. 1, pp. 171–175, Feb. 2006, doi: 10.1016/j.jcrysgro.2005.12.022.

[28] D. Rouchon, N. Rochat, F. Gustavo, A. Chabli, O. Renault, and P. Besson, ‘Study of ultrathin silicon oxide films by FTIR-ATR and ARXPS after wet chemical cleaning processes’, *Surf. Interface Anal.*, vol. 34, no. 1, pp. 445–450, Aug. 2002, doi: 10.1002/sia.1335.

[29] S. González-Castilla *et al.*, ‘Silicon oxide sacrificial layers deposited by pulsed-DC magnetron sputtering for MEMS applications’, Dresden, Germany, May 2009, p. 73620X, doi: 10.1117/12.821485.

[30] Z. Yin and F. W. Smith, ‘Optical dielectric function and infrared absorption of hydrogenated amorphous silicon nitride films: Experimental results and effective-medium-approximation analysis’, *Phys. Rev. B*, vol. 42, no. 6, pp. 3666–3675, Aug. 1990, doi: 10.1103/PhysRevB.42.3666.

[31] A. Fejfar, J. Zemek, and M. Trchová, ‘Hydrogen and nitrogen bonding in silicon nitride layers deposited by laser reactive ablation: Infrared and x-ray photoelectron study’, *Appl. Phys. Lett.*, vol. 67, no. 22, pp. 3269–3271, Nov. 1995, doi: 10.1063/1.114894.

[32] C. H. Huang, N. F. Wang, Y. Z. Tsai, C. C. Liu, C. I. Hung, and M. P. Houng, ‘The formation of a SiOx interfacial layer on low-k SiOCH materials fabricated in ULSI application’, *Mater. Chem. Phys.*, vol. 110, no. 2–3, pp. 299–302, Aug. 2008, doi: 10.1016/j.matchemphys.2008.02.023.

[33] J. H. Lee, C. H. Jeong, J. T. Lim, V. A. Zavaleyev, S. J. Kyung, and G. Y. Yeom, ‘SiOxNy thin film deposited by plasma enhanced chemical vapor deposition at low temperature using HMDS–O2–NH3–Ar gas mixtures’, *Surf. Coat. Technol.*, vol. 201, no. 9–11, pp. 4957–4960, Feb. 2007, doi: 10.1016/j.surfcoat.2006.07.075.

[34] T. Kaneko, D. Nemoto, A. Horiguchi, and N. Miyakawa, ‘FTIR analysis of a-SiC:H films grown by plasma enhanced CVD’, *J. Cryst. Growth*, vol. 275, no. 1–2, pp. e1097–e1101, Feb. 2005, doi: 10.1016/j.jcrysgro.2004.11.128.

[35] Q. Su *et al.*, ‘Microstructure-mechanical properties correlation in irradiated amorphous SiOC’, *Scr. Mater.*, vol. 146, pp. 316–320, Mar. 2018, doi: 10.1016/j.scriptamat.2017.11.053.

[36] E. H. Oulachgar, C. Aktik, S. Dostie, R. Sowerby, S. Gujrathi, and M. Scarlete, ‘Chemical and Structural Characterization of SiONC Dielectric Thin Film Deposited by PSCVD’, *J. Electrochem. Soc.*, vol. 153, no. 11, p. F255, 2006, doi: 10.1149/1.2338664.

[37] A. R. Chauhan, G. Bhatt, A. D. Yadav, S. K. Dubey, and T. K. Gundu Rao, ‘Synthesis of silicon oxynitride layers by dual ion-implantation and their annealing behaviour’, *Nucl. Instrum. Methods Phys. Res. Sect. B Beam Interact. Mater. At.*, vol. 212, pp. 451–457, Dec. 2003, doi: 10.1016/S0168-583X(03)01837-8.

[38] J. Dupuis, E. Fourmond, J. F. Lelièvre, D. Ballutaud, and M. Lemiti, ‘Impact of PECVD SiON stoichiometry and post-annealing on the silicon surface passivation’, *Thin Solid Films*, vol. 516, no. 20, pp. 6954–6958, Aug. 2008, doi: 10.1016/j.tsf.2007.12.026.

[39] B. Kaghouche, F. Mansour, C. Molliet, B. Rousset, and P. Temple-Boyer, ‘Investigation on optical and physico-chemical properties of LPCVD SiO $_x$ N $_y$ thin films’, *Eur. Phys. J. Appl. Phys.*, vol. 66, no. 2, p. 20301, May 2014, doi: 10.1051/epjap/2014130550.

[40] E. Camps, E. Campos-Gonzalez, J. Restrepo, A. Dutt, and G. Santana, ‘Structural and optical properties of nc-Si in SiOxNy matrix deposited by laser ablation for optoelectronic applications’, *Mater. Sci. Semicond. Process.*, vol. 91, pp. 377–382, Mar. 2019, doi: 10.1016/j.mssp.2018.11.020.

[41] V. G. Varanasi, A. Ilyas, M. F. Velten, A. Shah, W. A. Lanford, and P. B. Aswath, ‘Role of Hydrogen and Nitrogen on the Surface Chemical Structure of Bioactive Amorphous Silicon Oxynitride Films’, *J. Phys. Chem. B*, vol. 121, no. 38, pp. 8991–9005, Sep. 2017, doi: 10.1021/acs.jpcb.7b05885.

[42] S. Peter, S. Bernütz, S. Berg, and F. Richter, ‘FTIR analysis of a-SiCN:H films deposited by PECVD’, *Vacuum*, vol. 98, pp. 81–87, Dec. 2013, doi: 10.1016/j.vacuum.2013.04.014.

[43] S. K. Ray, C. K. Maiti, and N. B. Chakrabarti, ‘Low-Temperature deposition of dielectric films by microwave plasma enhanced decomposition of hexamethyldisilazane’, *J. Electron. Mater.*, vol. 20, no. 11, pp. 907–913, Nov. 1991, doi: 10.1007/BF02816031.

[44] J. Rissler *et al.*, ‘Effective Density Characterization of Soot Agglomerates from Various Sources and Comparison to Aggregation Theory’, *Aerosol Sci. Technol.*, vol. 47, no. 7, pp. 792–805, Jul. 2013, doi: 10.1080/02786826.2013.791381.

[45] R. Chow, W. A. Lanford, W. Ke-Ming, and R. S. Rosler, ‘Hydrogen content of a variety of plasma-deposited silicon nitrides’, p. 5.

[46] S. Bae, D. G. Farber, and S. J. Fonash, ‘Characteristics of low-temperature silicon nitride (SiNx:H) using electron cyclotron resonance plasma’, *Solid-State Electron.*, vol. 44, no. 8, pp. 1355–1360, Aug. 2000, doi: 10.1016/S0038-1101(00)00086-1.

[47] G. N. Parsons, J. H. Souk, and J. Batey, ‘Low hydrogen content stoichiometric silicon nitride films deposited by plasma-enhanced chemical vapor deposition’, *J. Appl. Phys.*, vol. 70, no. 3, pp. 1553–1560, Aug. 1991, doi: 10.1063/1.349544.

[48] A. El amrani, I. Menous, L. Mahiou, R. Tadjine, A. Touati, and A. Lefgoum, ‘Silicon nitride film for solar cells’, *Renew. Energy*, vol. 33, no. 10, pp. 2289–2293, Oct. 2008, doi: 10.1016/j.renene.2007.12.015.

[49] V. Sarou-Kanian, A. N. Gleizes, P. Florian, D. Samélor, D. Massiot, and C. Vahlas, ‘Temperature-Dependent 4-, 5- and 6-Fold Coordination of Aluminum in MOCVD-Grown Amorphous Alumina Films: A Very High Field ^{27}Al-NMR study’, *J. Phys. Chem. C*, vol. 117, no. 42, pp. 21965–21971, Oct. 2013, doi: 10.1021/jp4077504.